12-2011

Analysis of LEO Radiation Environment and its Effects on Spacecraft's Critical Electronic Devices

Luz Maria Martines S.
Embry-Riddle Aeronautical University - Daytona Beach

ANALYSIS OF LEO RADIATION ENVIRONMENT AND ITS EFFECTS ON SPACECRAFT'S CRITICAL ELECTRONIC DEVICES

BY
LUZ MARIA MARTINEZ S.

A THESIS
SUBMITTED TO THE DEPARTMENT OF PHYSICAL SCIENCES
AND THE COMMITTEE ON GRADUATE STUDIES
IN PARTIAL FULFILLMENT OF THE REQUIREMENTS
FOR THE DEGREE OF
MASTER OF SCIENCE IN ENGINEERING PHYSICS

12/2011
EMBRY-RIDDLE AERONAUTICAL UNIVERSITY
DAYTONA BEACH, FLORIDA

ANALYSIS OF LEO RADIATION ENVIRONMENT AND ITS EFFECTS ON SPACECRAFT'S CRITICAL ELECTRONIC DEVICES

by

Luz Maria Martinez S.

This thesis was prepared under the direction of the candidate's thesis committee chair, Dr. Bereket Berhane, Department of Physical Sciences, and has been approved by the members of the thesis committee. It was submitted to the Department of Physical Sciences and was accepted in partial fulfillment of the requirements of the Degree of
Master of Science in Engineering Physics

THESIS COMMITTEE:

Dr. Bereket Berhane, Chair

Dr. John Olivero, Member

Dr. Anthony Reynolds, Member

Dr. Peter Erdman
MSEP Graduate Program Coordinator

Dr. Michael Hickey
Department Chair, Physical Sciences

Dr. Robert Oxley
Associate Vice President for Academics

6/14/12
Date

Abstract

Spacecraft, space stations, satellites and astronauts are exposed to an increased level of radiation when in space, and it is important to evaluate the risks associated with extended radiation exposures in missions and space travel in general. The thesis focuses on the LEO radiation environment and how the particles in it interact with materials. Using existing empirical models, the exposed dosage due to the LEO space environment radiation sources, as a function of orbital altitude, orbital inclination and duration is studied. The physical processes that can result in failures and long term degradations of electronic devices due to solar radiation, high concentrations of electrons and protons trapped in the Van Allen radiation belts as well GCR and any secondary particles are examined. The impact on electronic components and systems onboard the spacecraft is evaluated.

Acknowledgments

I would like to thank the following individuals: Professors Dr. Bereket Berhane, Dr. Antony Reynolds, Dr John Olivero and Dr John French. I appreciated the help of Yishi Lee ,the staff in the Physical Science Department at Embry Riddle Aeronautical University and all of whom contributed greatly in this research. I want to dedicate this work to family and friends. Without them I would not be able to keep foward. And to Sebastian Guzman who has been always there for me.

This research has been supported by the LEO Radiation Impact on Humans and Safety Critical Components. The author is grateful to the FAA for personal funding.

Contents

List of Tables

List of Figures

Chapter 1

Introduction

For a long time space missions were launched and carried out by governmental agencies such as NASA. However, in the last decade there has been increasing interest in private (commercial) development of reusable launch vehicles. Recently, NASA has asked private contractors to build feasible suborbital spaceships to transport crew and cargo to the International Space Station (ISS). A number of groups in the commercial space industry are already planning to deliver payloads for scientific missions. Further, most of them have a long-term interest in new 'space tourism' industry [Reifert, 2009]. The success of these early efforts by the private sector will be crucial in developing future infrastructure for safe, reliable and affordable commercial space transportation. Most of the initial space missions by the private sector are expected to be suborbital or in low earth orbit (LEO).

In LEO spacecraft, space stations, satellites and astronauts are subject to an increased level of radiation due to energetic particles trapped by the earth's magnetic field, solar flares and galactic cosmic rays. Therefore, it is important to evaluate the risks associated with extended radiation exposures in LEO missions in particular and space travel in general and devise mitigation plans [Pisacane, 2008].

Mitigating the effect of radiation depends on accurately evaluating the radiation exposure, the radiation susceptibility of the material, and the level of acceptable risk. If the launch date, the mission duration, the trajectory, and mission scenario are known, there are some models that simulate the radiation environment; material

properties of shielding and the potential damage mechanisms can be used to estimate exposure dose rate in both humans and devices. In turn, knowing the dose rate permit to quantify the risk levels.

The vehicles used for space mission purpose are designed under the most strict requirements and standards to make certain that the crew is safe and the systems onboard the vehicle not fail at any point. In order to guarantee proper integration and functionality of the man-system interface the design requirements must apply to launch, entry and on-orbit, and environments. It is, therefore, important to understand the basic components of mission critical devices and systems that are on the space craft.

All space craft have a power supply and an electrical distribution system that supplies all systems and instruments of the spacecraft. The details of the power system used on a spacecraft depend on many factors such as flight duration and location of the mission. Chemical cell batteries are used on most space-vehicles and satellites to generate direct current power. However, they are not ideal for long term use due to their relatively short life time. They are often used in conjunction with solar panels to store power for use during times when the panels are shaded from sunlight. Solar power is very practical for spacecraft operating near the sun. The main short coming of solar cells is the need for additional structural support which adds more weight to the satellite or vehicle. Radioisotope thermoelectric generator are ideal source of power but they have to be housed in a crash resistant structures to avoid any nuclear contamination in case of failures [Braeunig, 1999].

Another important system consists of communication devices which are chosen based on the requirements of the mission such as anticipated distances, planned frequency bands, data rates and available on-board transmitter power. Dish-shaped antennas are principally used for high rate communication with Earth because of their highly directionality. In addition to the antennas, communication systems include transceivers which code data on to the carrier and decode data from it. Most of the electronic and optoelectronic devises involved in communication systems are Si or GaAs based.

Onboard computers are responsible for overall management of a spacecraft's activity like timing, command interpretation as well as to collect and process telemetry data. Telemetry transmissions are typically a mixture of science data from the experiments and spacecraft engineering or health data. This information may be transmitted in real time, or it may be written to a data storage device until transmission is feasible.

A spacecraft's attitude, its orientation in space, must be stabilized and controlled so that its high-gain antenna may be accurately pointed to Earth, so that onboard experiments may accomplish precise positioning for accurate data collection and subsequent interpretation. In order to maintain or restore three-axis stability, to control spin, to execute maneuvers and make minor adjustments in trajectory, spacecraft are provided with sets of control elements such as chemical trusters, momentum wheels and magnetic torquers. These devices are typically of either the hypergolic bi-propellant type or the mono-propellant type.

A spacecraft must operate and survive in the hostile environment. Sensitive components must be protected from the harsh extreme thermal variations, micrometeoroid bombardment, and other space hazards. Reflectors and other techniques are used to cool the spacecraft components as needed. Internal components are typically painted black to radiate heat more efficiently. Critical components are generally shaded using gold or optical solar reflectors. The use of resistive electric heaters or radioisotope heaters helps to keep spacecraft components above their minimum allowable temperatures The life support subsystems onboard a manned spacecraft or space station is responsible for maintaining a livable environment within a pressurized crew compartment. Included are subsystems for providing oxygen, drinking water, waste processing, temperature control, ventilation and CO_2 removal.

To ensure survival of the crew most basic physiologic parameters must be met. The crew must also be protected from long term health hazards as well. Survival is not the only alone in the consideration; the environmental conditions must also be of sufficient quality to permit the occupants to perform their required tasks. Other critical systems are summarized in tha Appendix B.

Some types of spcecrafts and their manufacturers are presented in Apendix A .

A biref description is given for the most remarkable aspects of each of them. It is clear from the previuos discussion that space vehicles rely highly on electronics and optoelectronic systems to function properly and ensure the safety of the crew.

More importantly, as the industry moves toward more commercialized space missions, reliance on commercial off the shelf (COTS) could be more prevalent. In general, COTS are not designed on purpose for space use and can suffer failures due to radiation events and the LEO radiation environment poses a great risk to mission with such electronic and optoelectronic devices and systems. Therefore, it is important to evaluate the risks associated with extended radiation exposures to critical components and systems in space missions and space travel in general.

Although great care has been taken to ensure radiation hardening in past space missions, especially after the Telstar satellite failure due to radiation effects in 1962, failure due to radiation effects on system critical components are still a big issue. The loss of some commercial satellites such as ETS-6, HST (STS-31) has been linked to failure due radiation [Bedingfield et al., 1996]. Pritchard et al. [2002] present radiation effects observed in several spacecraft such as Galileo and Mars Pathfinder at the system and subsystem level Thus, to ensure mission success the effects of space radiation must be taken into account.

The first step to mitigating system failures due to radiation in LEO is to understand the mechanisms that lead to them. Understanding long term degradations and accurate prediction of Single Event Effects (SEE) rates for spacecraft computers in orbital environments is needed for safe and cost-effective system designs. There have been a significant number of experimental and theoretical studies to address this issue. Using data from CRRES (Combined Release and Radiation Effects Satellite), effects on microelectronics Gussenhoven et al. [1995] and on single event upsets (SEU) Buchner et al. [2000] have been addressed. SEU rate calculations for effects due to cosmic rays is presented by Tang [1996]. An overview of radiation effects in semiconductor devices is due to various environments, including space, with extensive bibliography can be found in the book by Claeys and Simoen [2002]. A collection of papers on the effects of radiation, with emphasis on space application to space, that address modeling, testing and mitigation are given in the book by Velazco et al.

[2007].

Spacecraft interact with the space environment in ways that may affect the operation of the spacecraft as well any scientific experiments that are carried onboard. Understanding and modeling the LEO environment in which the spacecraft will travel is the first step towards safe and space travel and mission. Many models that are based on NASA's AP and AE models exist [Jordan, 1989]. The models are generally empirical. Gussenhoven et al. [1995] used data from APEX satellite to monitored single event effects on SRAMs and power MOSFETs.

Current trends in the design of electronic devices are toward a higher density and smaller components. Once the radiation spectrum in LEO environment is obtained, to analyze the failure mechanism, it is necessary to investigate the microscopic interactions between the radiation and the semiconductor and shielding materials. A broad description of the interaction of ionizing radiation and matter is given by Prussin [2007].

As one of the type of interactions for electromagnetic radiation with matter, Bethe and Maximon [1954] and Davies et al. [1954] disscused pair production differential cross section for all elements. Bethe-Heitler formula is derive and multiplied by a relatively simple factor that made the corrections. Small Z elements used the Born correction, proportional to Z^2 . For heavier elements the correction is somewhat less than the Z^2 [Bethe and Maximon, 1954],[Davies et al., 1954]. Detailed descriptions of the various electromagnetic phenomena can be found in textbooks such as the one by Jackson.

Thus, although there has been significant progress in understanding the effects of radiation on electronic devices that operate in space environment, deeper understanding of the mechanisms that cause failures and more systematic classification the effects on the devices, especially on the new commercial off the shelf devices, is needed to implement radiation hardness assurance programs and guarantee success of the many proposed commercial missions to LEO.

Therefore, in this thesis a detailed study of the physical processes that result in device failure is carried out. The results are applied to obtain Numerical approximation of single event failures in various devices. Comparisons with more rigorous packaged,

Monte Carlo simulations show that the simpler semi analytical tools can be used to reasonably predict failure modes and failure rates. Further, comparison of the results is made using data from experimental results. Finally data from tests conducted by NASA's Radiation Effects and Analysis Group (REAG) is used to create a table of many existing electronic devices and their failure rates.

Calculation of failure rates requires accurate knowledge of radiation flux received by the device material under consideration. Hence, after comparing several well established models such as CRÈME, SPENVIS was chosen to perform simulations of the LEO radiation environment and get estimates for the radiation flux that would impinge on the mission critical devices, with and without shielding.

The thesis is organized as follows. In Chapter 2, using existing empirical models, the exposed dosage due to the LEO space environment radiation sources, as a function of orbital altitude, orbital inclination and duration is studied. Numerical result using SPENVIS and CREME-96 are obtained. The physical processes that can result in failures and long term degradations of electronic devices due to solar radiation, high concentrations of electrons and protons trapped in the Van Allen radiation belts as well GCR and any Secondary particles are examined in Chapter 3. The stopping power and reaction cross sections are investigated for photons, charged particles and neutrons. The impact of these processes on electronic components and systems onboard the spacecraft are studied in Chapter 4. Shield materials and methods are compared in chapter 4.4. A specific example that brings all of these issues together is presented in Chapter 4.2.2. Concluding remarks and recommendations for future work are presented in Chapter 7.

Chapter 2

Modeling of Radiation Environment in LEO

The interplanetary space is not an absolute vacuum. In addition to galactic and solar particles, there are about 10 energetic particles per cubic centimeter. Most of these particles come from the sun; the solar wind flows radially out from the sun with a speed that varies from about 300 to 1000 kilometers per second near the earth's atmosphere. Others are due to the galactic cosmic rays. In this chapter, the various sources for radiation in LEO are reviewed. Further, using existing models the spectrum of the fluxes of protons and electrons in LEO are obtained [Davis et al., 2008].

2.1 Radiation Sources

2.1.1 Trappaed radiation

The interplanetary space is not absolute vacuum. In addition to galactic and solar photons, there are about 10 energetic particles per cubic centimeter. Most of these particles come from the sun; the solar wind flows radially out from the sun with a speed that varies from about 300 to 1000 kilometers per second near the earth's atmosphere. Like most planets and the sun the earth has a magnetic field which

deflects and traps the charged solar wind particles thereby creating a cavity known as the magnetosphere. In the magnetosphere the motion of energetic protons and electrons is confined by the earth's magnetic field in a region called the Van Allen Radiation Belts and were discovered at the beginning of the space age. The detailed mechanism by which the particles are trapped in the Van Allen belts is not completely understood; however, since their hazard to space travel was recognized promptly, there has been considerable amount of effort to model the trapped proton and electron populations. Although there continues a significant amount of research in the space physics community to understand and model the Van Allen belts better, NASA's AP-8 and AE-8 models, which were developed in the 1970s are have become the standard. In this section, these models and models based on them are discussed in more details.

The motion of charged particles in the Earth's magnetic field is governed by the Lorentz force

$$\vec{F} = q\left[\vec{E} + \left(\vec{v} \times \vec{B}\right)\right] \tag{2.1}$$

where q is the particle charge (including sign), $\vec{v}$ is the velocity vector of the particle, $\vec{B}$ is the magnetic field vector in space with magnitude B, and $\vec{E}$ is the electric field vector in space with magnitude E.

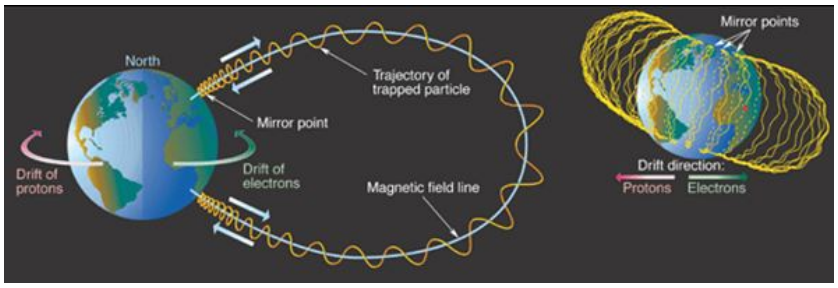

Figure 2.1: Motion of charged particles trapped in the Earth's magnetic field

The motion of these energetic charged particles can be determined using the Lorentz force and the analysis can be summarized as follows:

1. *Gyration* about geomagnetic field line for which the radius of circular motion is known as the *radius of gyration* or *Lamor radius*.

2. *Drift* in a direction perpendicular to both the geomagnetic field and the component of the applied force field perpendicular to the magnetic field.

3. *Mirroring* along the field lines bouncing back and forth between the northern and southern geomagnetic hemispheres. The *mirror point* is the point along the field line where the particle reverses direction.

4. *Longitudinal drift* around the geomagnetic axis forming a shell around the Earth. Positively charged particles drift westward and negatively charged particles drifts eastward.

A typical motion of a charged particle in the Van Allen belts is depicted by 2.1. The mirror points, the trajectories and the drift motion combined create the peculiar shape of the Van Allent belts.

The result is a toroidal surface aligned with the Earth's magnetic dipole axis, called drift shells. Trapped Particles remain there for long periods of time. These particles consist mainly of protons (energy 100 keV - 100 MeV) and electrons (energy 10 keV-10 MeV); there is also evidence that indicates the presence of heavy ions.

Of particular concern, for the LEO enviroment, is the extension of the inner radiation belt to low altitudes in the region where the Earth's magnetic field is particularly weak. This can be seen clearly in Figure 2.2 where the distribution of the belts and the orbit are presented [Heynderickx, 2002].

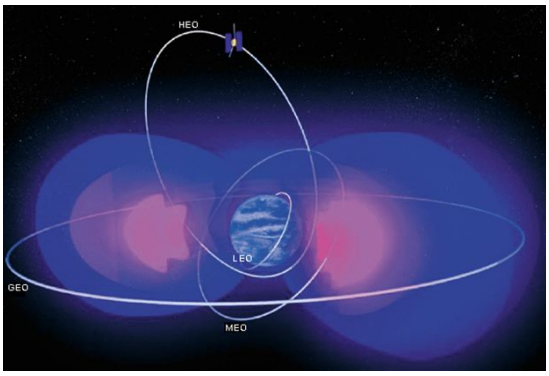

Figure 2.2: The Van Allen radiation belts and typical satellite orbits. GEO, HEO, MEO, LEO. Credit NASA

The inner belt extends for approximately hundreds of kilometers to $\approx 6,000$ km in altitude, and its populated by high energy protons and electrons $(1-10\text{MeV})$. The outer belt spanning up to $60,000$ km in altitude, is predominately made up of high-energy electrons. Due to the deviation of the geomagnetic poles from the geographic poles, the inner belt is closer to the Earth's surface near the south Atlantic reagion, this is call the South Atlantic Anomaly. In this region the particles penetrate more into the atmosphere because of the weak magnetic field at this particular point; that is why the fluxes of particles concentrated near the South Atlantic region. A schematic of the radiation flux contours for the Van Allen belts is presented in the Figure 2.3.

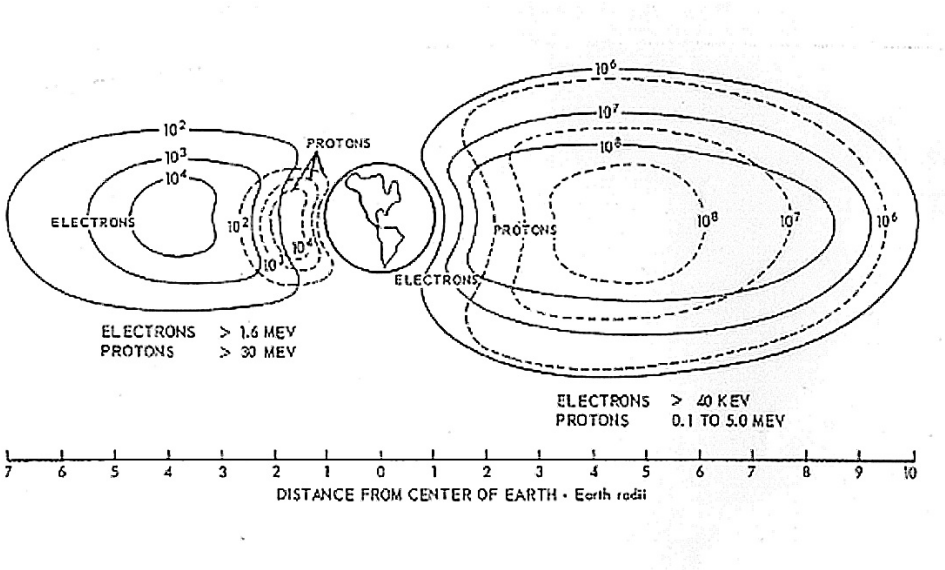

Figure 2.3: Trapped Radiation Belts as function of energy and distance from Earth

The environment encountered by satellites in LEO is mainly the proton and electron particles trapped in the Van Allen belts, and satellites pass through this region several times each day. The fluxes observed in these passes depend on the orbital inclination and altitude. The greatest inclination dependencies occur in the range of $0° < \theta < 30°$. For inclinations over 30°, the fluxes rise more gradually until about 60°. Over 60° the inclination has little effect on the flux levels.

In Figures 2.4 and 2.5, it could be observed how the proton and electron distribution depends on the solar cycle as well. The largest altitude variations occur between

200 to 500 km where large increases in flux levels are seen as the altitude increases [Hastings and Garrett, 2004].

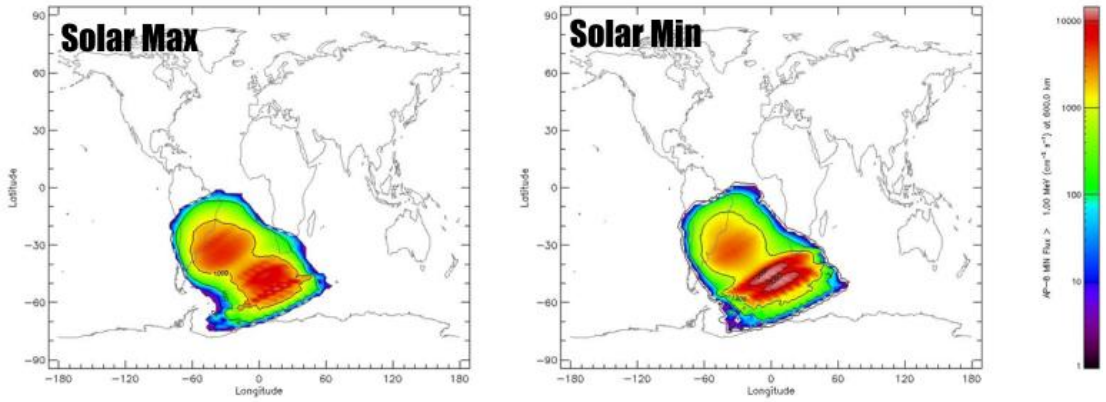

Figure 2.4: Proton distribution at solar maximun and solar minimum, for an orbit at 600Km

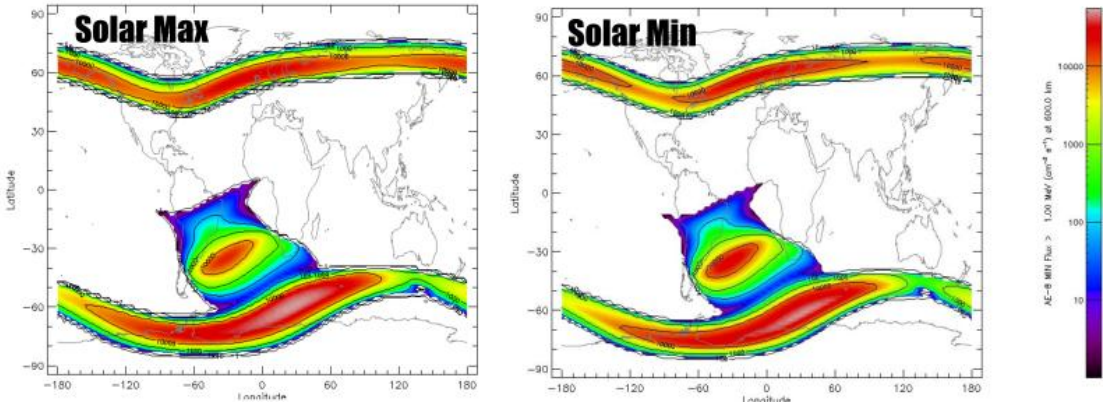

Figure 2.5: Electron distribution at solar maximun and solar minimum, for an orbit at 600Km

The change in the distribution of the trapped protons with respect to the altitude can be observed in Figure 2.6, similarly for electron distribution is presented in Figure 2.7. The figures were made for solar maximun at different altitudesfor protons and electrons with a energy greater than 1MeV. The projection of the proton distribution on the world map is shown at values of 200, 300, 400 and 500km.

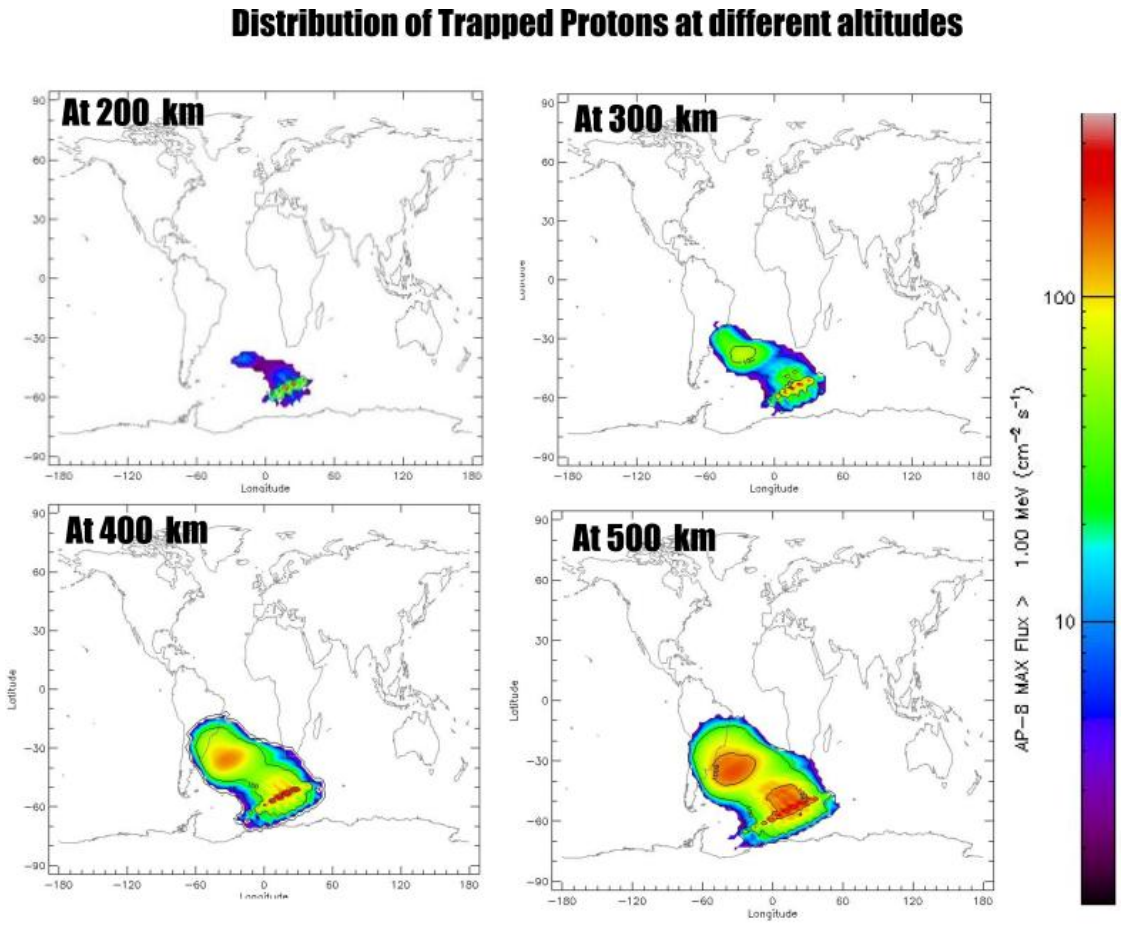

Figure 2.6: Proton distribution at different altitudes during Solar Maximum (world map projection). SPENVIS

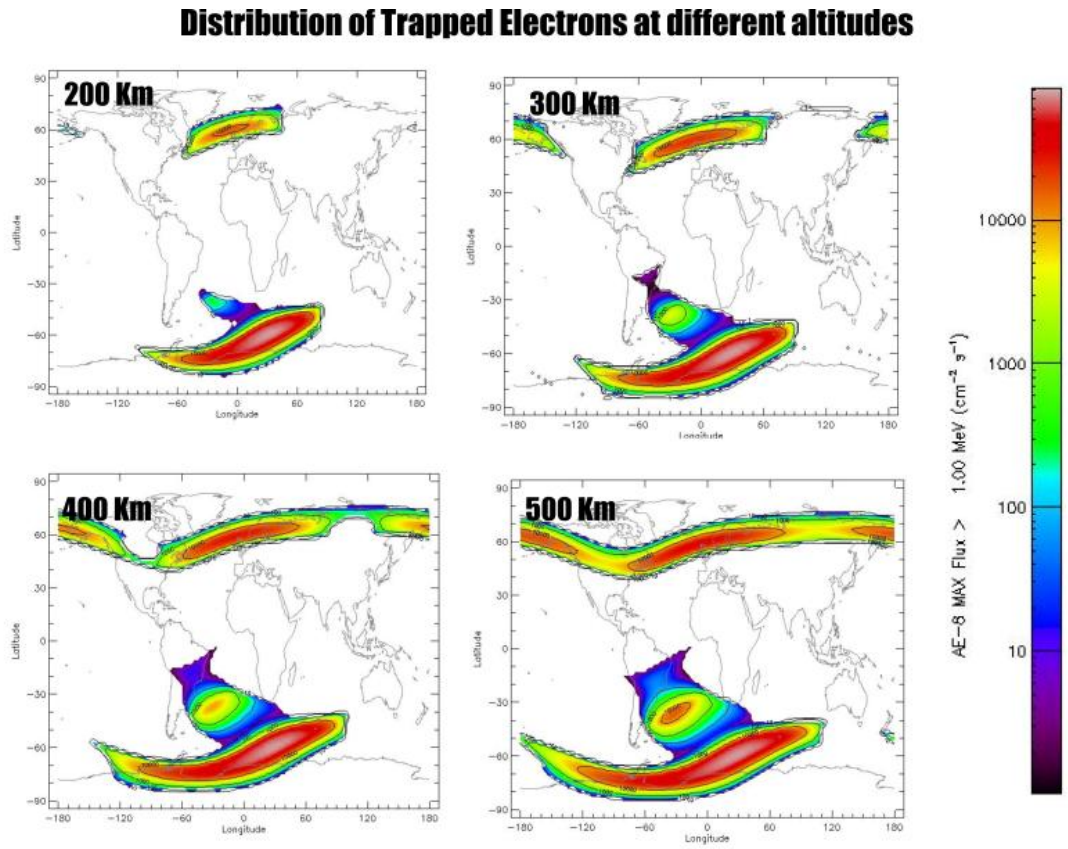

Figure 2.7: Electrons distribution at different altitudes during Solar Maximum (wordl map projection). SPENVIS

The increase of the flux is more considerable over 600 km altitudes. The location of the peak fluxes depends on the energy of the particle. For trapped protons with $E > 10$ MeV, the peak is at about 4000 km. In Figure 2.8 the proton spectra is plotted using SPENVIS at a latitud of 0^O and longitude of 0^O. The peak is approximately at 4000 km, either for solar maximun or solar minimum; then the flux drops gradually at altitudes above 4000km.

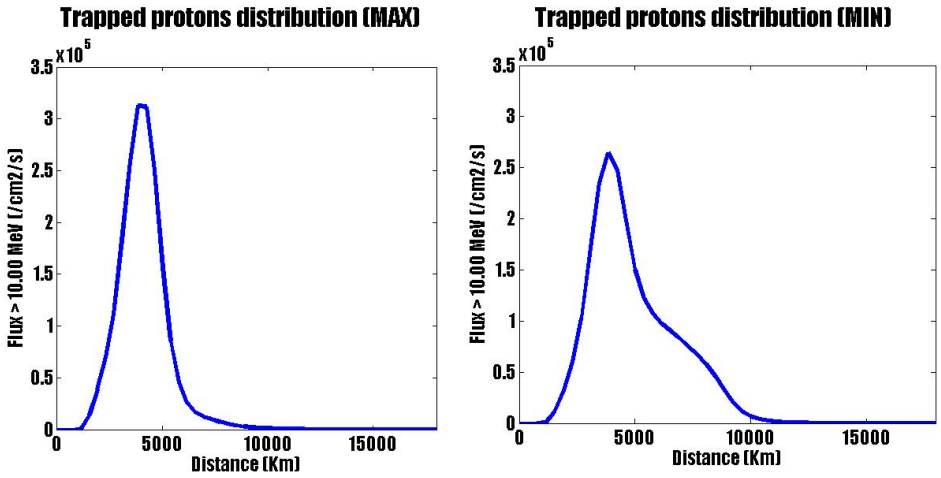

Figure 2.8: Graphics of Trapped Proton distribution at Solar Maximum and Solar Minimum

2.1.2 Galactcic Cosmic Rays

Galactic cosmic rays originate outside the solar system and provide a continuous flux of particles with number density on the order of a few particles per square centimeter per second. They are composed of approximately 85% protons, 14% alpha particles (helium nuclei), and 1% electrons and heavy ions. Some of the heavy ion spectrums outside the Earth's magnetosphere are shown in Figure 2.9. They include the highest energy particle radiation in the solar system, up to 10^{20}eV, and so the geomagnetic field is generally not sufficient to deflect the higher energy particles

For LEO spacecraft, the Earth's magnetic field deflects many of the lower-energy particles. At this low inclination, only particles with sufficiently high energy can

penetrate through the magnetic shielding. In the polar regions, particles can enter almost parallel to the magnetic field resulting in a higher and more directional flux.

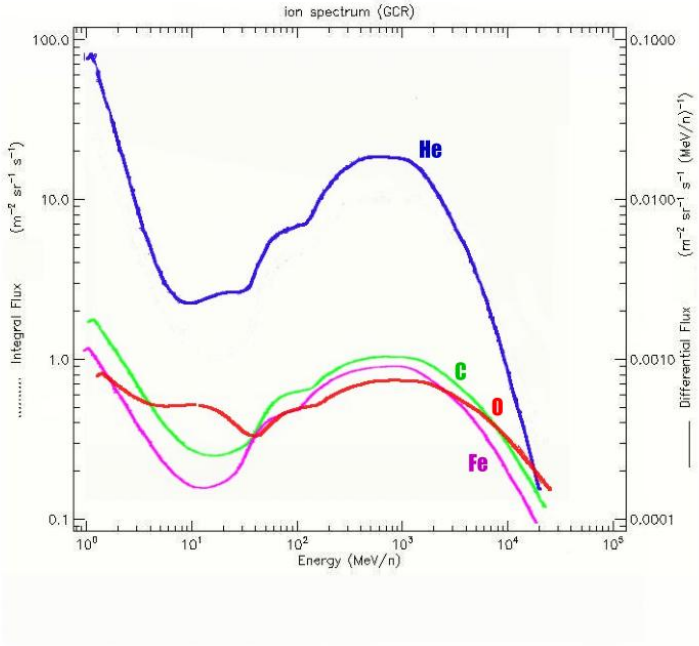

Figure 2.9: Galactic Cosmic Rays Sprectrum for some heavy ions

The magnitude of the flux correlates negatively with solar activity, with the minimum at solar maximum and maximum at solar minimum. During maximum solar activity, the sun is more likely to eject plasma with embedded magnetic fields to deflect some of the lower energy galactic cosmic rays.

2.1.3 Solar energetic particles

Solar particle events (SPE) are streams of particles that emanate from the sun during a coronal mass ejection, see Figure 2.10. Particle acceleration occurs from the release of energy during these events that causes a magnetohydrodynamic shock wave to develop and propagate from the sun throughout the interplanetary medium. The flow density of the radiation emitted is positively correlated with solar activity with lower fluxes during periods of low solar activity and higher fluxes and more frequent

occurrences during periods of higher solar activity.

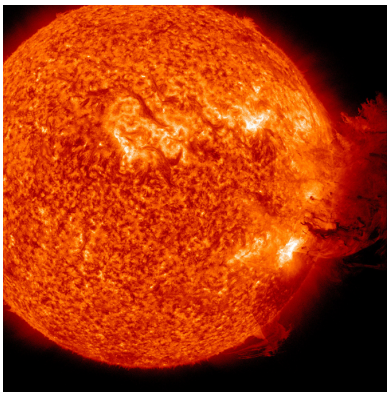

Figure 2.10: Coronal mass ejection from the sun, Credit: NASA/SDO

Solar particle events are unpredictable for time of occurrence, magnitude, duration, and composition. They can last from a few days to a week, with peak radiation persisting for hours. Solar flares and coronal mass ejections are emitted directionally and only a small fraction encounters the Earth. A number of significant events associated with past solar cycles may have been responsible for several spacecraft operational anomalies. Furthermore, radiation protection is a prime issue for space station operations, especially for extended missions [Pisacane, 2008].

The eleven year solar cycle can be divided into four stationary years with a small number of flare events (solar minimum) and seven active years with a large number of events (solar maximum). During the solar minimum phase, few significant solar flare events occur; therefore, only the seven active years of the solar cycle are usually considered for spacecraft mission evaluations. Large solar flare events may occur several times during each solar maximum phase. The proton energies may reach a few hundred MeV and the heavy ion component ranges in energy from 10s of MeV/n to 100s of GeV/n. As with the galactic cosmic ray particles, the solar flare low energy particles are attenuated by the Earth's magnetosphere [LaBel, 1996].

An empirical model of the solar flare proton environment based on solar cycle 20 has existed since 1973. This model divides events into 'ordinary' and 'anomalously large' (AL) and predicts the number of AL events for a given confidence level and

mission duration. Particles accelerated in flares include electrons, protons, alpha particles, and heavier nuclei. Fluxes of heavier nuclei are very small relative to proton fluxes and cause less damage to space systems. Electrons, due to their very small masses, likewise cause little damage. Alpha particle fluxes typically amount to 2 to 10 percent of the proton fluxes for similar energies and could, on occasion, be troublesome. Because the propagation of solar protons is controlled by the plasma and the magnetic fields in the lower corona and in interplanetary space, particle flux profiles observed by interplanetary spacecraft are often very complex, indicating that the nature of the solar events is barely understood and hard to simulate. [Stassinopoulos and King, 1974].

2.2 Radiation Models

Early models of the space environment relied on a static description of the particles in Van Allen belt; however, data obtained from some space missions such as Relay, Telestar, ERS13, Explorer, Gemini 4, Azur among others presented by Sawyer and Vette [1976], they showed that the static models are insufficient. The data showed spatial and temporal variations must be included for a more accurate description of the dynamics of the trapped particles in the Van Allen belts. Although, at present, no fully dynamic and global models exist, considerable progress has been made in the modeling of the space radiation environment including temporal and spatial variations [Sawyer and Vette, 1976]

The standard models of the trapped radiation in the Van Allen belts are the AP8 model for protons and the AE8 model for electrons developed by NASA [Jordan, 1989].

2.2.1 AP8 and AE8 Trapped Particles Models

AP-8 model gives trapped proton fluxes (particles per unit area per unit time) at a given location in geomagnetic coordinates. The McIlwain L parameter is introduced

in the description of the geomagnetic coordinates, and is defined by

$$L = r_0/R_E \tag{2.2}$$

where the distance r_0 is the radial distance at which a field line crosses the magnetic equator and $R_E$is the radius of the Earth ($\approx$ 6400Km) [Pisacane, 2008].

The proton energy range is from 0.1 - 400MeV. The AP-8 model is restricted to L shell values between 1.15 and 6.5. The model uses solar maximum conditions (AP-8 MAX) and solar minimum conditions (AP-8 MIN). Similarly the AE-8 model gives trapped electron fluxes of energies between 0.4 -7MeV within the L shell values of 1.14 and 12. Also, the AE-8 MAX and AE-8 MIN models are for solar maximum and solar minimum respectively.

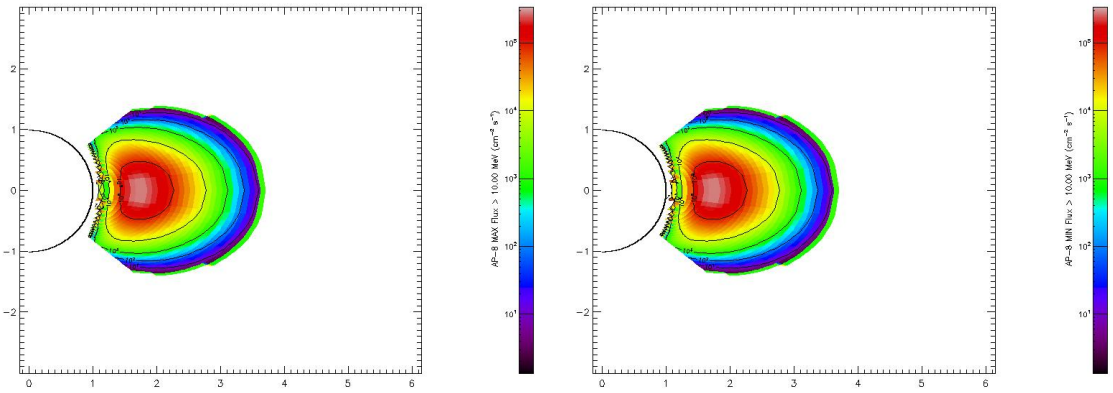

(a) AP-8 Proton Flux during Solar Max (b) AP-8 Proton Flux during Solar Min

Figure 2.11: Trapped Proton Fluxes intensities, distances in Earth radii; SPENVIS

Figure 2.11 illustrates the proton fluxes during solar maximum and solar minimum in false colors. Below, in Figure 2.12, the electron fluxes are also represented in false colors [Pisacane, 2008].

The dipole magnetic field model fit to describe the Earth's magnetic field is tilted (incline to the geographical poles) and offset (from the geometric center of the earth). This offset of about 550 km is antipodal to the direction just south of Brazil, so the a higher value of L shell approaches the surface of the Earth in that region. This

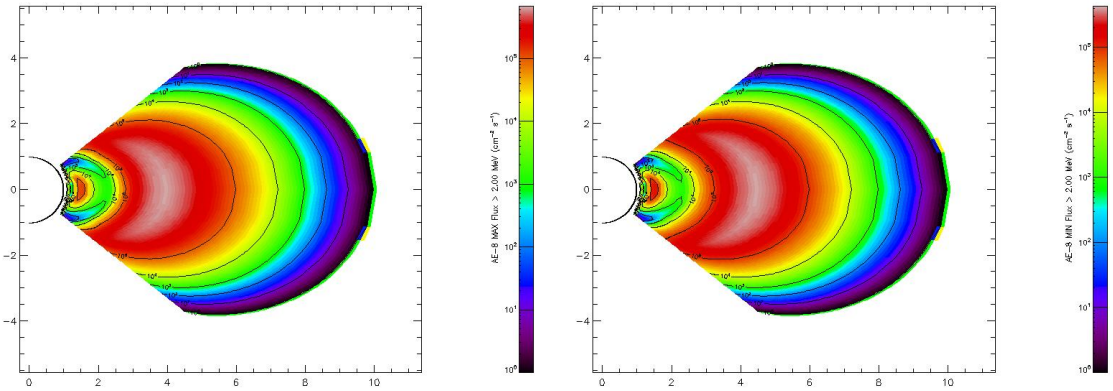

(a) AE-8 Proton Flux during Solar Max (b) AE-8 Proton Flux during Solar Min

Figure 2.12: Trapped Electron Fluxes intensities, distances in Earth radii; SPENVIS

region is called South Atlantic Anomaly. The L shells in the South Atlantic Anomaly contain significantly higher concentration of protons and electrons, as illustrated in Figure 2.13.

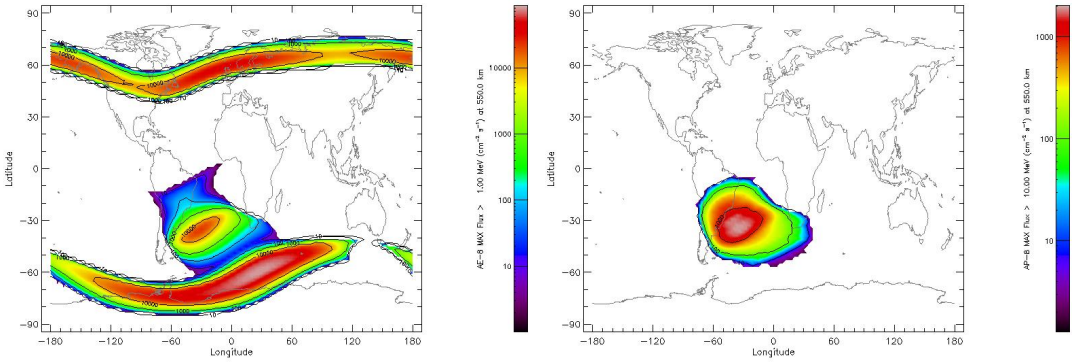

(a) AE-8 Integral elctron Flux >1MeV (b) AP-8 Integral proton Flux >10MeV

Figure 2.13: Proton and Electron distribution at 550km altitude in Solar Max; SPENVIS

2.2.2 CREME96

The Cosmic Ray Effects on Micro-Electronics (1996 Revision) is a suite of programs for creating numerical models of the ionizing radiation environment in near-Earth orbits, evaluating the resulting radiation effects on electronic systems in spacecraft and in high-altitude aircraft, estimating the high LET radiation environment within manned spacecraft.

2.2.3 The Space Environment Information System SPENVIS

ESA's Space Environment Information System, a WWW interface to models of the space environment and its effects, including the cosmic rays, natural radiation belts, solar energetic particles, plasmas, gases, and 'micro-particles'. The models implemented in SPENVIS require as input a set of points on a spacecraft trajectory or a user-defined set of geographic points. These sets of points are produced by two tools: the orbit generator and the coordinate grid generator. In general, one of these tools has to be used before the models themselves can be accessed. SPENVIS is able to detect whether a spacecraft trajectory or a coordinate grid has been generated. Once a trajectory or a coordinate grid has been generated, it can be used by different models. This means that, in the context of a given project, it is not necessary to generate coordinates for each model separately. The models implemented in SPENVIS have been organized in the following packages:

- radiation sources and effects
- spacecraft charging
- atmosphere and ionosphere
- magnetic field
- meteoroids and debris
- data base queries
- miscellaneous

- ECSS space environment standard

The radiation environment model used for the trapped particles is the AP8 - AE8, the fluxes of trapped protons and electrons, is determined as an integral or differential flux according to the output required. The distribution of these particles can be plotted in different perspectives for it easy visualization, a 3D projection, a world map distribution, or the projection of the radiation belts on space.

Chapter 3

Radiation Interactions with matter

The radiation types of concern here include charged particles such as electrons (beta particles), protons, alpha and fission fragment ions, and the neutral particles such as photons (gamma and X rays) and neutrons. Table 3.1 compares some key characteristics of the types of radiation of interest here, including charge, mass, and range in air.

Characteristic	Alpha(α)	Proton (p)	Beta (β)	Neutron (n)	Photon (γ)
Symbol	${}^{4}_{2}He^{2+}$	${}^{1}_{1}p$ or H^{1+}	${}^{0}_{-1}e$ or β	${}^{1}_{0}n$	${}^{1}_{0}\gamma$
Charge	+2	+1	−1	neutral	neutral
Ionization	Direct	Direct	Direct	Indirect	Indirect
Mass (amu)	4.001506	1.00727	0.0005485	1.008665	-
≈ Velocity (cm/s)	6.944×10^{8}	1.38×10^{9}	2.82×10^{10}	1.38×10^{9}	$c = 2.998 \times 10^{10}$
Speed of light	2.3%5	4.6%	94.1%	4.6%	100%
Range in Air	0.56cm	1.81cm	319cm	39250cm	82000cm

Table 3.1: Raidiation Type description

For a kinetic energy of 1 MeV, the electron is relativistic. For the same energy, the heavier particles are slower, stopped easier and deposit their entire energy over a shorter distance. For example, the passage of various radiation typewith the same energy through a material is depicted in Figure 3.1.

The interaction of the charged particles passing through matter is essentially different from that of the neutral radiation. In particular, the charged particles strongly interact with the orbital electrons of the mater.

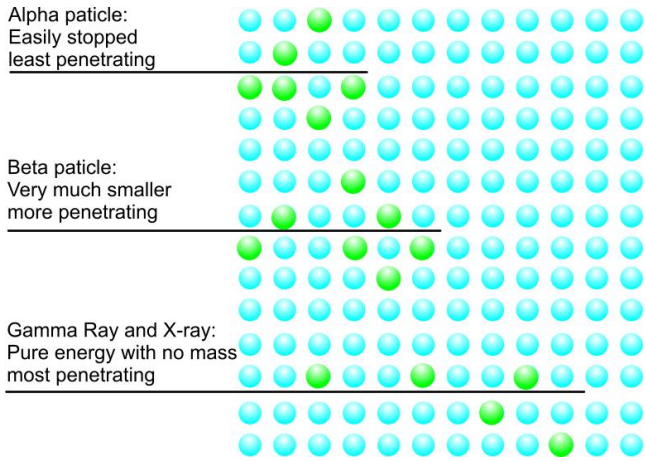

Figure 3.1: Radiation path through a material atom lattice(blue), the green atoms are ionized

3.1 Interaction Cross Sections

The interaction of energetic particles and photons with atoms is essentially a scattering processe. For a given type of radiation there are various process that can occur. The end results are in general dependent on the radiation type, energy and the target atom. For a given process it is particularly important to find the probability of its occurrence. Instead of treating the process as dynamic (time dependent), it is more convenient to consider an equivalent stationary process. Therefore, we consider a continuous current of particles incident on the target atom that scatter (possibly creating new particles) from the target.

A useful parameter that characterizes the scattering processes is the *scattering cross section*. The total scattering cross section is a measure of the rate of reactions (scattering processes) that occur per target atom for a given flux of the incident radiation. Commonly, it is measured in *barns* $\equiv 10^{-28}\mathrm{m}^2$. It is defined as

$$\sigma \equiv \frac{\text{number of reactions per second per nucleus}}{\text{number of projectiles incident per second per area}} \tag{3.1}$$

The cross section can be calculated using quantum mechanics by relating the transition probability. In the first order perturbation, the transition probability from a specific intial state to a specific final state is giving by *Fermi's Golden Rule* [Bernstein

et al., 2000]:

$$w = \frac{2\pi}{\hbar} |H'|^2 \rho(E_f) \tag{3.2}$$

where H' is the matrix element beween the initial and final states for the perturbation potential responsible for the transition and $\rho(E_f)$ is the density of possible final states of a reaction of the form

$$a + A \rightarrow b + B$$

In general, when a projectile a scatters from a target A resulting in a light and heavy products, b and B respectively. Using the Equation (3.2) the probability (cross section) of this interaction can be calculated as

$$\sigma_{a,b} = \frac{w}{\phi_a} \tag{3.3}$$

where ϕ_a represents incident monoenergetic projectile flux. The flux can be written as the product of the projectile density, n_a, and the projectile velocity, v_a, ie,

$$\phi_a = n_a v_a \tag{3.4}$$

The density of the final states represents the density of continuum states available to b and is:

$$d\rho_b = \frac{4\pi V}{h^3} p_b^2 dp_b \tag{3.5}$$

where p_b is the momentum of the paarticle b.

The density of final states in Equation (3.5) assumes only one combination of the orientations of the angular momentum vector of the reaction products. The angular momentum and quantum number j_B and J_B have a total number degeneracy that is determined by the product $(2J_B + 1)(2j_b + 1)$. Including this degeneracy the density of final states can be written

$$\rho(E_f) = \frac{dn}{dE_F} = \frac{4\pi}{h^3}(2J_B + 1)(2j_b + 1)\frac{p_b^2}{v_b} V \tag{3.6}$$

Direct substitution of equations (3.3)and using the Fermi's Golden rule equation (3.2), the reaction cross section is given by

$$\sigma_{a,b} = \frac{V^2}{\pi\hbar^4} |H_{a,b}|^2 (2J_B + 1)(2j_b + 1)\frac{p_b^2}{v_a v_b} \tag{3.7}$$

The general expression presented for cross section need some corrections accordingly to the type of interaction. If applied to charge particles must contain the coefficients responsible for the coulomb interactions.

It is also convinient to determine the differential cross section by definition as $\frac{d\sigma}{d\Omega_\theta}$. Then, the scattering of the incident radiation into a solid angle is given by $\sigma(\theta)d\Omega_\theta$.

3.2 The interaction of photons with matter

Photons are the fundamental constituent of electromagnetic radiation, have zero mass and no charge. Forms of electromagnetic radiation include radiowaves, microwaves, light, ultraviolet, x-rays and γ rays [Jackson, 1999].

There are three essential photon-matter interaction processes relevant to the scope of this work. These are Compton scattering, photoelectric effect and pair production. For comparison, the simple scattering of low eneregy electromagnetic radiation by an elecron is disscussed, known as Thompson scattering.

Consider an electromagnetic wave incident on an electron as depicted in Figure 3.2. The direction of the propagation of the incident radiation is taken to be along the positive $y - axis$.

The electric field vector at the location of the elctron is given by

$$\vec{E} = E_0 \sin \omega t \tag{3.8}$$

The Poyntingvector, i.e., the energy of the electromagnetic radiation per unit area normal to the direction of its propagation is given:

$$\vec{S}_{in} = \epsilon_0 c^2 (\vec{E} \times \vec{B}) \tag{3.9}$$

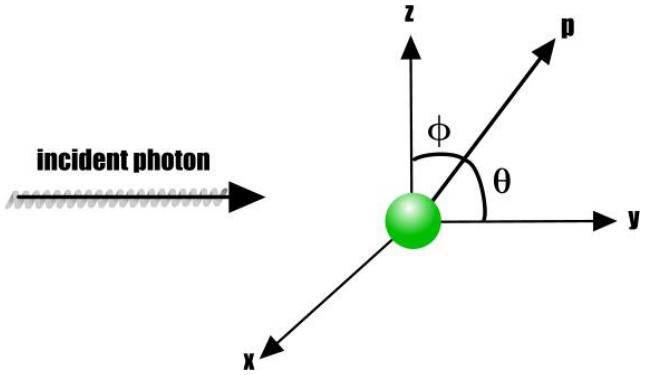

Figure 3.2: Schematic diagram Elastic Scattering

where $\vec{B}$ is normal to E and the direction of propagation. The time averaged power per unit area is given by

$$|S_{in}| = \epsilon c \left|E\right|^2 \tag{3.10}$$

To understand the resulting motion of the electron we note that the force experienced by the electron is $\vec{F} = -e\vec{E}$. The equation of motion of the electron is given by

$$m_e \frac{d^2 z}{dt^2} = eE \sin \omega t \tag{3.11}$$

The oscillating electron, consequently, produces an electric dipole moment in the z direction of the magnitude $M = ez$ re-emits the absorbed energy and this results in an electric field E' and Poynting vector S_{out} at the point P, at an angle of θ with the $y - axis$ and ϕ the azimuthal angle with the $z - axis$.

At the point P the electric field of an oscillating electric dipole can be written using the definition for the electron dipole momentum as $M = ez$

$$E' = \frac{1}{c^2} \frac{d^2 M}{r dt^2} \sin \theta \tag{3.12}$$

where r is the distance between the dipole and the point P. Now, using (3.12), (3.11) the resulting time averaged power per unit area along the propagation direction can be given by

$$\langle |S_{out}| \rangle = \frac{e^4 \left|E_0\right|^2}{64\pi^2 \epsilon_0 m_e^2 c^3 r^2}(1+\cos^2\theta) \tag{3.13}$$

The equations (3.13) and (3.15) permit the determination of the differential Thompson scattering cross section and is given by

$$\frac{d\sigma(\theta)}{d\Omega} d\Omega_\theta \quad = \quad \frac{\langle |S_{out}| \rangle \, r^2 D\Omega_\theta}{\langle |S_{in}| \rangle} \tag{3.14}$$

Since the incident power per unit area is

$$\langle |S_i| \rangle = \frac{\epsilon_0 c}{2} \left|E_0\right|^2 \tag{3.15}$$

Equation (3.15) becomes

$$\frac{d\sigma_{Th}(\theta)}{d\Omega} = \frac{r_e^2}{2}(1+\cos\theta) \tag{3.16}$$

where k_c is the Coulomb's constant defined as $k_c = \frac{1}{4\pi\epsilon_0}$ and $r_e = k_c e^2/m_e c^2$. The plot of the Equation 3.16 in presented in Figure 3.3 as a funciton of the scattering angle θ in units of barns.

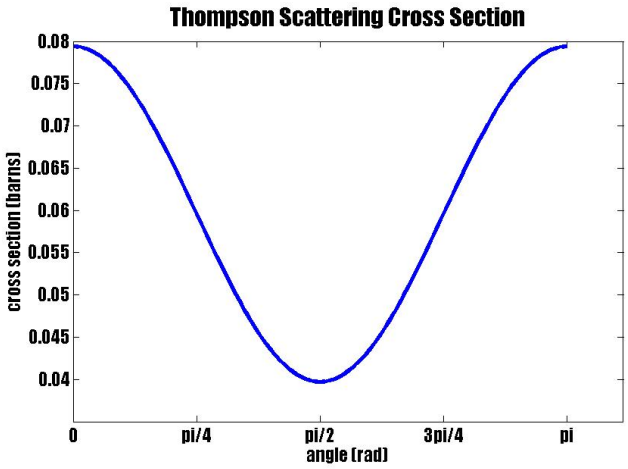

Figure 3.3: Thompson Scattering Cross Section

The minimum cross section happens for an anlge value of $\pi/2$, where the scattered

electron will move in 90^o angle to the diection of the incoming radiation. The maximum values are for small angles with respect the direction of the incoming radiation, either at forwards or backwards. The total scattering cross section is obatained by integration as

$$\sigma_{Th} = \int_0^{\pi} \sigma_{Th}(\theta) d\Omega_{\theta} = \pi r_e^2 \int_0^{\pi} \pi(1 + \cos^2\theta) \sin\theta d\theta = \frac{8}{3}\pi r_e^2 \tag{3.17}$$

The total cross section for Thompson scattering per electron is found to be about 0.665b, [Prussin, 2007].

3.2.1 Compton Scattering

Compton scattering is significant at intermediate photon energies between 200 keV - 1.5 MeV. It involves the inelastic scattering of the electromagnetic waves by an atomic electron, and the photon is reduced in energy and deflected from its original direction as shown schematically in Figure 3.4. A photon of energy E_0 is assumed incident on a free unbound electron. After the interaction, the electron is found moving at an angle of ϕ with a kinetic energy T_e and a photon with lower energy E' is found moving at the scattering angle θ.

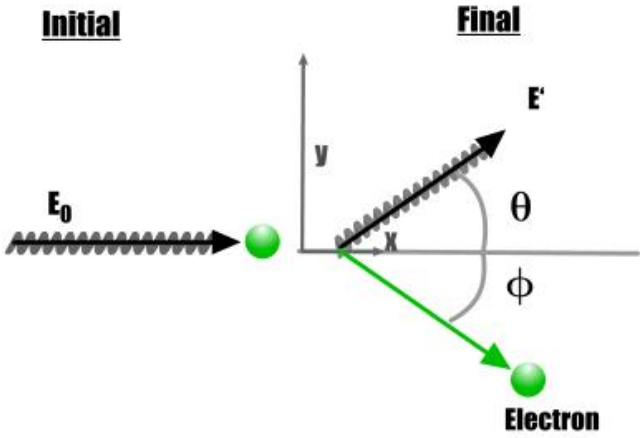

Figure 3.4: Schematic diagram of Comptom Effect

Using conservation of energy and momentum $E_0 = E' + T_e$ and $P_0 = P' + P_e$,

the characteristic properties of incident photon can be used to write the electron momentum as

$$P_e^2 = (P_0 - P')(P_0 - P') = P_0^2 + P'^2 - 2\,|P_0|\,|P'|\cos\theta \tag{3.18}$$

Then, the energy dependancce of the electron momentum

$$P_e^2 c^2 = E_e^2 - (mc^2)^2 \tag{3.19}$$

The electromagnetic wave energy ($E = pc$) is used in Equation(3.18) to obtain

$$E_e^2 - (m_e c^2)^2 = E_0^2 + E'^2 - 2E_0 E'\cos\theta \tag{3.20}$$

It is found that: [Bernstein et al., 2000].

$$E' = \frac{E_0}{1 + \alpha(1 - \cos\theta)} \tag{3.21}$$

where $\alpha = E_0/m_e c^2$ is the ratio of energies between the incident electromagnetic wave and the rest energy of the electron mass.

The compton electron has gained kinetic energy from the incident wave, threfore, the resulting electromagnetic wave has less energy, this difference is given by

$$E_0 - E' = E_0\left[\frac{\alpha(1 - \cos\theta)}{1 + \alpha(1 - \cos\theta)}\right] = T_e \tag{3.22}$$

The maximum electron kinetic energy is produce at $\theta = \pi$, whereas low electron energies are produced at forward angles. Application of the conservation of momentum in both x and y directions yield [Prussin, 2007].

$$\cot\phi = (1 + \alpha)\tan\frac{\theta}{2} \tag{3.23}$$

It is notable that when $\theta = 0$, $\cot\phi|_{\theta=0} = (1 + \alpha)\tan 0 = 0$. When $\phi|_{\theta=0} = \pi/2$ the incident photon produces the minimum energy transfered to the electron. When $\phi|_{\theta=\pi} = 0$ maximum energy is transfer to the electron and the electron moves in the

direction of the incident photon.

$$\frac{d_e\sigma_c(\theta)}{d\Omega} = \frac{r_e^2}{2}\left\{\left[1+\alpha(1-\cos\theta)^{-3}\right]\right. \\ \left.\left[\alpha\cos^3\theta+(\alpha^2+\alpha+1)(1+\cos^2\theta)-\alpha(2\alpha+1)\cos\theta\right]\right\} \quad (3.24)$$

A MatLab code was implemented to compute the differential cross section for various values of incident photon energy. The results are shown in Figure 3.5. As energy of the incident photon increases, the scattering becomes predominantly in the forward direction. However, for low energies, the cross section reduces to Thomson cross section discussed earlier and the scattering is equally likely to be forward or backward.

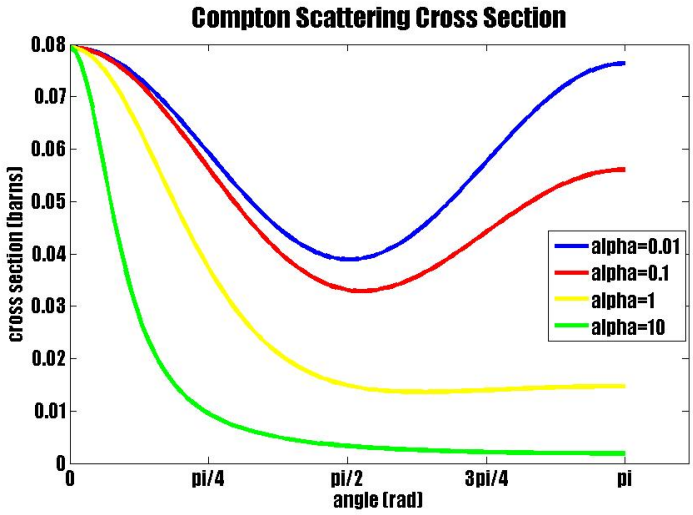

Figure 3.5: Compton Scattering Cross Section

3.2.2 The Photoelectric Effect

The photoelectric effect was initially demonstrated by Heinrich Hertz demonstrated 1880s. In the process a photon transfers all of its energy to an orbital electron, which is ejected with kinetic energy equal to the difference of the incident photon energy and the binding energy (ionization energy) needed to remove the electron. The range

of energies that produce the photoelectric effect is E $<$ 200 keV.

$$E_e = E_\gamma - BE_e \tag{3.25}$$

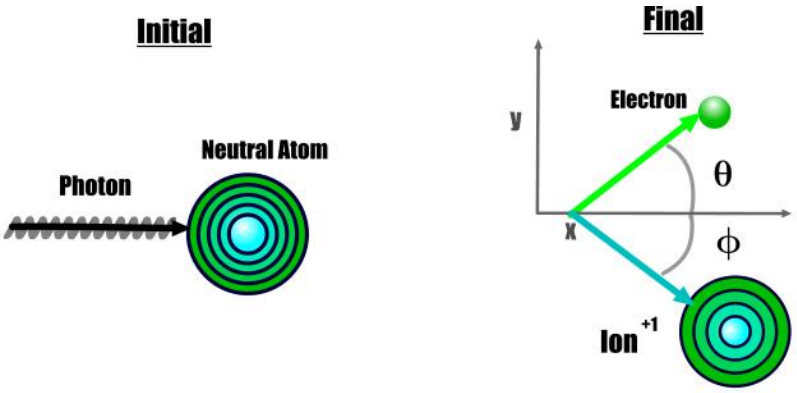

Figure 3.6: Schematic diagram of Photoelectric Effect

The recoil energy of the ion is generally negligibly small. The conservation of momentum requires that the electron must be bound, that is, the coupling of the electron to the atom must be strong enough that the system has a high probability for accepting the recoil energy and momentum. The more tightly bound the electron the higher will be the probability for the effective momentum transfer. Simplified models of the photoelectric effect generally make approximations that are applicable to the case that the photon energy is large compare to the binding energy of the ejected electron. The models preidict that the cross section for ejection of K electrons is approximately

$$\sigma_{pe,K} \approx \left(\frac{32}{\alpha}^7\right)^{1/2} \left(k_c \frac{e^2}{\hbar c}\right)^4 Z_e^5 \sigma_{Th} \tag{3.26}$$

where $\alpha = E_0/m_e c^2$ and $k_c(e^2/\hbar c) \approx 1/137$ is the fine structure constant[Prussin, 2007].

A plot of the cross section (Equation 3.26) as a function of the energy is shown in Figures 3.7 and 3.8. For the plot, aluminum and lead were chosen as shielding materials and silicon and germanium for the electronic materials. The cross sections,

as expected are large at low energies.

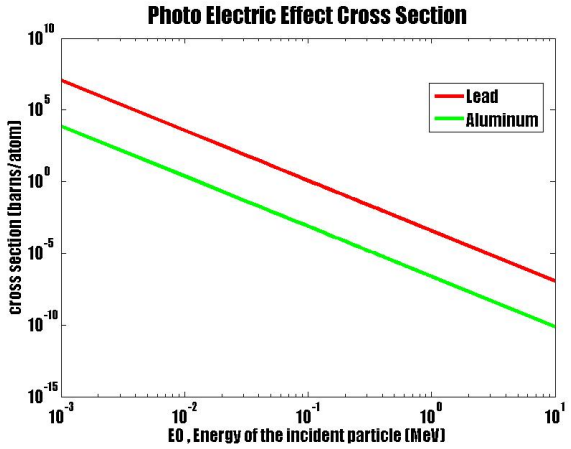

Figure 3.7: Photoelectic Effect Cross Section for Shielding Materials

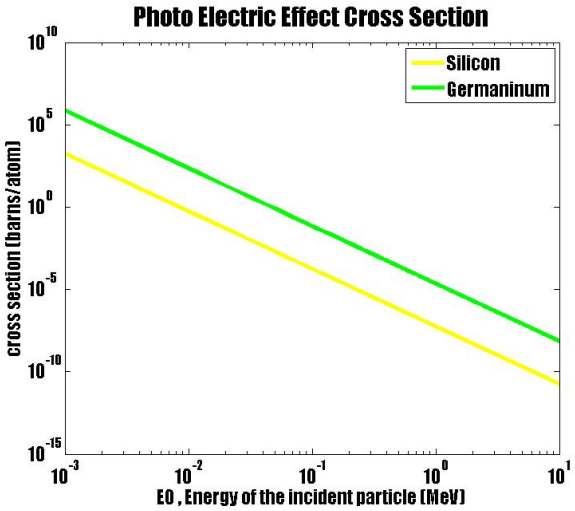

Figure 3.8: Photoelectic Effect Cross Section for Electronics Materials

3.2.3 Pair production

In pair production a photon disappears and an electron-positron pair is formed. Since the rest energy of an electron/positron is 0.511MeV, pair production requires a photon of at least 1.02MeV to occur and something extra to impair kinetic energy to the created particles as is shown in Figure 3.9, so usually it occurs higher energies (E>1.5MeV). The remainder of the photon energy is received as kinetic energy by the electron-positron pair

$$T_e = E_\gamma - 2m_e c^2. \tag{3.27}$$

Eventually the positron combines with an electron, and two photons are produced, each having an energy of 0.511MeV.

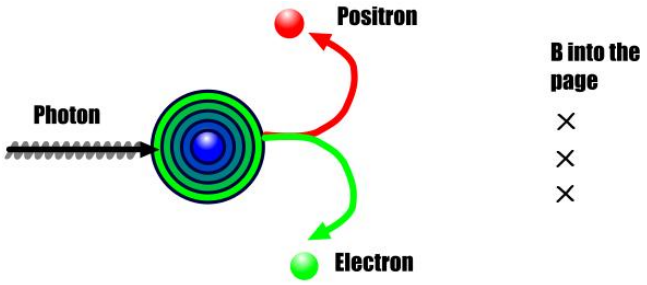

Figure 3.9: Schematic diagram of pair production

The total cross section for interaction with a nucleus, i.e., in the limit that screening of the nuclear charge by the atomic electrons is neglected, is given by the Bethe and Heitler formula,

$$_a\sigma_{pp} = Z^2 r_e^2 K_c \left[\frac{28}{9}\ln(2\alpha) - \frac{218}{27}\right]. \tag{3.28}$$

Conservation of energy and momentum show that the threshold for pair production in the field of a free electron is $4m_e c^2$. Pair production in the field of electrons is really only significant for very lightest elements [Davies et al. and Bethe and Maximon]. To plot the function described in Equation 3.28, a Matlab code was implemented and the results are shown in Figures 3.10a and 3.10b.

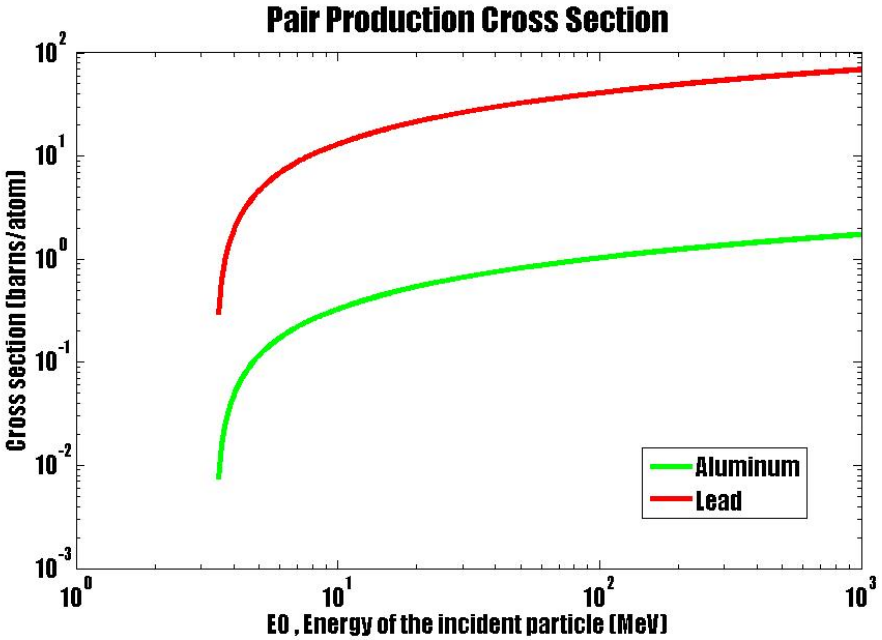

(a) Shielding materials

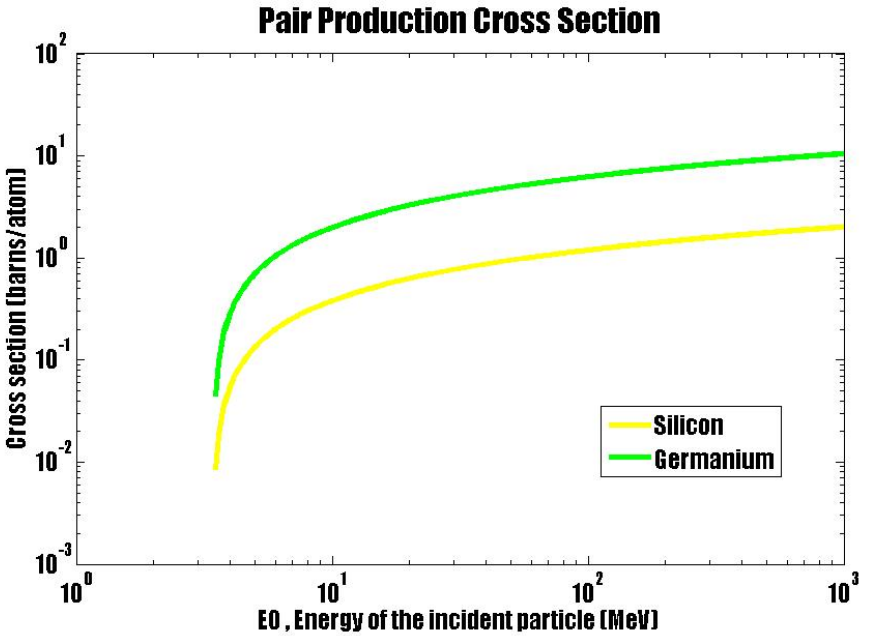

(b) Electronics materials

Figure 3.10: Pair Production cross section

As before aluminum and lead were chosen for shielding materials and silicon and germanium for electronics materials. The calculations are made for materials with a single element. More complex materials will need a different and more elaborate discussion about the cross section for pair production. The cutoff of the energy is about 3.4 MeV. This will be the energy required to generate a pair of electron-positron (0.511 MeV) per each particle. The extra energy may be given to the particles as kinetic energy so that the particles escape the nucleus force field.

The larger the value of σ, the more probable will it be for a particular reaction to occur. The total scattering cross section for photon is given as the sum of the three principal effects by:

$$\sigma_{total} = \sigma_{\text{photoelectric effect}} + \sigma_{\text{Compton scattering}} + \sigma_{\text{pair production}} \tag{3.29}$$

3.3 Charged Particle Interactions

The behavior of charged particles (α, β, p) passing trough matter is fundamentally different from that of neutral radiations (η , γ). Mostly, the charged particles strongly interact with the orbital electrons of the materials through which the particles move. The charged particles therefore are classified as *directly ionizing*. Additionally, the charged particle interactions can be subdivided in two cases based on mass: (1) heavy charged particles (α and p) and (2) light charged particles [Holbert, 2007].

3.3.1 Heavy Charged Particles Interactions

Heavy charged particles lose energy through interaction with the electrons in small steps. When the particle no longer has enough energy to ionize the material, it loses energy by nuclear collisions. As the particle slows, it captures electron(s) to form a neutral atom (e.g., proton becomes hydrogen, and alpha forms helium). The heavy particles slow down almost entirely due to coulombic interactions with the atomic electrons. Because of the large number of these interactions, the slowing down is nearly continuous. Ions are not easily deflected by atomic electrons and so the travel straight line paths. In contrast with the exponential decrease of neutrons and gamma

rays, the heavy particle has a well defined range of only a few centimeters in air, ever for quite energetic particles. Light charged particles, like beta particles and electrons pass trough matter, several possible processes occur including: The model of the energy loss of heavy charge particles can be made by assuming a particle with velocity $v \gg 0$ and mass $m_{HCP} \gg m_e$. The particle is incident upon a homogeneous isotropic medium. The only interaction that result in energy loss are those with electrons. The maximum energy loss in a elastic collision of a heavy charged particle with a free electrons is

$$\begin{aligned} \Delta E &= T_{HCP} - T'_{HCP} && (3.30) \\ &= T_{HCP}\left[1 - \left(\frac{m_{HCP} - m_e}{m_{HCP} + m_e}\right)^2\right] && (3.31) \\ &\approx \frac{4m_e}{m_{HCP}} T_{HCP} && (3.32) \end{aligned}$$

A very large number of collisions will be needed, on the average, for a heavy charged particle to come to rest in a medium. Because the small energy loss per collision and the assumption of an isotropic stopping medium, the trajectory is assumed to be linear and the energy loss is so small that the velocity of the particle can be considered constant.

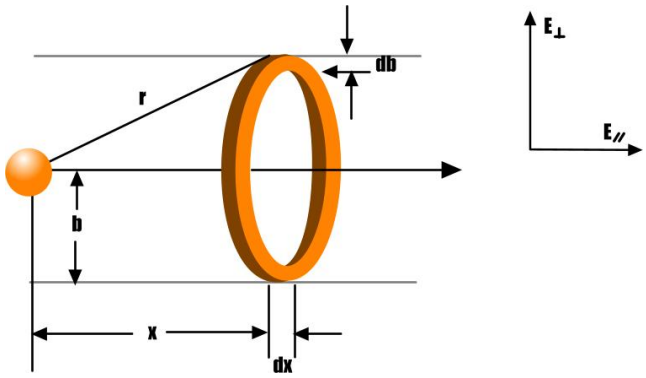

Figure 3.11: Schematic for the interaction of heavy charged particle with electrons in the annulus

In reference to the diagram shown in Figure 3.11, the energy loss model can be

discussed. The particle with charge Z and velocity v is moving in a medium of constant electron density. An electron located at a distance x and impact parameter b from its trajectory will experience a force

$$F = -K_c \frac{Ze^2}{r^2} = |eE| = e\left(E_\perp^2 + E_\parallel^2)\right)^{1/2} \tag{3.33}$$

The kinetic energy transfer to an electron is

$$T_e = k_c \frac{2Z^2e^4}{m_e b^2 v^2} \tag{3.34}$$

This result (Equation 3.34) can be used as the estimate energy transfer to all electrons with the same impact parameter. If n_e is the electron density, the number of electron with impact parameter b to $b + db$ in a differential distance dx along the heavy ion trajectory is just $2\pi n_e b db dx$. Using the previous result and the Equation 3.34 the total energy transfer (energy loss) can be integrated as

$$-\frac{dE}{dx} = 2\pi T_e n_e b db dx = k_c^2 \frac{4\pi n_e Z^2 e^4}{m_e v^2} \int \left(\frac{db}{b}\right) \tag{3.35}$$

To integrate over the impact parameter there are some constraints, at $b = 0$ the energy loss must tend toward ∞. So the minimum impact parameter is when the the maximum kinetic energy transfer occur.

$$\begin{aligned} (T_e)_{max} &= 2m_e v^2 \\ b_{min} &= k_c \frac{Z^2 e^4}{m_e v^2} \end{aligned} \tag{3.36}$$

Now, considering the bound energy of the electrons, especially the K and L electrons in high Z elements, an *effective ionization constant*, I, can be defined for each element of the periodic table nad is given in eV. Given I, energy transfers corresponding to $T_e < I$ are simply forbidden and impact parameters that are sufficiently large that they would produce energy transfers less that I will not contribute to integral

in equation 3.35.

$$I = k_c^2 \frac{2Z^2 e^4}{m_e b_{max}^2 v^2} \tag{3.37}$$

Or

$$b_{max} = k_c \frac{Ze^2}{v} \left(\frac{2}{m_e I} \right)^{1/2} \tag{3.38}$$

Using the limits for b_{min} and b_{max} in the integral of the equation 3.35 and adding the quantum mechanics corrections the Bethe-Bloch approximation is obtain:

$$-\frac{dE}{dx} = k_c^2 \frac{4\pi n_e Z^2 e^4}{m_e v^2} \ln \left[\frac{2m_e v^2}{I - (1 - \beta^2)} - \beta^2 \right] \tag{3.39}$$

where β can be obtained from:

$$T = \left(\frac{1}{\sqrt{1 - \beta^2}} - 1 \right) m_0 c^2 \tag{3.40}$$

The velocity ratio β can be determined from the nonrelativistic kinetic energy E_k and the rest energy of the proton (or alpha particle) as:

$$\beta = \left(\frac{2T_p}{E_0} \right)^{1/2} \tag{3.41}$$

Where

$$\begin{aligned} T_p &= \text{Kinetic energy of the proton} \\ E_0 &= m_0 c^2, \text{rest energy of the proton} = 938.3 MeV \\ m_0 &= \text{rest mass} MeV/c^2 \end{aligned}$$

The resulting equation is usually call the stopping power due to **ionization** [Prussin, 2007]. For these calculations, the effectivee ionization constant was taken from the epirical relation presented in [Pisacane, 2008]:

$$I \approx 9.1 Z_0 (1 + 1.9 Z_0^{-2/3}) \text{eV} \tag{3.42}$$

For alloys or complex materials, weighted contributions should be used based on

$$I = \exp\left(\frac{1}{n}\sum_i n_i Z_i \ln I_i\right) \tag{3.43}$$

Where

$$\begin{aligned} I &= \text{mean exitation energy of the alloy} \\ n &= \text{total number of electrons per unit volumen of alloy} \\ I_i &= \text{mean excitation energy of each material} \\ n_i &= \text{electron density of material } i \end{aligned}$$

To calculate the number density of electrons in the target:

$$n_{target} = \frac{N_A \rho_{target} \eta_{target}}{M_{target}} \tag{3.44}$$

Where

$$\begin{aligned} n_{target} &= \text{number density of electrons } e/m^3 \\ N_A &= \text{Avogadro's number } molecules/kmol \\ \rho_{target} &= \text{desnity of target material } kg/m^3 \\ \eta_{target} &= \text{number of electrons per molecule } e/molecule \\ M_{target} &= \text{molecular mass of target material } kg/mol \end{aligned}$$

The graphics shown in Figures 3.12a and 3.12b are plot of the stopping power of protons are calculated for different materials using Equation 3.39, and are divided according to their functions either as shielding or as electronic components materials.

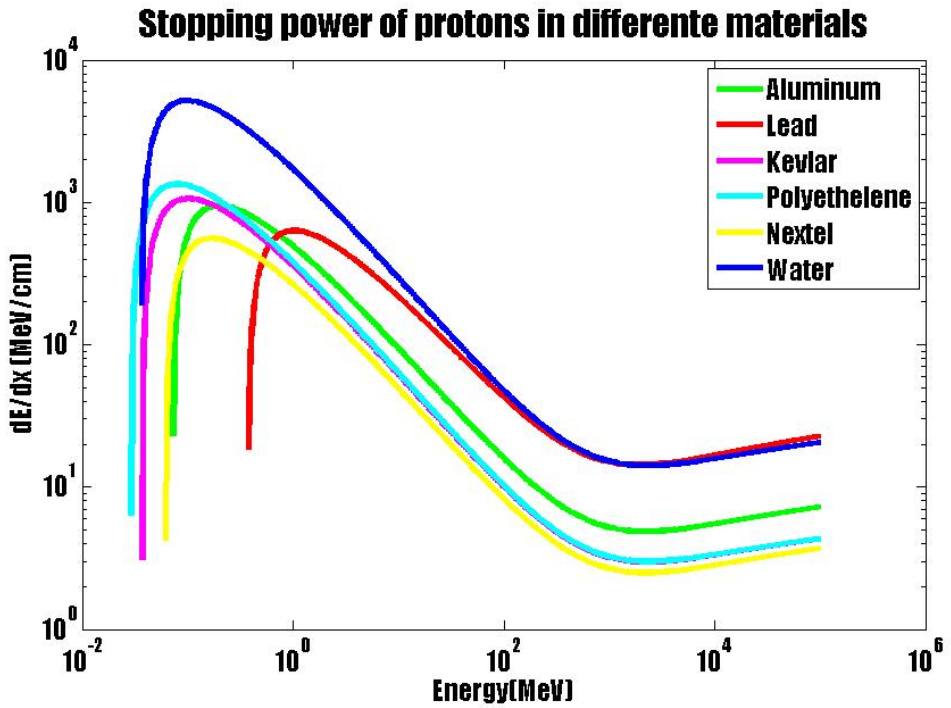

(a) Shieling materials

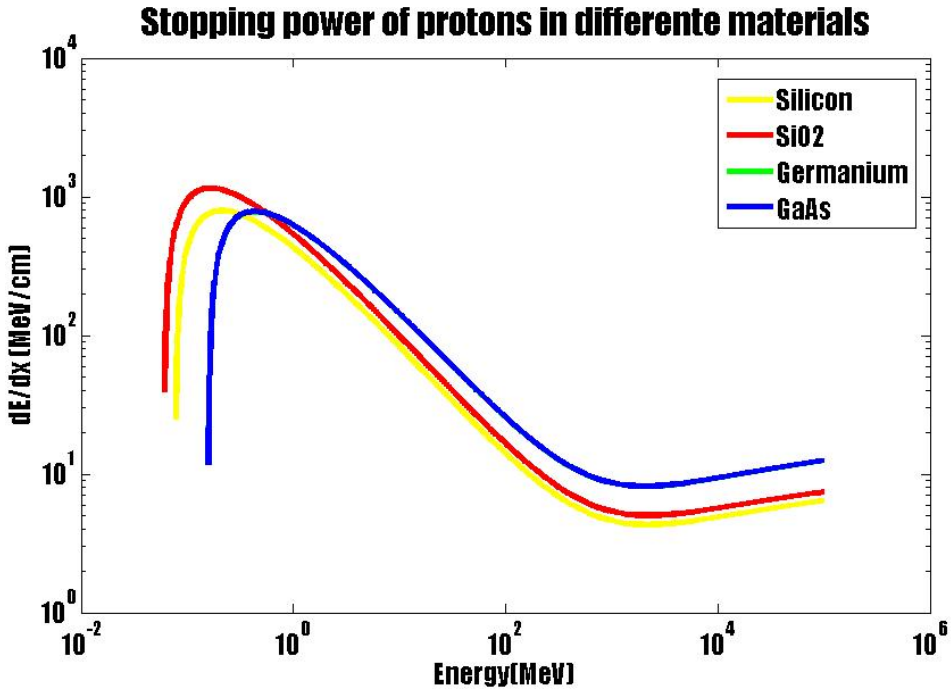

(b) electronics materials

Figure 3.12: Stopping Power of Protons in some materials

Analyzing for the shielding materials first, Figure 3.12a , the material that best behave as shielding for protons is water, but the implementation of water as a shielding is difficult. Comparing the commonly used materials that can be used as shielding for protons of lower energy (< 0.3 MeV) is the polyethelene, the dE/dx is greater, which means that a greater amount of energy is deposited in a unit distance. For protons with energies close to 1 MeV the best shielding material is aluminum, in the graphic the curve (in green) dominates over the over curves, in a small interval around 1 MeV, which means that approximately 100 Mev are deposit in 1 cm traveling through aluminum. Then, for energies greater than 1 MeV the best material is lead, because of its high density of electrons, high Z number, and high ionization constant.

For the materials of electronic components in Figure 3.12b, GaAs is the most sensitive material to damage due to interaction with protons. Protons with energy < 10 MeV will transfers about 1000 MeV per cm.

For α particle and heavy ions of the same total kinetic energy, the computation was made in reference to Equation 3.39 but changing the parameters for the incoming particles. Heavier particles will be expected to travel shorter distances before their kinetic energy falls to zero. Making a comparison between the graphics of the stopping power of protons and alpha particles, it is clear that the alpha particles deposit a greater amount of energy per unit distance. In Figure 3.13a for the materials comunly used for shielding for energies bellow 2MeV the materials that best behaves as shielding is polythene again for alpha particles. Then, Above the 10MeV lead and water are dominant .

Besides the stopping power it is also important the distance penetrated by the heavy ion before it is 'stopped', and the energy deposited along its trajectory. The distance traversed by a heavy charged particle is known as the *average range* of the particle in the medium in question. To estimate this average range the equation 3.45 can be used.

$$R = \int_{E_0}^{0} \left(\frac{dE}{dx}\right)^{-1} dE \tag{3.45}$$

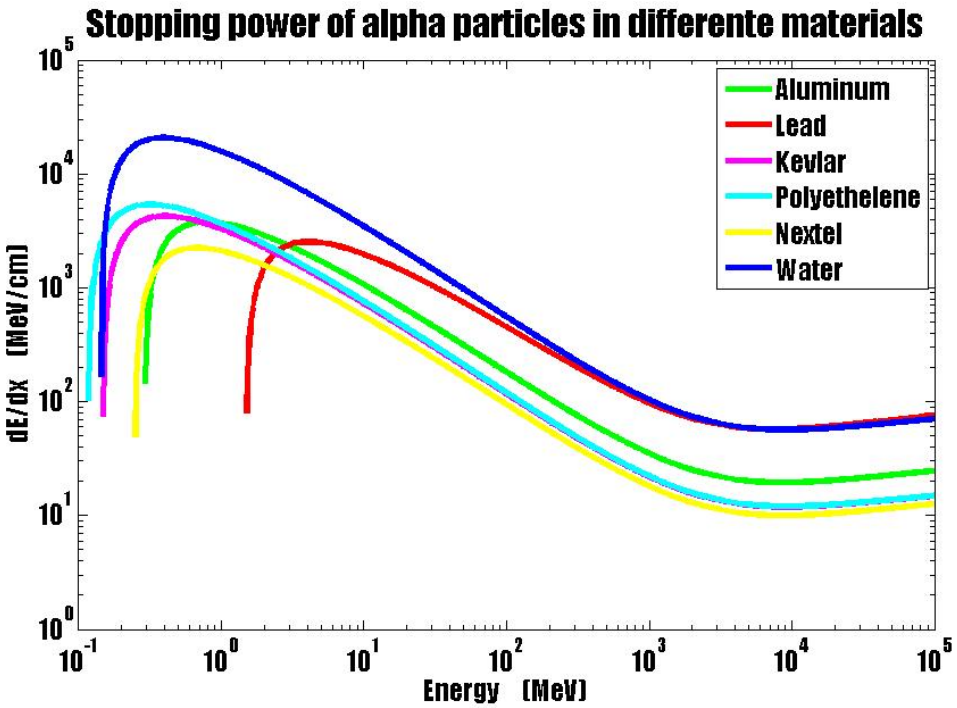

(a) Shielding materials

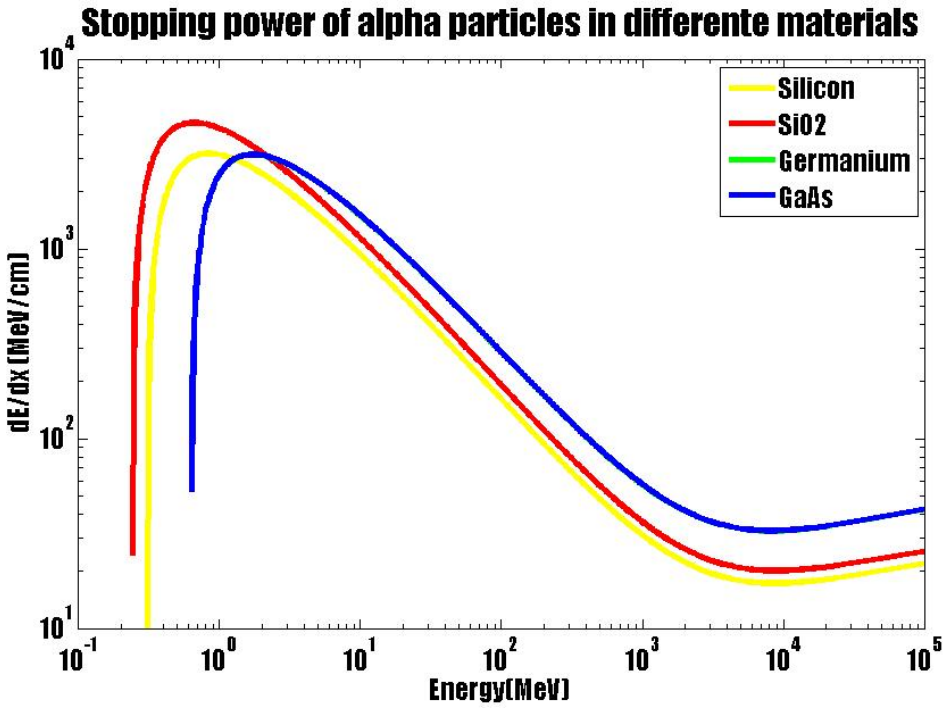

(b) Electronic materials

Figure 3.13: Stopping power of alpha particles in some materials

The initial energy of the ion, the energy at $x = 0$, is defined as E_0. The final energy is, of course, zero when the ion has traversed the distance $x = R$.

$$T = \left(\frac{1}{\sqrt{1-\beta^2}} - 1 \right) m_0 c^2 \tag{3.46}$$

$$\frac{dT}{d\beta} = \frac{m_0 c^2 \beta}{(1-\beta^2)^{3/2}} \tag{3.47}$$

Utilizing the relativistic expression for the kinetic energy of a particle in equation 3.46 and differentiating it with respect β , then substituting the result in 3.39 the final expression for the universal function for all ions traversing a given medium can be rewritten as:

$$R = \frac{(m_0 c^2)(m_e c^2)}{k_c^2 4\pi Z^2 e^4} \int_{\beta(E_0)}^{0} f(\beta) d\beta \tag{3.48}$$

Where

$$f(\beta)d\beta \frac{\beta^3}{n_e(1-\beta^2)^{3/2} \ln\left[\frac{2m_e c^2 \beta^2}{I(1-\beta^2)} - \beta^2\right]} d\beta \tag{3.49}$$

A matlab code was implemented to plot the graphics for different materials. It was found a singularity or the $f(\beta)$ at the point where

$$\left[\frac{2m_e c^2 \beta^2}{I(1-\beta^2)} - \beta^2 \right] = 0 \tag{3.50}$$

Because the $\ln 1 = 0$ and it creates and point of singularity when divided by zero. Let $\frac{2m_e c^2 \beta^2}{I} = A$ and solving for β

$$\frac{A\beta^2}{1-\beta^2} - \beta^2 = 1 \tag{3.51}$$

$$A\beta^2 = (1-\beta^4) \tag{3.52}$$

$$\beta^4 + A\beta^2 - 1 = 0 \tag{3.53}$$

Using the quadratic formula

$$\beta^2 = \frac{-A \pm \sqrt{A^2+4}}{2} \tag{3.54}$$

As a result the point of the singularity is

$$\beta = \sqrt{\frac{\sqrt{A^2+4}-A}{2}} \tag{3.55}$$

After modifying the formula usng Taylor's expansion around this point the integration was made and the final plots were obtained. In the Figures 3.14a and 3.14b the particles stop easier in a shorter distance for Nextel, so a proton moving with a energy of 10MeV will stop around 1mm. The range differ from material to material, in this case lead is the one with the smallest average range function, and it is expected because the LET (or stopping power) for lead is greater. In the case of alpha particles, as in Figures 3.15a and 3.15b, the average range is reduced by almost an order of magnitude, because the alpha particles are moving slower, so it will come to stop in a smaller distance. In Figure 3.15a the main conclusion that can be extracted is that for alpha particles over the range of 10MeV water could be a good shielding, and the thickness needed does not exceed a few mm.

The simple fact that can be learned from these model calculations and the simulations is that the range of heavy charged particles in matter is generally quite small, owing to the very large number of collisions that take place with the electrons. As the heavy ions moves through the matter there will be some probability that it will 'pickup' an electron an even some probability that an electron bound to it can be taken up once again, by the stopping medium. The probability of capture or release depends upon the binding energies of the electrons and the energies of the electrons in the stopping medium. On average, especially for ions of high atomic number, there will be a continuous reduction in the ionic charge as it slows down. Because the stopping power depend upon the square of the ion's charge, the process of charge exchange will lead to significantly larger ranges that estimated by equation 3.39 when the initial velocity is too small.

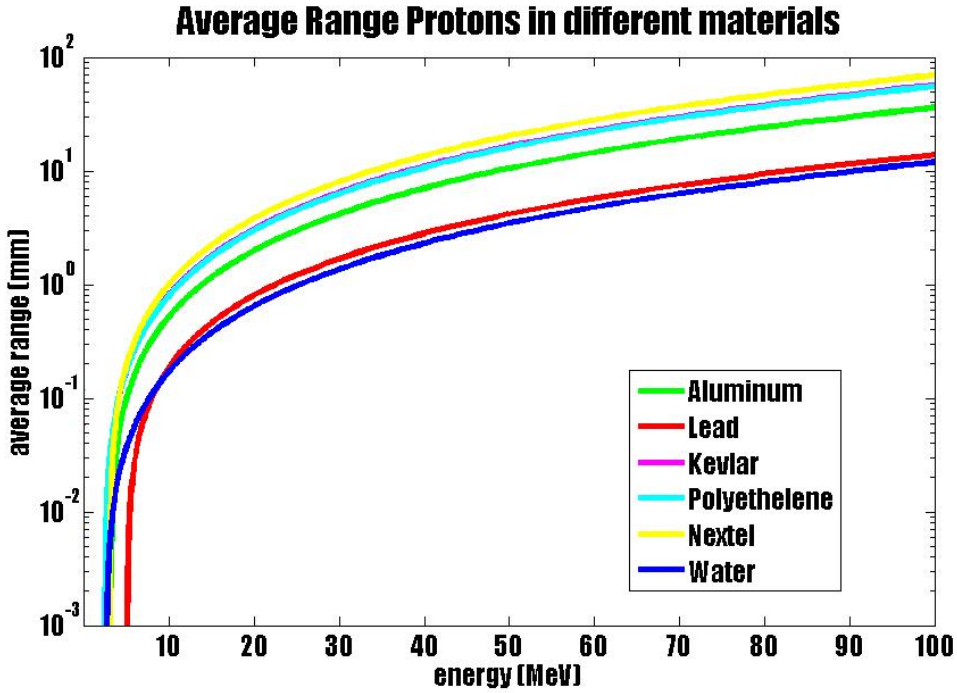

(a) Shielding Materials

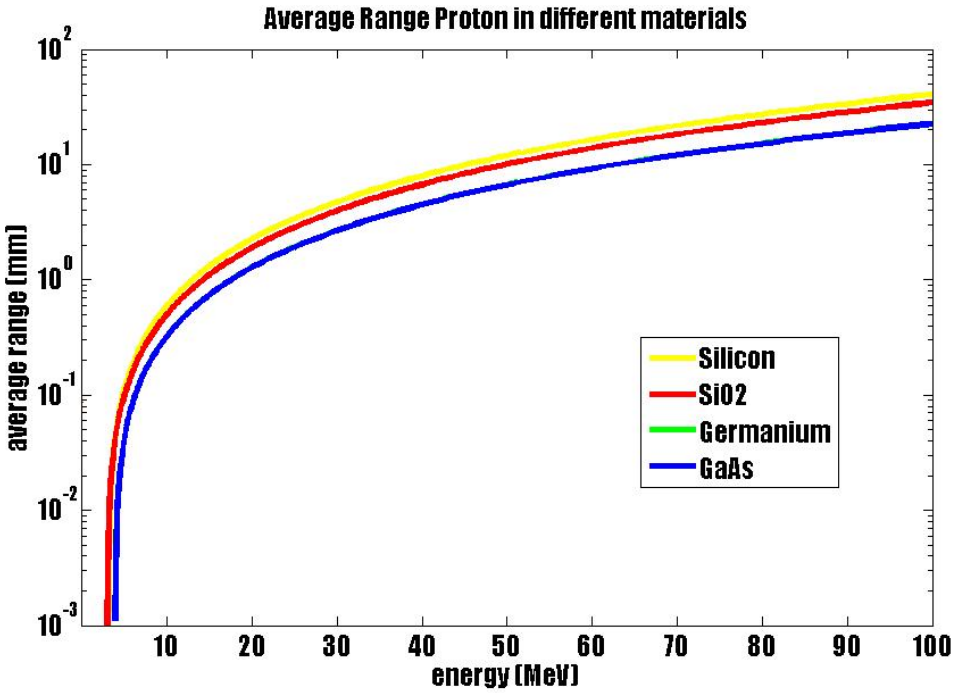

(b) Electronics Materials

Figure 3.14: Average Range of Protons in some materials

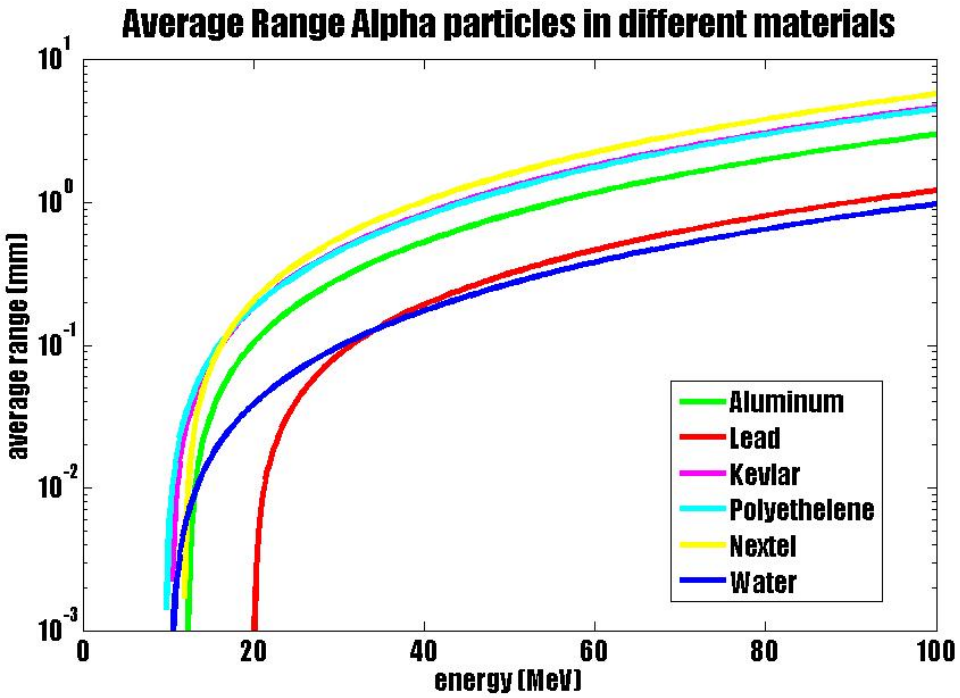

(a) Shielding Materials

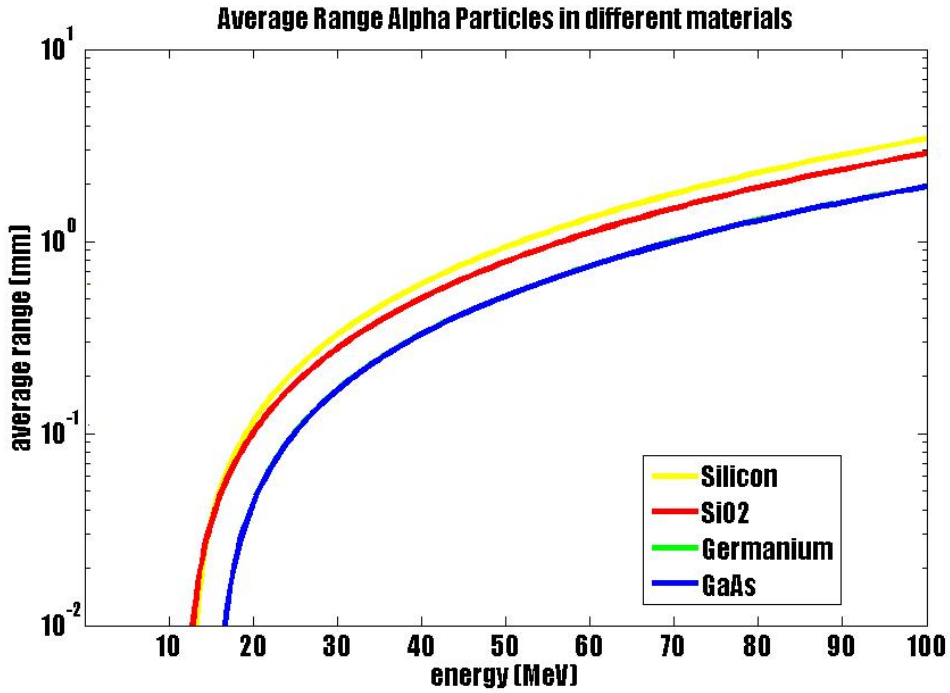

(b) Electronics Materials

Figure 3.15: AverageRange of Alpha Particles in some materials

At low energies, there is a significant probability that ion-atom and ion-ion collisions will be effective in the transfer of energy from the heavy ion to the stopping medium. This mechanism is referred to as *nuclear stopping* as opposed to the electronic stopping, that is considered before. Such collisions involve partners of heavy mass, sufficiently large that they can actually cause an ion in a lattice to be ejected from its normal site. Nuclear stopping is especially important for heavier ions and it reduced the range of an ion relative to that given by the model when it is only considering the interactions with electrons. This suggests that measurements of the stopping power and range of proton in matter can serve as reference for the stopping of all other ions. Because the only difference between the stopping power of proton and any other heavy ion in a given material is the ionic charge of the ion for the same velocities.

In the table 3.2 are the properties of the materials that were used to calculate the stopping power and the average range. As is clear in the table, the properties of *Ge* and *GaAs* are close, therefore in the graphics presented for the electronics material of different properties, the curves belonging to these materials are overlap, and in most cases they appear as one. Using this calculations, an easy acces table

Material	e per molecule	density kg/m3	I eV	molecular mass
Nextel	608.0	2700.0	136.2	2490.2
Kevlar	124.0	1440.0	81.4	238.0
Water	10	1000	79.16	18
Polyethelene	16.0	1300.0	64.0	28.0
Aluminum	13.0	2700.0	158.9	26.7
Lead	82.0	11350.0	821.3	207.2
Silicon	14.0	2329.0	169.1	28.1
Si02	30.0	2648.0	132.6	60.0
Germanium	32.0	5323.0	346.1	72.6
GaAs	64.0	5316.0	346.2	144.6

Table 3.2: Properties of Materials used to calculate the stopping power and averge range

is presetend in table 3.4 , where a direct corelation can be made. For proton or

alpha particles interacting with several materials, either for electronic or shielding analysis, the stopping power, the Average range, and the total energy deposited are tabulate,i. e. a proton with a kinetic energy of $1MeV$ interactin with Nextel, will have a stopping power of $48.3MeV/cm$, an average range of $1.1mm$. Multiplying these two valuese can be obtained the total energy deposited in the material, for this example it was $5.3MeV$. The theory said that the proton will inpair less than $10MeV$ so the result is in agreement of that prediction. To corroborate the values obtained in the table 3.4, a sofware of nuclear physics simulation was used. SRIM (Stopping and Range of Ions in Matter) sofware, is a group of programs which calculate the stopping and range of ions into matter using a quantum mechanical treatment of ion-atom collisions. SRIM is based on a Monte Carlo simulation method, namely the binary collision approximation with a random selection of the impact parameter of the next colliding ion. The folowing Figures are plots made with SRIM showing the posible trajectories of the ions (at different energies) within a given material and how long can they travel before they they finally stop. The deviation from the original linear trajectory is called *straggle*.

Lead and aluminum where the materials chosen to do the comparison, betwen the calculations made and the result obtained with SRIM. Figures 3.16 and 3.17 show the trajectories and the distribution for protons at different energies ($10MeV$, $100MeV$, $1GeV$) in acordance to the ones presented in the table 3.4. The computation of the average range using the matlab code and the resutls of the Montecarlo modeling of SRIM agree accurately in two decimal places of the average range values. Taking Lead as an example, for an incident proton of 100MeV the computation result for the average range is about $14.17mm$ and for the same proton in Lead the average range acording to the SRIM simulation is about $14.2mm$.

Particle	Material	Energy (MeV)	Stopping Power (MeV/cm)	Average Range (mm)	Total Energy Deposited (MeV)
Protons	Aluminum	10	93.62	0.6181	5.7866522
		100	15.82	36.26	57.36332
		1000	5.71	1415	807.965
	Lead	10	215.1	0.3158	6.792858
		100	41	14.17	58.097
		1000	14.95	497.9	744.3605
	Kevlar	10	63.2	0.9	5.688
		100	10.13	56.18	56.91034
		1000	3.23	2238	722.874
	Polyethelene	10	64.2	0.9	5.778
		100	11.13	56.18	62.52834
		1000	3.23	2238	722.874
	Nextel	10	48.83	1.1	5.3713
		100	8.16	70.35	57.4056
		1000	2.6	2729	709.54
	Silicon	10	81.6	0.6963	5.681808
		100	13.95	41.26	57.5577
		1000	4.5	1587	714.15
	SiO2	10	96.44	0.57	5.49708
		100	16.61	34.89	57.95229
		1000	5.37	1355	727.635
	Germanium	10	142.2	0.419	5.95818
		100	25.46	22.87	58.22702
		1000	8.6	852	732.72
	GaAs	10	142.2	0.419	5.95818
		100	25.46	22.87	58.22702
		1000	8.6	852	732.72

Table 3.3: Stoppig Power, Average Range and total energy ditribution of protons in different materials

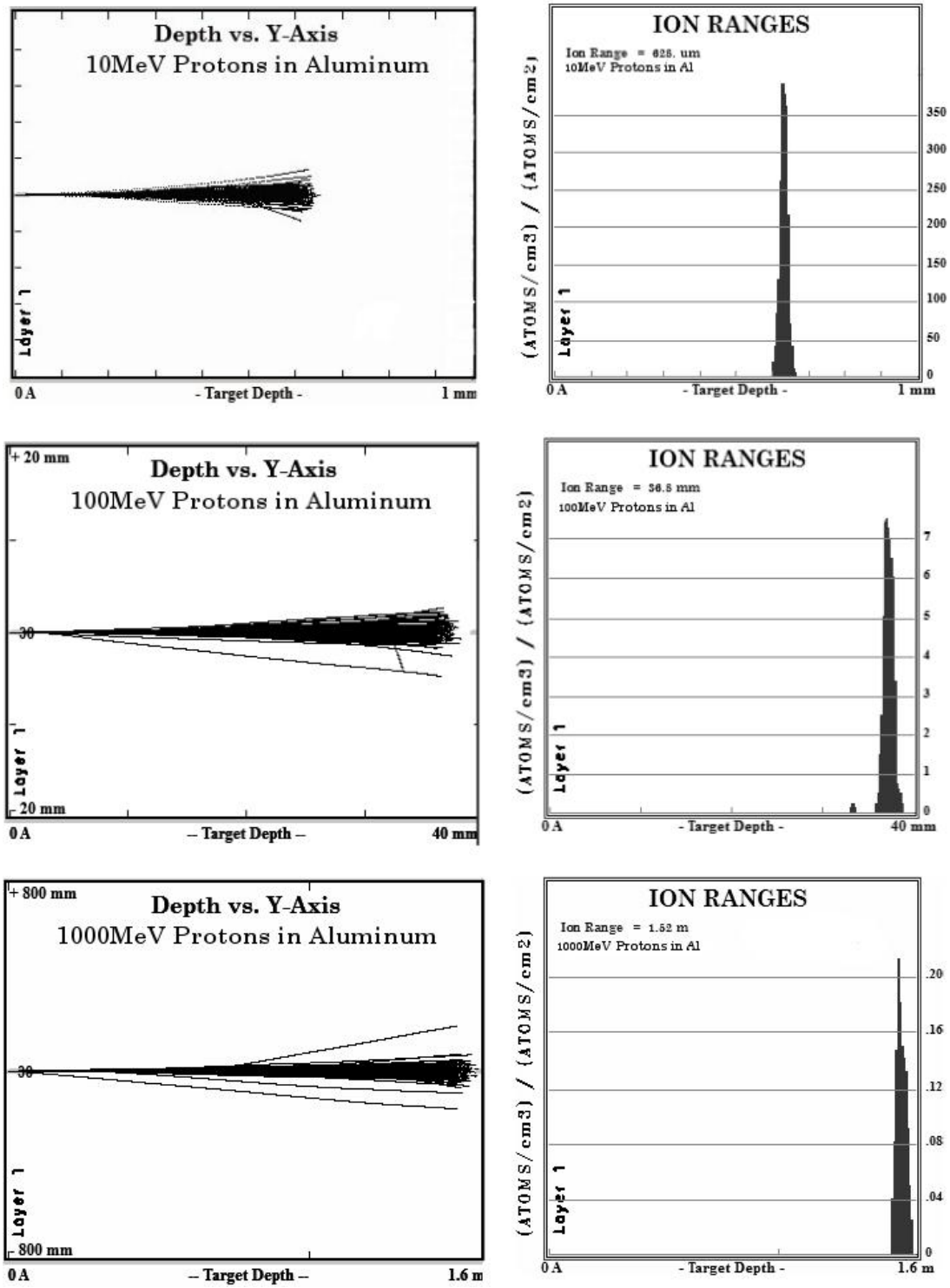

Figure 3.16: Protons trajectories and distribution in an Aluminum target at different energies. Using SRIM

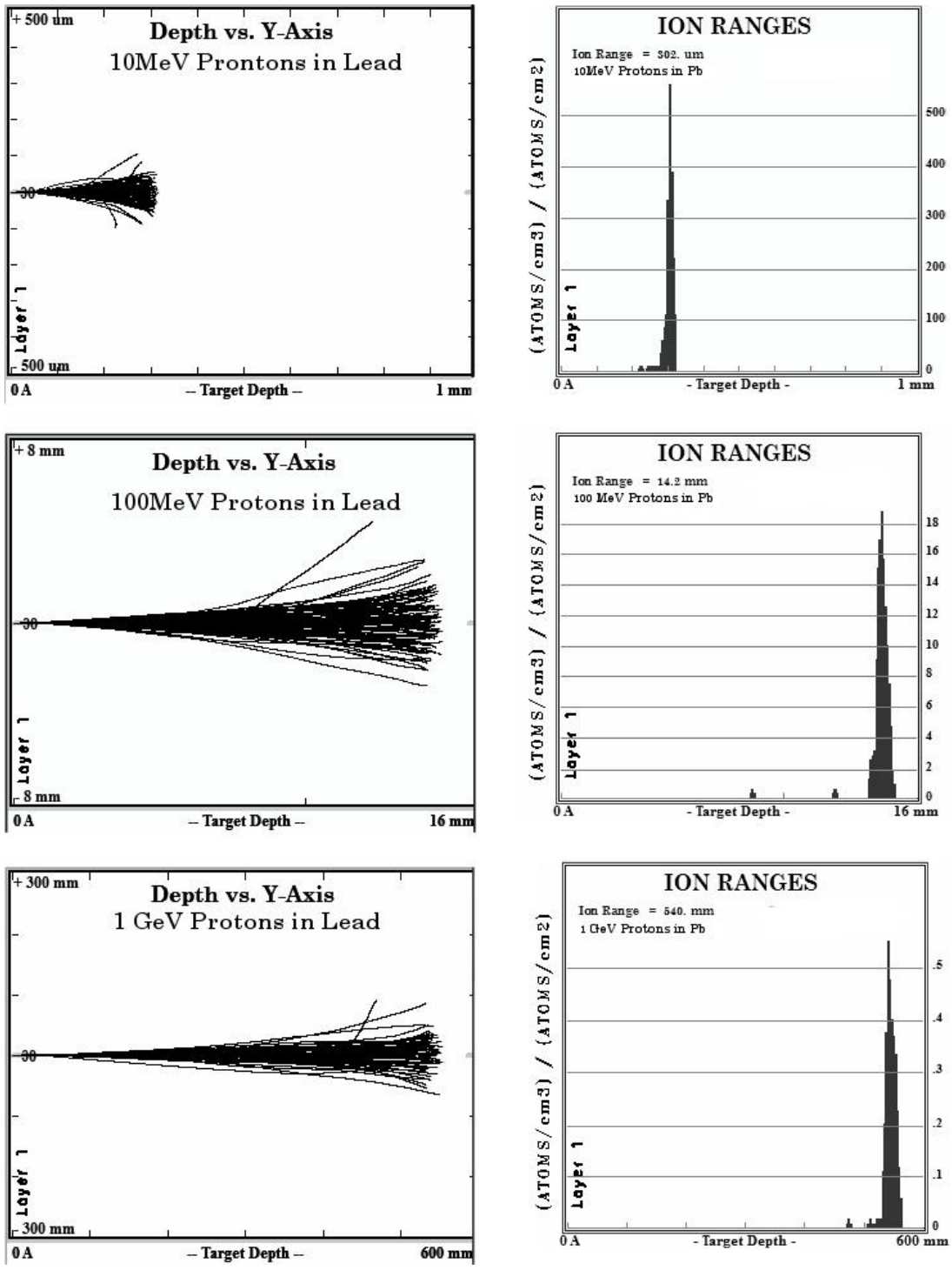

Figure 3.17: Protons trajectories and distribution in a Lead at different eneries. Using SRIM

Particle	Material	Energy (MeV)	Stopping Power (MeV/cm)	Average Range (mm)	Total Energy Deposited (MeV)
Alpha Particles	Aluminum	10	1055	0.05	5.275
		100	180.4	3.1	55.924
		1000	34.75	173	601.175
	Lead	10	1956	0.05	9.78
		100	453	1.3	58.89
		1000	95.49	64	611.136
	Kevlar	10	715	0.07	5.005
		100	115.9	4.67	54.1253
		1000	1009	269.3	27172.37
	Polyethelene	10	757.3	0.07	5.3011
		100	119	4.67	55.573
		1000	22.02	269.3	592.9986
	Nextel	10	558.2	0.11	6.1402
		100	93.84	6.07	56.96088
		1000	17.94	333.2	597.7608
	Silicon	10	925.3	0.0065	0.601445
		100	159.3	3.5	55.755
		1000	30.78	194	597.132
	SiO2	10	1129	0.055	6.2095
		100	189.3	2.97	56.2221
		1000	36.14	165	596.31
	Germanium	10	1489	0.046	6.8494
		100	282.9	2.03	57.4287
		1000	56.7	103.9	589.113
	GaAs	10	1489	0.046	6.8494
		100	282.9	2.03	57.4287
		1000	56.7	103.9	589.113

Table 3.4: Stoppig Power, Average Range and total energy ditribution of Alpha particles in different materials

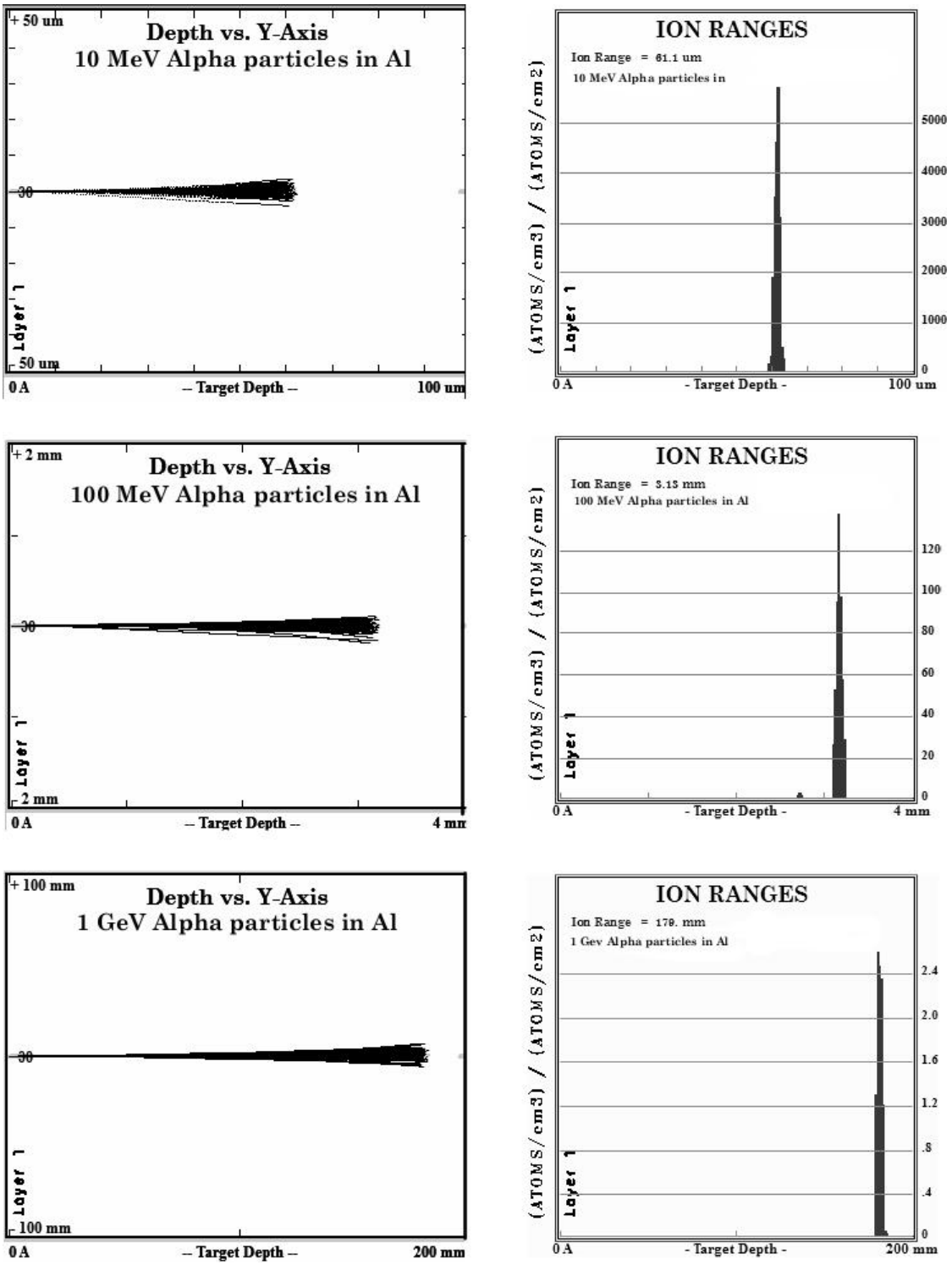

Figure 3.18: Alpha particles trajectories and distribution in a Aluminum at different eneries. Using SRIM

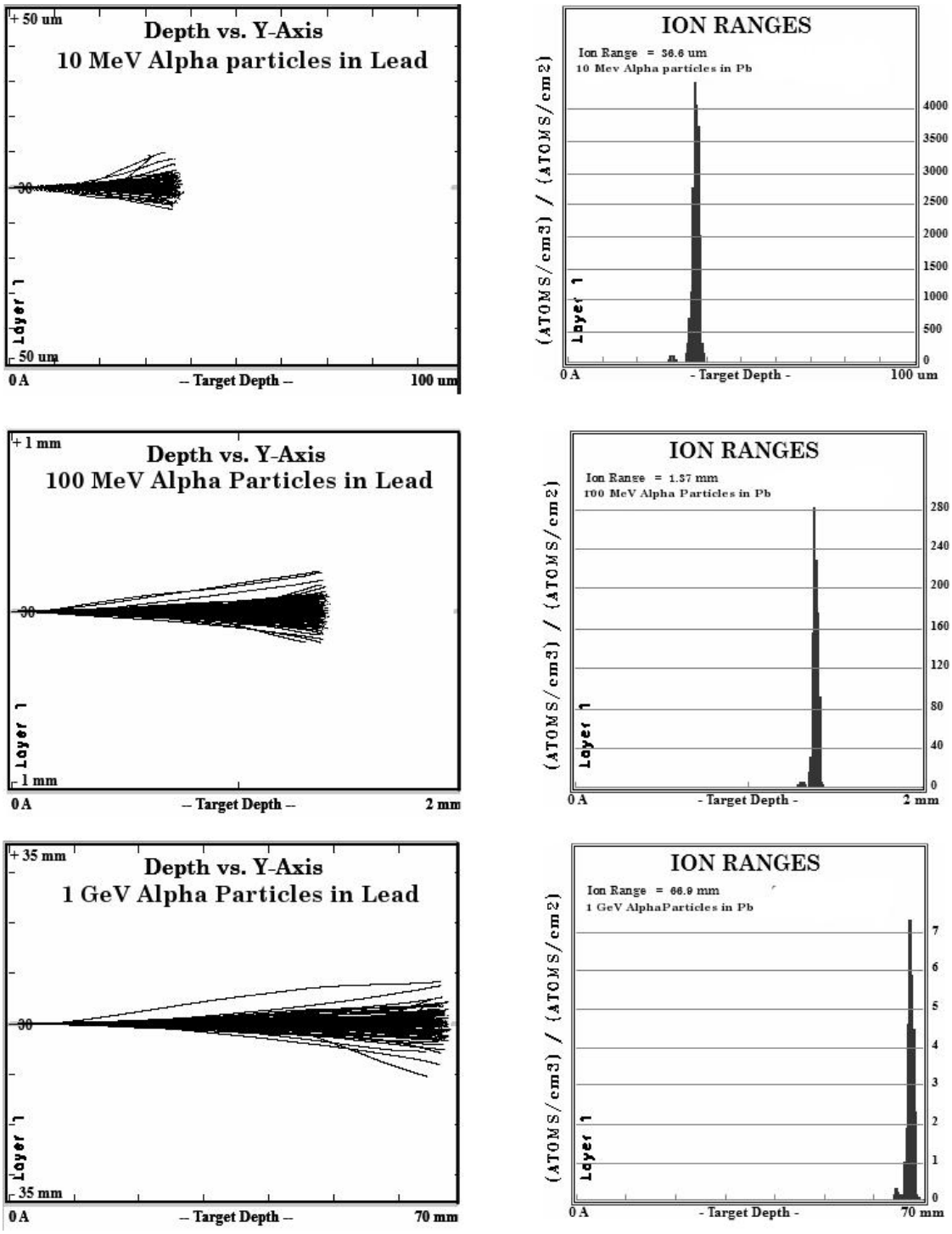

Figure 3.19: Alpha particles trajectories and distribution in a Lead at different eneries. Using SRIM

3.3.2 Electrons interactions with matter

The model of the heavy ion was linear and the time required for interaction with an electron was so short that an impulse approximation can be used to estimate the average energy transfer. Similarly, in this section the interaction of high-energy electron with the electron in the stopping medium is discussed however the assumption of the linear trajectory is not satisfied.

A single collision of a projectile with a target, when the two have identical masses, can result in the complete transfer of the projectile kinetic energy. The model describing the scatter of electrons on electrons there are no means of identifying which of the particles was the projectile and which was the target after the collision. A head-on collision, in which all the kinetic energy of the projectile is transferred to the target electron, will appear as no collision at all, the target will simple move away from the site of the interaction with exactly the same kinetic energy as the projectile had.

The classical model to understand the stopping power of electrons in matter is given in equation 3.39. The stopping power is not dependent upon the mass of the charged projectile. It only depends on the velocity. Consequently, the idea of stopping power describing the energy loss along the linear trajectory of the projectile can be transformed to one that describes the energy loss along the *actual* trajectory, no matter how nonlinear it is, the same basic physics should apply. The result for the energy loss of electrons by ionization can be written in the form

$$-\left(\frac{dE}{dx}\right)_{e,ion} = k_c^2 \frac{4\pi n_e e^4}{m_e v^2}\left[\ln\frac{2m_e c^2}{I} + \ln(\gamma-1) + \frac{1}{2}\ln(\gamma+1) - \left(3+\frac{2}{\gamma}-1\gamma^2\right)\ln 2^{1/2} + \frac{1}{16} - \frac{1}{8\gamma} + \frac{9}{16\gamma^2}\right] \quad (3.56)$$

Where $\gamma = (1-\beta^2)^{-1/2}$. A direct comparison between equations 3.39 and shows that the constants preceding the bracketed terms as wll as the first term in brackets are identical if $Z = 1$. According to the graphics in Figure 3.20 the stopping power of electrons and protons by ionization do not differ by more than about 13% over the enery range of $0.01 - 10MeV$. As a result, the stopping power by ionization of

electrons is the same as that of protons with the same energy.

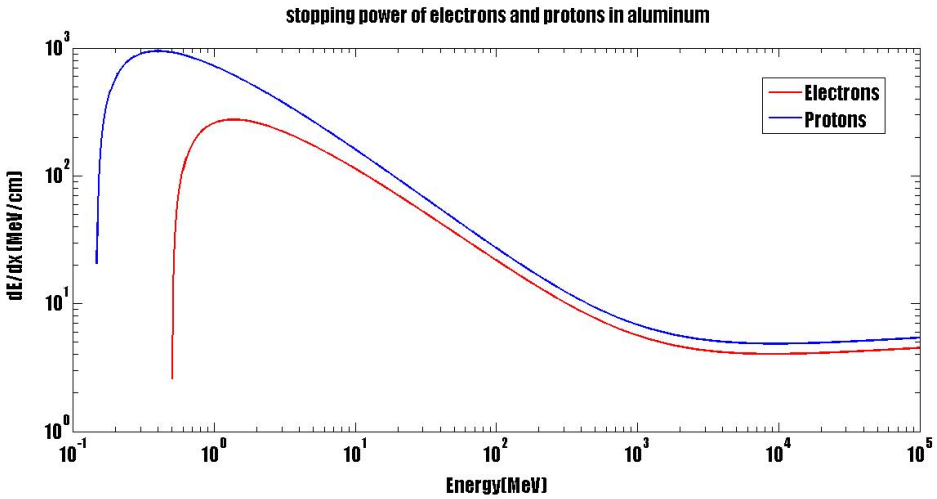

Figure 3.20: Stopping Power of Electrons and Protons in Aluminum

Classically when a charge is moving in an electric field it will emit energy as electromagnetic radiation. The probability of emission of electromagnetic energy is inversely proportional to the square of the mass of the particle. Accordingly, energy loss by emission of electromagnetic radiation is general negligible for heavy ions such as protons, but can be significant in the case of the stopping of electrons . This radiation is known s *bremsstrahlung*, literally translated from German to English as 'braking radiation'. The probability for bremsstrahlung in the field of the nucleus is proportional to the square of the atomic number.

Large angle scattering difficults the calculation of the range of electrons in matter. For practical applications, a number of studies have combined experimental determination of the range of monoenergetic electrons and electrons from β decay to develop useful correlations for range estimations. The range in b/cm^2 is parameterized as the Katz-Penfold formula, these represent empirical fits to experimental data on the range of electrons in aluminum:

$$\begin{aligned} \overline{R} &= 0.412E_n, n = 1.265 - 0.0954\ln(E) \quad (0.01 < E < 3MeV) \\ &= 0.530E - 0.106 \quad (2.5 < E < 20MeV) \end{aligned} \tag{3.57}$$

Given the ranges of aluminum, the approximations for the ranges of electrons in other materials composed of the lighter elements. This relies on the fact that for all elements wit $Z \leq 20$, the N/Z ratio of isotopes found in nature is ≈ 1 If ρ is the mass density and A and Z are the mass and atomic number of the element in question the electron density is given by:

$$n_e = \frac{\rho}{A} Z N_0 \approx \frac{\rho Z N_0}{2Z} = \frac{\rho N_0}{2} \tag{3.58}$$

Therefore any material composed of light elements will have the same areal electron density. The range of electrons in any materials composed of light elements will be approximately the same as the range in aluminum.

3.4 Nuclear Interactions

Since neutrons are uncharged they interact directly with the nucleus. Since the nucleus is considerably smaller than the atom, compared to charged particles and the nuclear force has very short range, neutrons can travel large distances in the material before an interaction occurs. However, a neutron that moves close enough to the target nucleus will experience the strong interaction. In the process it may simply scatter away or if it loses enough of its energy, it may be captured by the nucleus resulting in an unstable (radioactive) nucleus. The radioactive nucleus, in turn, undergoes a nuclear transformation and releases secondary ionizing radiation-particles in the material. Alternatively, the incident neutron may pick up a nucleon leaving an unstable nucleus behind. An illustration of these possible reactions is shown in Figure 3.21.

For example, a neutron may be captured by a silicon atom and produce the unstable isotope of magnisium, ^{25}Mg, as shown in the reaction below in Equation 3.59.

$$n \quad + \quad {}^{28}Si \quad \rightarrow \quad 2p \quad + \quad 2n \quad + \quad {}^{25}Mg* \tag{3.59}$$

The magnesium isotope in turn decays yielding Helium and carbon and a neutron

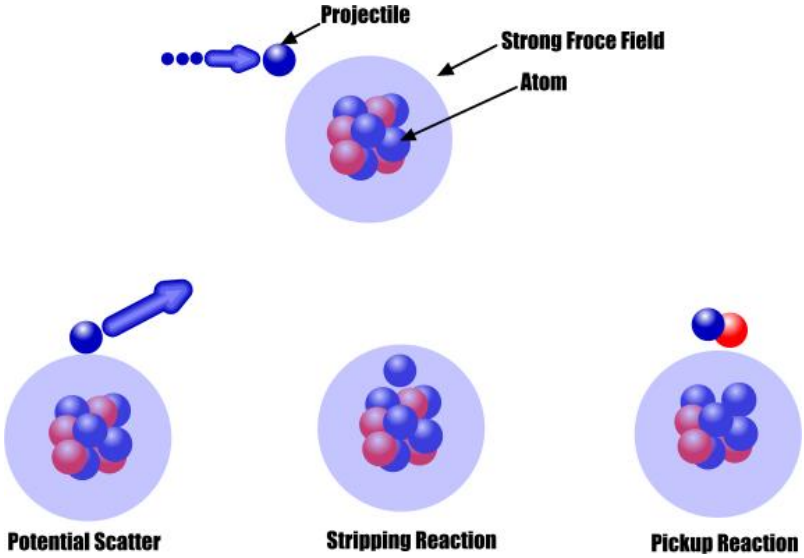

Figure 3.21: Possible Nuclear Reactions

leading to a cascade of such reactions , like the one presented in Equation 3.60.

$$^{25}Mg* \rightarrow n + 3^{4}He + {}^{12}C \tag{3.60}$$

Protons, pions and other hadrons can also collide with nucleus of an atom and interact via the nuclear force. In the LEO space environment, the probability of such event to occur is very small. However, when a collision occurs, a nuclear reaction can be initiated. In most such reactions the scattering is predominantly in the forward direction. For example, 90% of 100 Mev proton beam in silicon will scatter in cone of half angle of 10 degrees [Tang, 1996]. Therefore significant energy may be deposited along the track of the beam.

The cross section for nuclear interactions can be obtained using rigorous quantum scattering theory. A more practical method involves phenomenological approach that uses experimental data to fit the Breit-Wigner formulas. Numerical simulations tools such as GEANT4 and NUSPA ref can also be used to accurately compute the cross sections over a large range of energies.

Cross sections using NUSPA is shown in Figure 3.22 an example of the interaction between neutrons and Si atoms is presented. Thhe total cross section of neutron on

^{28}Si are plotted against the neutron energy. The cross section, as expected, are large as the energy is low [Tang, 1996].

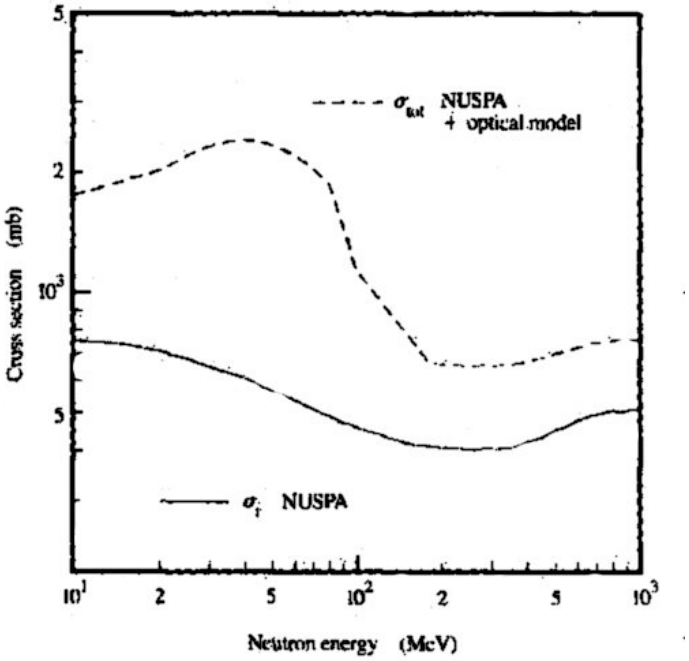

Figure 3.22: Calculated cross section using NUSPa and optical models. [Tang, 1996]

Chapter 4

Space Radiation Effects on electronics components

Damage to electronic devices on board of spacecraft due to radiation can be broadly classified as *ionizing and non-ionizing* (mainly displacement) damage. Although a brief description of displacement damage is given at the end of the chapter, the emphasis in this chapter is on ionizing radiation damage. Ionization damage can further be classified into *long-term* and *single event effects* (SEE).

4.1 Ionization Damage

Radiation damage in semiconductor materials due to the creation of electron-hole pairs is known as ionization damage. Ionization damage takes place as a consequence of the bombardment of a material by charged particles or photons with high enough energy to create an electron-hole pair. The photoelectric effect discussed in Chapter 3 is such an example. Table 4.1 gives the energy required to create an electron-hole pair for a variety of semiconductor materials and insulators used in electrical devices.

Ionizing radiation effects on semiconductor devices are classified into two major types: total ionizing dose (TID) and single-event effects (SEE). TID results in a degradation of the device due to accumulated effects of ionizing radiation over the time span of a space mission, whereas SEEs are transient or permanent effects due

Material	Chemical symbol	Type	Atomic / Molecular mass	Density (g/cm3)	First Ionization energy eV
Silicon	Si	Semiconductor	28.08	2.329	3.62
Germanium	Ge	Semiconductor	72.64	5.323	2.98
Galium arsenide	GaAs	Semiconductor	144.645	5.776	4.8
Silicon Dioxide	SiO2	Insulator	60.84	2.4	17

Table 4.1: Properties of semiconductor and insulators

to single particles. A summary of primary effects of the natural space environment on CMOS devices is given in Table 4.2.

Radiation Source	**Particle Types**	**Primary Effects in Devices**
Trapped Radiation Belts	Electron	Ionization damage
	Protons	Ionization damage, SEE in sensitive devices
Galactic Comic Rays	High-energy charged particles (ions)	Single Event Effects (SEE)
Solar Flares & CMEs	Electrons	Ionization damage
	Protons	Ionization damage, SEE in sensitive devices
	Lower energy heavy-charged particles	SEE

Table 4.2: Summary of Space Radiation Evironments and their Effects on CMOS Devices

Charge acumulation mechanisms

A transfer of energy in the range from some energy ϵ to $+dE$ from the incident particle to the target has the cross section

$$d\sigma = \frac{d\sigma}{d\epsilon} d\epsilon \tag{4.1}$$

Hence, a radiation particle traversing a distance δx inside a material with n targets per unit volume loses energy $-\delta E$ given by

$$-\delta E = n \times \delta x \int_{\epsilon_{min}}^{\epsilon_{max}} \epsilon \frac{d\sigma}{d\epsilon} \epsilon \tag{4.2}$$

where the minimum and maximum energy transfer values, ϵ_{min} and ϵ_{max} , are determined from the kinematics of the interaction. The ratio

$$-\frac{\delta E}{\delta x} = n \int_{\epsilon_{min}}^{\epsilon_{max}} \epsilon \frac{d\sigma}{d\epsilon} \epsilon \tag{4.3}$$

is usually referred to as the stopping power, presented earlier in Chapter 3, and is a measure of the energy loss per unit length of a radiation particle as it passes through the target material (generally given in $KeV/\mu m.$) It is common to normalize the energy loss per unit length by the density, ρ, of the target material and refer to it as the linear energy transfer (LET).

$$LET = -\frac{1}{\rho}\frac{\delta E}{\delta x} \tag{4.4}$$

The LET is commonly given in units of MeV cm^2/mg.Some numerical results of LET specifc for particular energy ranges, types of particles, and absorbing materials, are disscussed in more depth in Chapter 3.

For a given LET of a material, the energy and charge deposited by the radiation over a distance x (cm) are given by

$$E_{deposited} = LET \times x \times \rho \tag{4.5}$$

The charge deposited depends on the ionization energy of the atoms in the absorber.

$$Q = \frac{E_{deposited} \times e}{I} \tag{4.6}$$

Ionization damage in CMOS devices

Ionizating radiation generates electron-hole pairs in semiconductors and in insulators such as silicon dioxide. The oxide is a crystal lattice vulnerable to the build-up of injected ions [Wall and Macdonald, 1993]. Just as in semiconductors, ionizing radiation generates electron-hole pairs in insulators such as silicon dioxide layers used in semiconductor devices such as metal-oxide semiconductor (MOS) based technologies. In fact, oxide layers can be more susceptible to the build-up of charge due to electron-hole pair creation than semiconductors [Wall and Macdonald, 1993]. Although it is possible for the electron and holes to recombine, the electrons get transported away by the bias electric field quickly, whereas the holes, due to their lower mobility than electron, are often trapped at interfaces between the semiconductor and insulator potentially causing an increase in the leakage currents. Increase in leakage current can significantly reduce the time constant of the device and threshold voltage of the MOS gate. If this voltage shift is large enough, the device may change its status from 'off' to 'on' with no applied voltage. Continued exposure to radiation leads to decrease in functionality and ultimately total failure [Pisacane, 2008].

Figure 4.1, from Wall and Macdonald [1993], shows a MOS band diagram for a p-substrate capacitor with a positive applied gate.

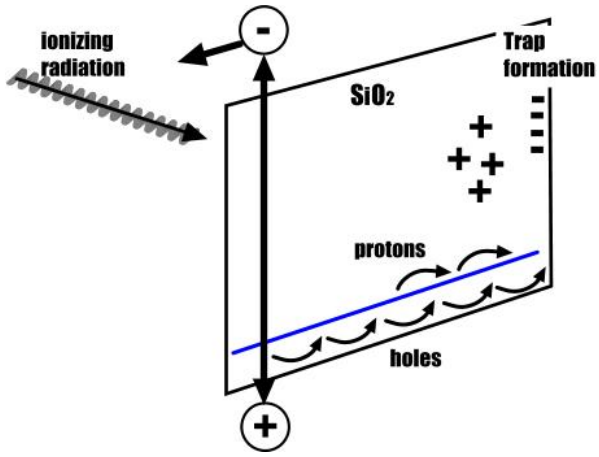

Figure 4.1: Band diagram of an MOS capacitor

Commercial off the shelf CMOS devices operating in space environment begin to

be affected by TID at about 2 Krad (for Si). The total accumulated dose depends on orbit altitude, orientation, and time. Satellites and space probes typically encounter TID between 10 and 100 krad(Si) [Wall and Macdonald, 1993].

4.2 Single Event Effects

The Single Events Effects (SEEs) can directly result from ionizing particles or by secondary particles Velazco et al. [2007]. SEEs can be put into two categories: soft errors and hard errors. Soft errors usually appear as a bit flip in a memory and do not permanently affect the functionality of the device. Hard errors are destructive to the functionality of the device, and they can either be temporary or cause permanent damage.

4.2.1 Single Event Upset (SEU)

An important SEE is Single Event Upsets. Defined by NASA as *radiation-induced errors in microelectronic circuits caused when charged particles (usually from the radiation belts or from GCR) lose energy by ionizing the medium through which they pass, producing electron-hole pairs*, resulting in damage of digital, analog, and optical components. SEUs are 'soft' errors and a reset of the device will result in normal device behavior. In digital logic and memory devices, error detection and correction codes are often utilized to reduce the effects of SEUs.

SEU Rate Calculations

When the total number of electron hole pairs generated by incident radiation reaches a critical value, which depends on the device, an SEU, for example a memory flip, ocurrs. For a sample of thickness Δx, the probability that a radiation particle will pass through the sample without any effect is given by:

$$P_T = \exp(-\rho\sigma_{total}\Delta x) \tag{4.7}$$

where

$$\begin{aligned} \rho &= \text{is the number of atoms per unit volume } (cm^{-3}) \\ \sigma_{total} &= \text{The total cross section for a specific} \\ &\quad \text{type of interaction} \end{aligned}$$

The interaction rate for given flux of incident radiation particles is given then by (Tang [1996]):

$$R = A \int_{E_{min}}^{E_{max}} dE\phi(E) \left\{1 - exp\left[-\rho\sigma_{total}(E)\Delta x\right]\right\} \tag{4.8}$$

where

$$\begin{aligned} \phi(E) &= \text{incoming energy flux } particles/cm^2 s \\ E_{min}, E_{max} &= \text{lower and upper energy limits} \\ A &= \text{surface area of the sample exposed} \end{aligned}$$

As an example, consider a reaction of 200 MeV neutrons on ^{28}Si. Since the energy is large enough there are many possible outcomes of the reaction. For example ,[Tang, 1996], in the first stage of the cascade reaction

$$n \quad + \quad {}^{28}Si \quad \rightarrow \quad 2p \quad + \quad 2n \quad + \quad {}^{25}Mg* \tag{4.9}$$

that is, two protons and two neutrons are emitted from the system, and an excited compound nucleus $^{25}Mg*$ is formed. It then de-excites by particle emission.

$${}^{25}Mg* \quad \rightarrow \quad n \quad + \quad 3^4He \quad + \quad {}^{12}C \tag{4.10}$$

The process presented in the Equation 4.10, has a neutron and three alpha particle emitted from the compound nucleus $^{25}Mg*$, which is transformed into a residual nucleus ^{12}C. The total cross section for this reaction is approximately 600 mb(see

Figure 3.22) which yields , for a 20 μm thick Si sample, a probability of interaction of about 6×10^{-5}.

In Si based devices about 3.6 eV is need to create an electron hole pair. An energy loss of $1MeV/\mu m$ is therefore associated with the generation of 2.8×10^5 electron-hole pairs. Which is equivalent to a local linear charge density of $\pm 44.5 fC/\mu m$. If this device requires a critical charge (Q_{crit}) of $50fC$ to flip its memory, it would take a minimum ionization energy of $1.12MeV$ to induce such shift.

More rigorous calculations of SEU rates take into account radiation transport in the material. SPENVIS was used for calculating the SEU rates for a few silicon devices in different orbits environments (at 300, 400, 500 and 600 km, respectively). The plot of the orbits are presented in Figure 4.2. A sumary of the results is shown in table 4.3.

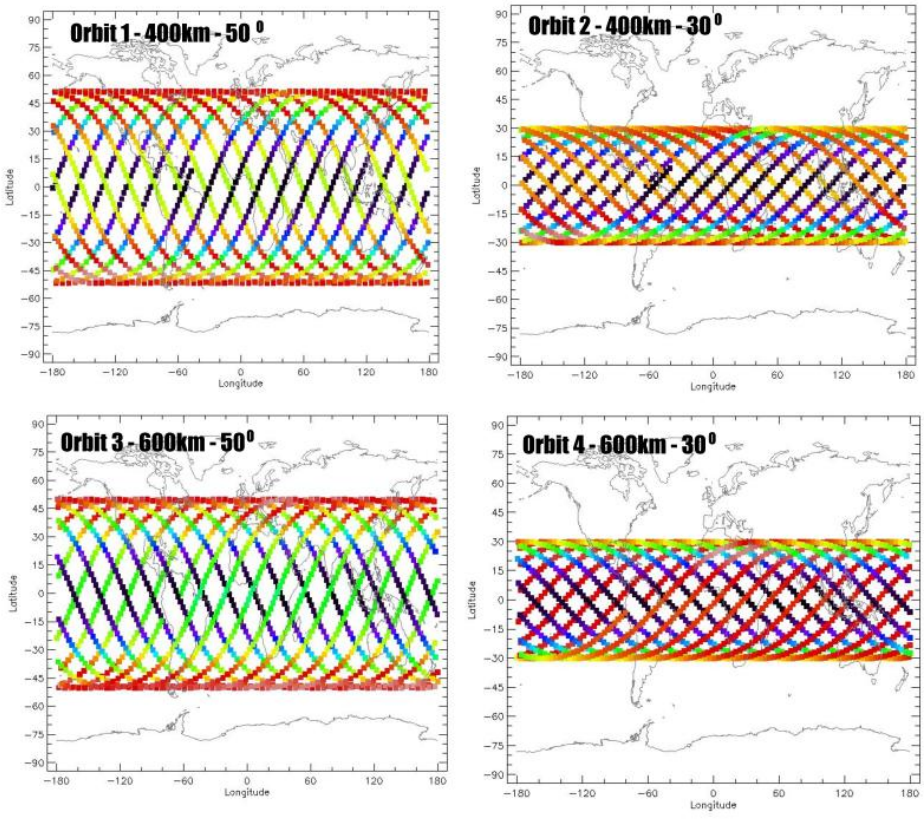

Figure 4.2: Orbits used for simulated SEU rates in SPENVIS

Orbit	**Solar Activity**	**Device**	**Total SEU rates** bit $^{-1}$ day $^{-1}$
Orbit 1	Solar Max	2164 MOS Hitachi	9.65×10^{-04}
		TC514100 Toshiba	2.81×10^{-05}
		01G9274 DRAM IBM	3.60×10^{-10}
		MB814100 (4M DRAM) Fujitsu	1.68×10^{-05}
	Solar Min	2164 MOS Hitachi	5.09×10^{-03}
		TC514100 Toshiba	1.36×10^{-04}
		01G9274 DRAM IBM	5.71×10^{-10}
		MB814100 (4M DRAM) Fujitsu	6.66×10^{-05}
Orbit 2	Solar Max	2164 MOS Hitachi	2.39×10^{-05}
		TC514100 Toshiba	6.18×10^{-07}
		01G9274 DRAM IBM	3.28×10^{-10}
		MB814100 (4M DRAM) Fujitsu	3.30×10^{-07}
	Solar Min	2164 MOS Hitachi	4.31×10^{-05}
		TC514100 Toshiba	1.11×10^{-06}
		01G9274 DRAM IBM	6.05×10^{-10}
		MB814100 (4M DRAM) Fujitsu	5.97×10^{-07}
Orbit 3	Solar Max	2164 MOS Hitachi	7.72×10^{-03}
		TC514100 Toshiba	2.12×10^{-04}
		01G9274 DRAM IBM	2.35×10^{-09}
		MB814100 (4M DRAM) Fujitsu	1.05×10^{-04}
	Solar Min	2164 MOS Hitachi	1.87×10^{-02}
		TC514100 Toshiba	5.01×10^{-04}
		01G9274 DRAM IBM	3.10×10^{-09}
		MB814100 (4M DRAM) Fujitsu	2.45×10^{-04}
Orbit 4	Solar Max	2164 MOS Hitachi	1.99×10^{-04}
		TC514100 Toshiba	4.80×10^{-06}
		01G9274 DRAM IBM	3.36×10^{-09}
		MB814100 (4M DRAM) Fujitsu	2.61×10^{-06}
	Solar min	2164 MOS Hitachi	2.33×10^{-04}
		TC514100 Toshiba	5.67×10^{-06}
		01G9274 DRAM IBM	4.31×10^{-09}
		MB814100 (4M DRAM) Fujitsu	3.12×10^{-06}

Table 4.3: SEU rates calculations using SPENVIS

4.2.2 An application to the ISS

The ISS is a good example of a typical LEO space environment where experimental data has been collected. Therefore, it is a good example to illustrate the effectiveness of the models discussed in this thesis.

Parameter	Value
Epoch (UTC):	10:00:52, 10/25/2011
Eccentricity:	0.0030834
Inclination:	51.6429°
Perigee height:	370 km
Apogee height:	412 km
Right Ascension of ascending node:	69.4065°
Argument of perigee:	89.9969°
Revolutions per day:	15.58657083
Mean anomaly at epoch:	313.9857°
Orbit number at epoch:	74608

Table 4.4: ISS Orbit Parameter

Using the above parameters and the SPENVIS coordinate generation tool a tracking of the orbit of the ISS is shown in Figure 4.3.

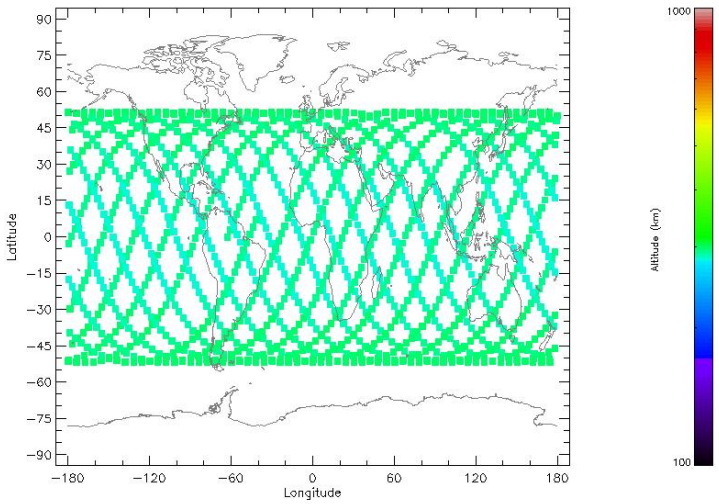

Figure 4.3: Orbit Tracking for the ISS

In order to obtain the radiation dose received by on-board devices during a solar maximum, we run the SPENVIS model (AP8 and AE8) for solar maximum. For example, the proton and electron fluxes for this ISS orbit are shown in Figure 4.4.

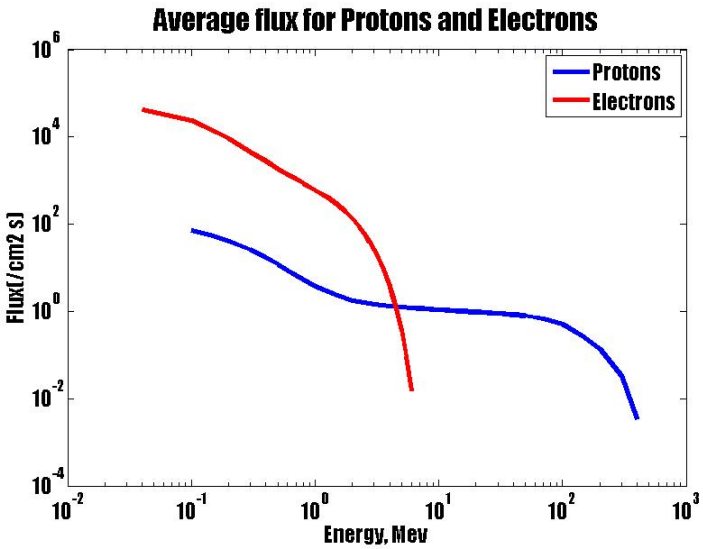

Figure 4.4: Average Generated Spectra using SPENVIs and MatLab for Protons and Electrons

Clearly, the fluxes vary with the possition of the spacecraft in its orbit,as shown in Figure 4.5. The electron flux becomes negligible for energies above 10 MeVs while the proton flux persists up to several hundreds of MeVs. Therefore, the protons are more important to consider. The exact time and intensity at a given point, where the spacecraft orbiting encounter the high energetic electrons and protons can be determined from the plots in Figure 4.6. In this case the highest exposure was between the 12:00 and 13:00 hours of this specific orbit.

Assuming a shielding of about $1.764mm$ of Al and $0.088mm$ of Ta, the proton spectrum are calculated as a function of energy and plotted in Figure 4.7. For comparison the spectrum without shielding is also shown. The results show clearly that the flux is significantly reduced by the shielding material for particle energies below 10 MeV. To confirm the results from SPENVIS, the effects of the shielding materials were also simulated using the radiation transport model, SRIM. As shown in Figure 4.8 for energies of about 10MeV the ions are stopped by the shielding. At 100Mev

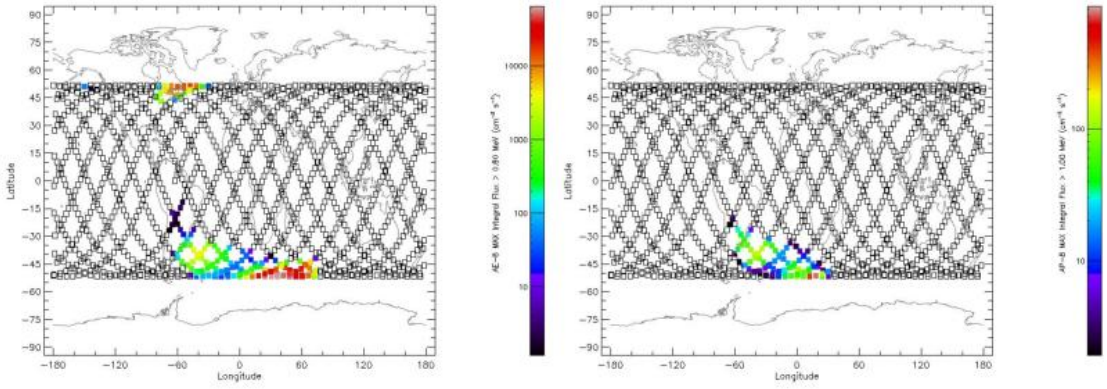

Figure 4.5: Orbital Points of exporsure for protons and electrons

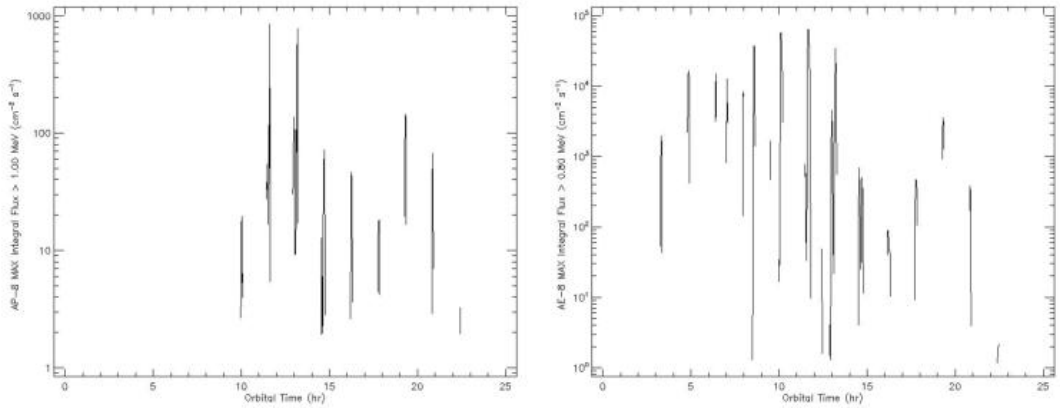

Figure 4.6: Orbital Time Plot of electron and protons

the ions continue its with very little effect from the shielding.

Using the above spectrum the effect on SEU rates can be estimated. The model used by SPENVIS uses an amount of charge collected that depends linearly on the LET of the ionizing particle and the length of its path within the sensitive volume. The input parameters for the calculation are the thickeness ($\approx$ 2mm) and the device, in this case GaAs 1K MESFET SRAM. The LET sprectrum is calculated, the rate at which energy is deposited per unit lentgh as a function of energy, and it is shown in Figure 4.9. This LET sprecctrum is used to estimate the SEU rates that result from direct ionization of the incident protons after passing a 2mm thick shield of Al.

The SEU cross section is calculated and is presented in Table 4.5

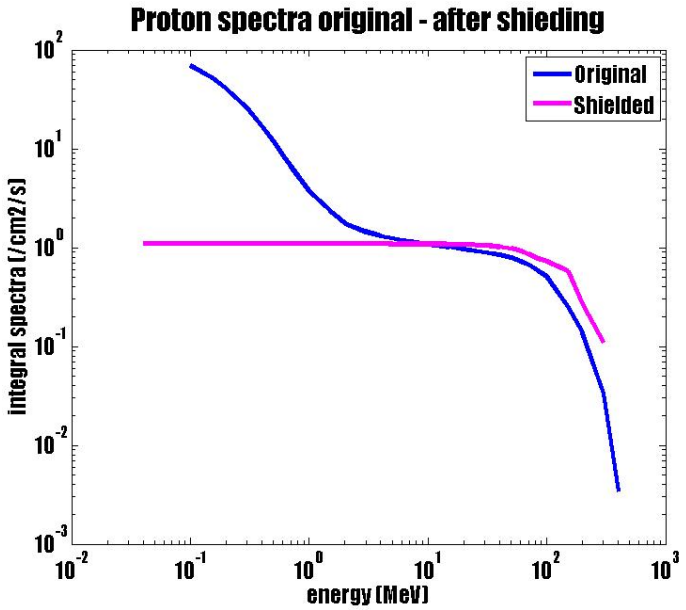

Figure 4.7: Proton spectra for LEO orbit before and after shielding. SPENVIS

Finally, the estimated SEU rates averaged over the mission is $3.1660 \times 10^6/bit\ day$.

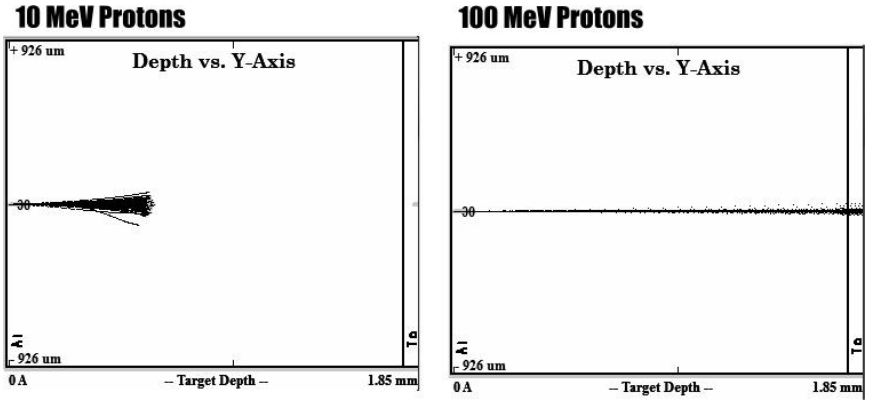

Figure 4.8: SRIM simulation of protons in a shielding of Al and Ta

Energy (MeV)	σ **(cm2 bit-1)**
17.6	4.00E-13
21.4	2.50E-13
21.6	3.50E-13
30	2.00E-12
39.8	1.00E-11
40	4.50E-12
61	9.00E-12
63	5.00E-11

Table 4.5: Cross sections for proton nuclear interaction effects, SPENVIS

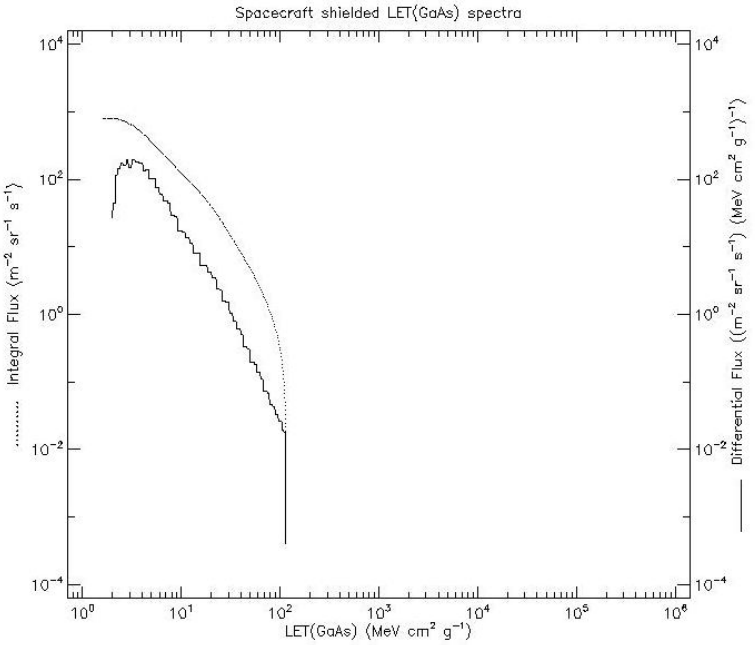

Figure 4.9: LET sprectra for the shielded spacecraft in GaAs

4.2.3 Others Single Event Effects

Single Hard Error (SHE) is an SEU which causes a permanent change to the operation of a device. An example is a stuck bit in a memory device. **Single Event Functional Interrupt (SEFI)** is a condition where the device stops normal functions, and usually requires a power reset to resume normal operations. It is a special case of SEU changing an internal control signal. **Single Event Latchup (SEL)** causes loss of device functionality due to a single event induced high current state. An SEL may or may not cause permanent device damage, but requires power resetting of the device to resume normal device operations. **Single Event Burnout (SEB)** is a condition which can cause device destruction due to a high current state in a power transistor. Ground testing has shown that power MOSFETs are susceptible to burnout when struck by a single heavy ion or proton. Most of the available data on unhardened power MOSFETs is for ions with linear energy transfer LET$>$ 25 MeV cm^2/mg. An extensive ground test programs concentrated on the effects of heavy ions and protons of power MOSFETs. The proton experiment revealed that some of the 200-volt power MOSFETs devices tested were susceptible to proton-induced SEB as well. On the CRUX experiment were flown 100-volt and 200-volt MOSFETs. **Single Event Gate Rupture (SEGR)** results when the susceptibility of dielectric layers is to hard breakdown due to single-event gate or dielectric rupture (SEGR/SEDR). It is a limiting factor for some dielectrics used in logic applications. SEGR is characterized by the sudden and permanent rupture of a gate oxide layer during irradiation, while SEDR is the generalization of this process to arbitrary dielectric layers [Beck et al., 2008].

Multiple Bit Upset (MBU) is an event induced by a single energetic particle that causes multiple upsets during its path through a device or system that occur simultaneously in either a localized area or along straight lines [Buchner et al., 2000].

4.2.4 SEE Test and Results

Validations of the models and predictions are needed to determine their accuracy. The primary Cosmic Ray Upset Experiments (CRUXs) were designed to assess the

effect of heavy ions on spacecraft system components by flight testing. This first attempt was not statistically significant due to the low scale integration, brief flight time, and lack of adequate instrumentation with which to measure the environment. However the few detections of SEUs occurred clearly in the SAA.[Adolphsen et al., 1995]

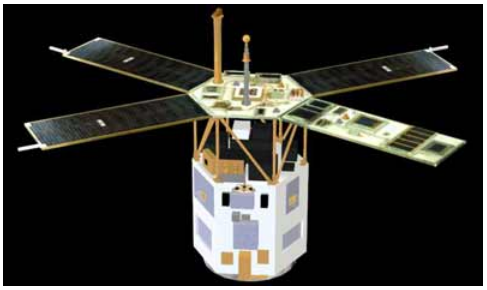

Figure 4.10: Image of the Satellite Advanced Photovoltaic and Electronic Experiment,[Adolphsen et al., 1996]

The CRUX experiment on the Air force's satellite APEX(Advanced Photovoltaic and Electronic Experiment) satellite ,shown in Figure 4.10,was launched August 3,1994 . APEX was designed to monitored SEE effect on 1Mbit and 256 Kbit SRAMs [1], listed in table 4.6 and 100 volt and 200 volt power MOSFETs [2]. The APEX satellite flown during the solar minimum between Solar Cycles 22 and 23.

Part Type	**Manufacturer**	**Technology**	**Chip Size**	**# Devices**	**Total Bits**
MT5C1008CW25	MICRON	NMOS/CMOS	$128K \times 8$	23	24117248
88130L45PC	EDI	NMOS/CMOS	$128K \times 8$	9	9437184
ZQ0405 4628128	HITACHI/ELMO	NMOS/CMOS	$128K \times 8$	16	16777216
MT5C2568CW-25	MICRON	CMOS	$32K \times 8$	40	10485760
8832C120C1	EDI	CMOS	$32K \times 8$	18	4718592
71256L100DB	IDT	NMOS/CMOS	$32K \times 8$	19	4980736

Table 4.6: SRAM test devices in CRUX

The memory devices were programmed to one of two specified states:

1. All ones or all zeroes, alternating about every 24 hours

[1] Memory Integrated Circuits
[2] Dual High current N-Channel MOSFETs

2. A checkerboard pattern

The mission duration was about 176 days of data. The comparisons between the daily fluences of protons and the upsets can be observed in Figure 4.11 the temporal profile for upsets on the MICRON 256Kbits parts for mission day 13 compared with that for protons with energies greater than 40MeV as detected by CREDO. This system not only measures the total dose acquired in flight at ten different sites within CRUX, but also monitors the environment in terms of LET of encountered particles. Most SEUs coincide exactly with the incidence of proton particles. The seven times that they do not occur with the detection of proton particles occur at L values greater than 3 and therefore, the SEUs, are most likely induced by heavy GCR ions. The total dose accumulated in the CRUX box for the first year is estimated to be less than 2 Krads.

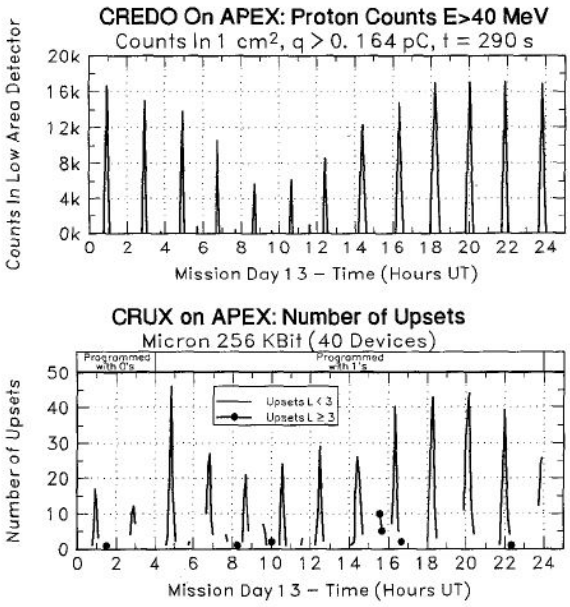

Figure 4.11: Temporal Correlation of CREDO and CRUX experimental data. [Adolphsen et al., 1995]

The occurrence of single events upsets (SEUs) during quiet magnetospheric and solar conditions was mainly due to trapped protons. The plots presented by Barth at

Barth et al. [1998], clearly showed the influence of the trapped proton belts, including the South Atlantic Anomaly on upset rates. Five minute time resolution of the data resulted in the maps shown in Figure 4.12 for altitudes of 700 and 1300 km. The effect that increasing the altitude has on the SEU rates is clear from Figures [Gussenhoven et al., 1995].

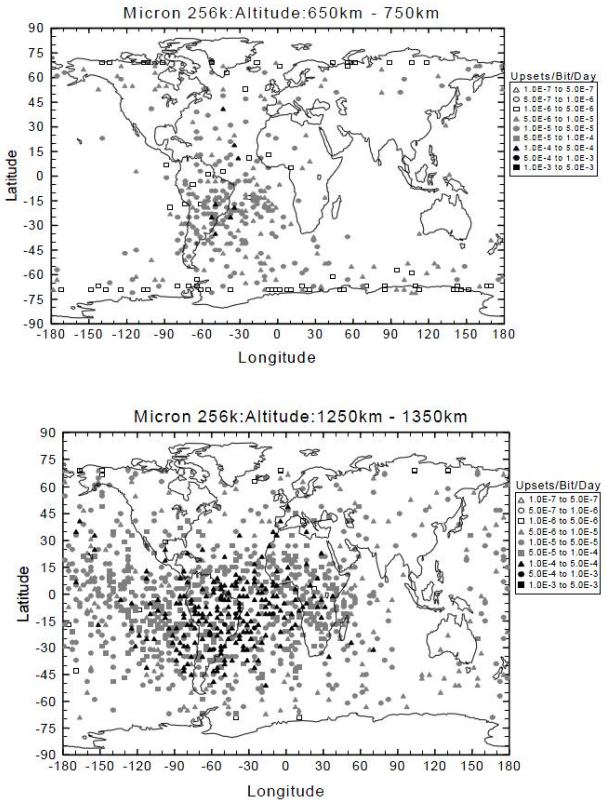

Figure 4.12: Upset Rates on the MICRON 256K at different altitudes, Barth et al. [1998]

Spacecraft and spacecraft designers are increasingly using devices instead of the more traditional radiation hardened (RH) components, in order to meet stringent spacecraft design requirements. SEE ground testing has become a key in many spaceflight programs, to determine the threshold linear energy transfers (LETs) and cross-sections for single event upset (SEU) and single event latchup (SEL). During the tests, the devices were operating as they would in a spacecraft application. First, power was supplied to the device [LaBel et al., 1995].

ION	ATOMIC #	ENERGY, MeV (MeV)	LET $MeVcm^2/mg$
C	12	102	1.44
F	19	141	3.44
Cl	35	211	11.4
Ni	58	263.2	26.4
I	127	320	59.6
Au	197	341	181.9

Table 4.7: Properties of Beam of ions for tests on SEE, NASA/GSFC Radiation Effects and Analysis

The Table 4.8 is a sumary of the experiments and results obtained by LaBel et al., the different experiments referred in the table in column #6 are described as the following:

$$
\begin{aligned}
HI &= \text{Heavy Ion Results} \\
P &= \text{Proton Results} \\
SEU &= \text{SEU LETth in } MeVcm^2/mg \\
SEL &= \text{SEL LETth in } MeVcm^2/mg \\
ssat &= \text{device cross section in cm2/device unless stated otherwise}
\end{aligned}
$$

LET_{th} is defined as the maximum LET at which no errors are seen at a fluence of 1×10^7 $particles/cm^2$. SEU LET is defined as the minimum LET value to cause an effect at a fluence of 1×10^7 particles/cm^2. SEL LET is defined as the maximum LET value at which no latchup occurs at a fluence of 1×10^7 particles/cm^2. The saturation cross section of the device is the point at which the cross section curve becomes asymptotic. Then, the effect observed in the test is in the last column of the Table 4.8. For each device the category is given in the last column: it is the number in brackets.

	Part #	Function	Manuf.	Process	LETth, ssat	Notes
FPGAs	A1280A	FPGA	Actel	CMOS	HI: SEL 59.6	[1], SEDR
EEPROMs	HN58C1001	EEPROM	Hitachi	CMOS	HI: SEL > 90	SEL only [1]
	28C256	EEPROM	SEEQ	CHMOS	HI: SEL > 90	SEL only [1]
Analog Dev.	AD524	Inst. Amp.	Analog Dev.	Bipolar	HI: SEU 11.5 [2] ssat 1E-3 SEL >80	
	AD565	DAC	Analog Dev.	CMOS	HI: SEU >80 SEL >110 ssat <1E-6	SEU defines [1] as transient $>0.5V$
	HS5212	ADC	Hybrid Sys.	Hybrid	HI: SEU 2 [2] ssat 1E-3 SEL >80 sat 1E-7	
	7820RP/372	ADC	SEI	LC2MOS	HI: SEL >80 ssat <1E-7	SEL only [1]
	DAC08AQ	DAC	PMI	Bipolar	HI: SEU 3.5 ssat 1.9E-2 SEL >80	[3]
Power Dev.	SSP21110	Pwr. Cont.	DDC	Hybrid	HI: SEU >80 SEL >80	[1] Immune to -25 SEB, SEGR
	2690R-D15F	DC-DC conv.	MDI	Hybrid	HI: SEU 4-8 SEL >72	no destr. [4] conditions
	AHE2815	DC-DC conv.	Adv. Analog	Hybrid	HI: SEU 20-26.6	poss. SEGR @ [4]

Continued on next page

– continued from previous page

	Part #	Function	Manuf.	Process	LETth, ssat	Notes
					switchoff 26.6 SEGR 59.6	59.6 w/ 28V in; @ 26.6 w/ 34V in
	MFL2805S	DC-DC conv.	Interpoint	Hybrid	HI: SEU > 72 SEL > 72	[1]
	MFL2812S	DC-DC conv.	Interpoint	Hybrid	HI: SEU 50 ssat 5E-6 SEL > 72	[2]
	MFL2815D	DC-DC conv.	Interpoint	Hybrid	HI: SEU 45-59.7 SEL >72	[2]
	MFL2815S	DC-DC conv.	Interpoint	Hybrid	HI: SEU >72 SEL >72	[1]
	LM119	Comparator	NSC	Bipolar	HI: SEL >110 ssat <1E-6	SEL only [1]
	LM139A	Comparator	NSC	Bipolar	HI: SEL >80	SEL only [1]
	LM193	Comparator	NSC	Bipolar	HI: SEL >100 ssat <1E-6	SEL only [1]
	LM108AH	Op-amp	PMI	Bipolar	HI: SEU 24 ssat 5E-4 SEL 60	[2]
	LM124	Op-amp	NSC	Bipolar	HI: SEL >90	SEL only [1]
	LM158	Op-amp	NSC	Bipolar	HI: SEL >100 ssat <1E-6	SEL only [1]
	OP07AJ	Op-amp	PMI	Bipolar	HI: SEU 11.5-13	[3]

Continued on next page

Linear Dev.

– continued from previous page

	Part #	Function	Manuf.	Process	LETth, ssat	Notes
					SEL >50	
	OP97	Op-amp	PMI	Bipolar	HI: SEL >110 ssat <1E-6	SEL only [1]
	PA10	Op-amp	Apex	Bipolar	HI: SEL >100 ssat <1E-6	SEL only [1]
	SMP11	Op-amp	PMI	Bipolar	HI: SEL 80-81.9 ssat >1E-4	SEL only [2]
	SE5521F	Sig. Cond.	SGN	Bipolar	HI: SEL >100 ssat <1E-6	SEL only [1]
	LM117H	Volt. Reg.	NSC	Bipolar	HI: SEL >110 ssat <1E-6	SEL only [1]
	LM120H	Volt. Reg.	NSC	Bipolar	HI: SEL >110 ssat <1E-6	SEL only [1]
	LM136AH	Volt. Reg.	NSC	Bipolar	HI: SEL >110 ssat <1E-6	SEL only [1]
	LP2951	Volt. Reg.	NSC	Bipolar	HI: SEL > 90	SEL only
	REF-02	Volt. Ref.	PMI	Bipolar	HI: SEL >100 ssat <1E-6	SEL only - 373J
	8116400 60PJ	16M DRAM	Fujitsu	CMOS	HI: SEU <1.41 SEL >80 P: SEU-tolerant	SEFI observed [3]
	HM5117400 RR7	16M DRAM	Hitachi	CMOS	P: fairly tolerant to	[3]

Continued on next page

– continued from previous page

	Part #	Function	Manuf.	Process	LETth, ssat	Notes
					proton-induced SEU	
	KM44C4000	16M DRAM	Samsung	CMOS	HI: SEU<1.46 ssat 1.7E-7 cm2/bit; SEL >80	SEFI and stuck[3] bits seen at 59.6
	MCM516400	16M DRAM	Motorola	CMOS	P: susceptible to proton-induced SEU	[3]
	MCM517400 J60	16M DRAM	Motorola	CMOS	P: susceptible to proton-ind. SEU	[3]
	MT4CM4B1DW6	16M DRAM	Micron	CMOS	HI: SEU <1.41 SEL 12-26.6 ssat >2E-4	[4]
	TC5117400 FT-70	16M DRAM	Toshiba	CMOS	P: susceptible to proton-ind. SEU	[3]
	TC5117400J	16M DRAM	Toshiba	CMOS	HI: SEU<1.46 ssat 1.8E-7 cm2/bit; SEL>80	
	70324	Dual port RAM	IDT	CEMOS	HI: SEL > 90	[3]
	70V25	Dual port SRAM	IDT	CMOS	HI: SEU <3.46 ssat 5E-7	[3]

Continued on next page

– continued from previous page

	Part #	Function	Manuf.	Process	LETth, ssat	Notes
FIFOs	7201T	9x512 FIFO	IDT	6, 8, 10, 12u Split-Epi	HI: SEL varied by EPI: 6u >80; 8u 50-60; 10u >26.6; 12u 26.6 6u: ssat <1E-6 P: 6u not easily upset	6u EPI was [4] SEL resistant, but very SEU sensitive
	7203ERP	9x2048 FIFO	IDT	CMOS/epi	HI: SEU 8 - 11.6 control SEU 20 SEL 35	[3]
	7203L40DB	9x2048 FIFO	IDT	Bulk	HI: SEU 3.4 ssat 5.5E-3 SEL 15-22	[4]
μprocessors	7204	9x4096 FIFO	IDT	Bulk CMOS	HI: SEU 8 - 11.6 SEL 16	[4]
	80386-20	Micro-processor	Intel	CHMOS IV	HI: SEU 3.38 SEL 37.1 - 59.9	Microlatch only
	80386DX-25	Micro-processor	Intel	CHMOS IV	HI: SEL 29-37.1	[6], Destr. SEL only
	82380-20/B	Integrated Peripheral	Intel	CHMOS III	HI: SEU <3.38 SEL 12.2 - 26.2	[6], Destr. SEL only Control/ Mode SEU
	82380-16	Integrated Peripheral	Intel	CHMOS III	HI: SEL <12	[6], SEL only [6], SEL only

Continued on next page

– continued from previous page

	Part #	Function	Manuf.	Process	LETth, ssat	Notes
	80387	Math Coprocessor	Intel	CHMOS IV	HI: SEU 3.38 SEL 37.1-59.9	[6], Destr. SEL only
	80486DX-33	Micro-processor	Intel	CHMOS IV	HI: SEU < 3.53 w/cache on SEU 3.83 - 8.27 w/cache off SEL 20	[6], Destr. SEL
	80486DX2-66	Micro-processor	Intel	CHMOS V	HI: SEU 3.83-8.27 w/cache on or off SEL 59.6	1 device saw microlatch @59.6; 2 others SEL >80
Other	49C460	EDAC controller	IDT	CMOS/epi	HI: SEU 20-25 control SEU 26.6 SEL >80	[3]
	74FCT163 374	16 bit Register	IDT	0.5u CEMOS	HI: SEU 20 SEL 25 ssat>5E-4	3.3V/5V [4] translation
	74FCT163 245	16 bit Transceiver	IDT	0.5u CEMOS	HI: SEU >25.2 SEL 25.2 ssat>5E-4	3.3V/5V [4] translation
	MIC4427	Mosfet driver	Micrel	Bipolar	HI: SEL >72	SEL only [1]

Table 4.8: SEE proton and heavy ion test results in electronic components,

4.3 Non ionizing radiation damage

Non-ionizing radiation can produce damage in material and tissue by the production of atomic displacements.Non inonizing radiation can produce relatively stable, long-term changes in device and circuits characteristics that may result in parametric degradation and functional failure. Non-ionizing energy loss result in displacement damage and defects in both insulator and semiconductor regions. A detailed description of displacement damage can be find in [Beck et al., 2008].

4.4 Effects of Shielding Materials

4.4.1 Materials

Composite materials, or simply composites, are commonly used for shielding in space. Composites may be engineered or naturally occurring materials made from two or more constituents with significantly different physical or chemical properties. Two factors make composites material good choices in space applications: high specific modulus and strength, and dimensional stability during large changes in temperatures in space [Hull and Clyne, 1996].In addition to debris composites also provide radiation shielding. Materials with low atomic number ($low - Z$)(e.g., hydrogenous materials) are more effective than $high - Z$ materials for reducing exposure to cosmic radiation.

Some common shielding materials are Polyethylene, Kevlar, Nextel and Aluminum. During space missions, polyethylene and polyethylene based composites are used as structural materials, radiation shielding materials, and electrical insulators. Polyethylene (C_nH_n) is a relatively inexpensive, stable, and, with a low atomic number to maximize the Coulombic Stopping while minimizing other secondary paticle porduction and has been certified for use aboard the ISS. Polyethylene is a good shielding material because it has high hydrogen content, and hydrogen atoms are good at absorbing and dispersing radiation [Stephens, 2008].

Another useful shielding materials is KEVLAR. ®The polymer poly-p-bezamide liquid crystalline solutions due to the simple repetitiveness of its molecular structures lead to current development of KEVLAR, Figure 4.13. [Systems, 2005]

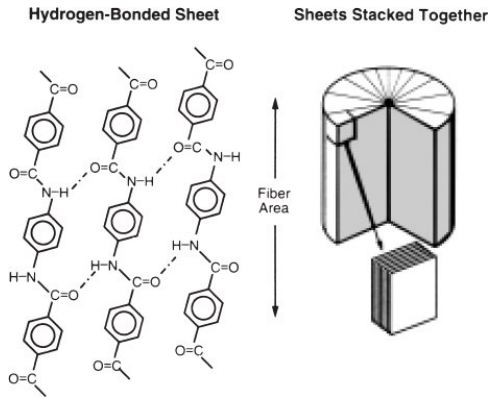

Figure 4.13: Rod-Like Fiber structure by the radial stacking of Hydrogen-Bonded sheets

NEXTEL^{TM}, which is a continuous filament ceramic oxide fibers can be readily converted into textiles which meet demanding performance requirements in high temperature operating environments. Additionally, the NEXTEL fibers have low elongation and shrinkage at operating temperatures, which allow for dimensionally stable product with good chemical resistance, low thermal conductivity, thermal shock resistance, low porosity and unique electrical properties.

Another useful shielding material is **Aluminum**. Due to its low density, Aluminum is one of the more commonly used spacecraft surfaces. Its optical properties make it a good choice for thermal control. Furthermore, it is ideal for use in Low Earth Orbit (LEO) where Atomic Oxygen attack is a major design issue.

4.4.2 Tests

In agreement with the basic models, experiments clearly show that light, highly hydrogenated materials, like polyethylene, provide the best radiation shielding. A typical shielding was tested by [Destefanis et al.], to investigate the total energy released inside Nextel, Kevlar, Aluminum and High Density Polyethylene. A 1GeV/n Fe-beam was selected as a useful simulator of the actual galactic cosmic radiation heavy spectrum.

The main conclusion presented by Destefanis et al. is that Kevlar is a good radiation shielding material, with an effectiveness close $(80-90\%)$ to that of polyethylene.

This data confirmed that hydrogen-rich materials are effective radiation shields. It also show that Kevlar, which is rich in light atoms like carbon, is rather effective. However, Nextel and aluminum resulted to be much poorer radiation shielding materials.

The effectiveness of Kevlar over Aluminum as a radiation shield is also confirmed by test that are being carried out the ISS Pugliese et al. [2010]. Equivalent dose rate for KEVLAR and Aluminum due to reactions and secondary particles from the ISS data are sumarized in Table 4.9.

experiment	**Shield**	**equivalent dose rate (uSv/d)**
Secondary	no shield	510 ± 43
	Al Shield	570 ± 43
	Kevlar Shield	493 ± 43
Neutrons	no shield	78 ± 23
	Al Shield	74 ± 21
	Kevlar Shield	65 ± 18

Table 4.9: Equivalent Dose rate for experiments on ISS

Accelerator-based tests to characterize the radiation properties of Kevlar and Nextel done by Lobascio et al. [2008] the radiation dose for GCR heavy ions is approximately $80 - 90\%$ of that produced by the same mass of polyethylene, while a double mass of Nextel is necessary to achieve that same reduction. Both Kevlar and Nextel provide a higher attenuation that the same mass of aluminum. (Figure 4.14)

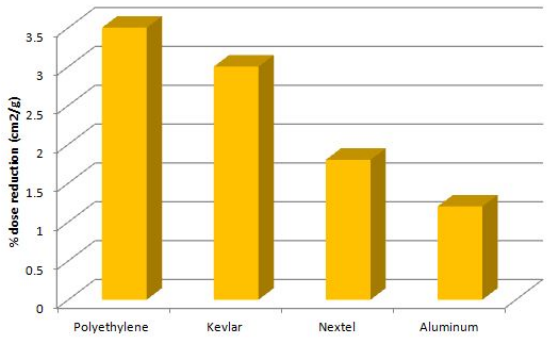

Figure 4.14: Percent of dose reduction per unit areal density.

Chapter 5

Conlcusions

- The theoretical calculations of the stoppings power and average range were accurate when compared with a more specific Monte Carlo simulation of the interaction betwen charge particles and matter.
- The shielding properties of the materials were evaluated, eihter with calculations or simulations, giving both the same results.
- For protons and heavy ions, water behaves as the best shield, for lower energies. As the energy of the particles increases Lead will come as the best shield. For some applications, it could be Kevlar and Polyethelene could be usefull.
- Germanium and GaAs have similar properties and behave in the same way for interactions with heavy charge particles. These materials also are the most suceptible because the LET on them is greater than Si.
- The SEU rate depends on the energy of the incoming particle, but mostly on the secondary particles. To calculate the rates is require the fluence of the incoming particles
- Kevlar behavior in space environment, and in particular its outgassing properties, resistance to hypervelocity impacts and particle radiation shielding have been well characterized as individual material and in combination with other materials.

- Solar Cycle, during maximum solar activity phase, exposure rates from GCR and trapped protons are lowest yet exposure to solar particle event is highest.
- Extra vehicular activities are programmed to avoid passage of the ISS orbit through the SAA
- Spacecraft location and orientation
- Exposure rate decreases with decreasing altitude in LEO. Atmospheric drag upon spacecraft is a costly impact. During solar maximum activity higher altitudes are used where drag is reduced but higher dose rates result

Shielding can significantly reduce TID, but it can rarely affect SEEs since particles energetic enough to cause SEEs typically require shields several inches thick to be adequately attenuated. Unfortunately, shielding may also enhance TID and SEEs by slowing fast particles into energy ranges of SEE or TID sensitivity. Therefore, given that flight path considerations and shielding cannot completely shelter electronics from radiation, designers must use radiation hardened (rad-hard) and fault tolerant subsystems as the final recourse. Device intended for use in LEO space environment often require radiation hardening , i.e., they need to be specially designed and fabricated to be radiation tolerant. Nevertheless, rad-hard standard parts have radiation exposure limits [Wall and Macdonald, 1993] beyond which they don't operate safely; therefore designers of spacecraft mission must take into account the radiation-tolerance issues of the electronic devices and must minimize these effects using carefully planned trajectories and shields.

Future work will start by a more accurate and extensive model of the nuclear interactions and then obtain the dependace of this result with the rate of SEUs. Furthermore ,run simulations for different orbits and determine the posible correlation SEU rate and altitude with the help of online models and simulations.

Appendix A

Cometial Space Vehicles

Spacecraft	Manufacter	Notes
Genesis I & II	Bigelow	Space ultra-low mass membrane structure. Used films: polyester, polyimides ,perfluorinated polymers, and Mylar. Utilize mainly for space stations and long period maned spacecraft [Bigelow, 2011]
SpaceShipOne	Scaled Composites	Spaceship one is a three-place, high altitude research rocket, designed for suborbital's flight to 100km altitude. The spaceplane is carried by White Knight, a manned, twin-turbojet research aircraft intended for high-altitude missions. [Composites, 2011]
SpaceShipTwo	Scaled Composites	SS2 will carry two pilots and six passengers on a suborbital space trip lasting two and a half hours. Is dropped from beneath the White Knight Two. The apogee of the new craft will be approximately 110 km. The unique way it returns is via the feathering system which does away with the need for sophisticated computer driven flight control systems or the need to rely on the pilots [Galactic, 2011] [Composites, 2011]
Kankoh Maru	Japanese Rocket Society	The Single Stage To Orbit and Vertical Takeoof and Landing was designed to carry 50 passengers to low Earth orbit.Employs a 'split crew' concept.[Anderson, 2011]
Ascender	Bristol Spaceplanes	Takes off from an ordinary airfield using its turbofan engine and climbs at subsonic speed to a height of 8 km, has a maximum speed of around Mach 3 on a steep climb and can reach a height of 100 km. On reaching the atmosphere, the pilot pulls out of the dive and flies back to the airfield .[Spaceplanes, 2011].
Black Armadillo	Armadillo Aerospace	The current design is a single stage vehicle with nontraditional operating features. The Black Armadillo's propulsion system consists of four pressure fed, hydrogen peroxide, monopropellant system rocket engines fed from a single tank.[Prize, 2003]

Continued on next page

– continued from previous page

Spacecraft	Manufacter	Notes
LYNX	XCOR.	This two-seat, piloted space transport vehicle will take humans and payloads on a half-hour suborbital flight to 100 km and then return safely to a landing at the takeoff runway. Lynx uses its own fully reusable rocket propulsion system. Is an all-composite airframe that makes it lightweight and strong. [XCOR, 2003]
CST-100	Boeing	Is a Spacecraft design proposed in 2010 that will enter in operation in 2015. It is made in collaboration between Boeing and Bigelow Aerospace , the integration of existing technologies from these companies will generate a safe, reliable transportation system
ThunderStar	Starchaser Industries	The near term objective is the creation of a 3 person reusable space capsule called Thunderstar which will be used for sub-orbital flights in excess of 100km. The second system is a vertically launched 8 seat sub-orbital space plane that could be upgradeable for orbital applications.

Table A.1: Cometial Space Vehicles

Appendix B

Spacecraft Critical Systems

System	Subsystem	Fucntion
Landing	Heat shield	A device that protects crew and equipment from heat.
	Parachute	An apparatus used to retard free fall.
	Drogue	A small parachute used to slow and stabilize a spacecraft
	Descent engine	The rocket used to power a spacecraft as it makes a controlled landing on the surface of a planet or moon
Direct-Sensing	High-energy particle detector	A device for measuring the energy spectra of trapped electrons and atomic nuclei
	Low-energy charged particle detector	A device designed to characterize the composition, energies, and angular distributions of charged particles.
	Plasma detector	A device for measuring the density, composition, temperature, velocity and three-dimensional distribution of plasmas
	Dust detector	A device for measuring the velocity, mass, charge, flight direction and number of dust particles striking the instrument
	Magnetometer	A device for measuring the strength and direction of the interplanetary and solar magnetic fields.
	Plasma wave detector	A device for measuring the electrostatic and electromagnetic components of local plasma waves in three dimensions
Remote-Sensing	Vidicon	A vacuum tube, produces a video signal of varying electrical potential measured as an electron beam is swept across a phosphor coating on the glass where the image is focused
	Charged coupled device (CCD)	An imaging large-scale integrated circuit, two-dimensional array of charge-isolated wells, each representing a pixel
	Infrared radiometer	An optical instrument that measures the intensity of infrared energy radiated by its targets.
	Polarimeter	An optical instrument that measures the direction and extent of the polarization of light

Continued on next page

– continued from previous page

System	Subsystem	Fucntion
	Photometer	An optical instrument that measures the intensity of light from a source
	Spectrometer	An optical instrument that splits the light received from an object into its component wavelengths by means of a diffraction grating.

Table B.1: Spacecraft systems

Appendix C

Introduction to Semiconductors

Materials are classified by their physical properties. Conductivity measures the amount of current trough a material when a voltage is applied, and this specific materials are classified in there conductivity groups: metals, insulators and semiconductors. Metals present practically no resistance to carrier flow, whereas insulator allows virtually no electrical carrier, but semiconductors are unique and can behave as conductors or insulators.

The difference for the conduction relies in basic principle of the quantum mechanics, where the electrons are distributed in orbit at discrete distances from the nucleus. In the figure C.1 the one atom system have the s and p level represent the orbital according to the quantum mechanics convention, for two-atom system, each energy level in the single atoms system splits into two sub-levels, as shown. When more atoms are added to construct a crystalline solid, the energy levels successively split leading to the energy bands separated by gaps of forbidden energies. This energy bands have different conduction properties.

The conduction band is where the electrons can move 'freely' through the solid without being tied to an atom. Such an electron contributes to current when a voltage is applied. Accordingly, the electrons in the valence band has an energy that us attached to an atom of the solid, and is not 'free' to move within the solid when a voltage is applied. Energy bands help us more easily understand the conductive properties of different materials. In the figure C.2 for a metal, the lowest energy value

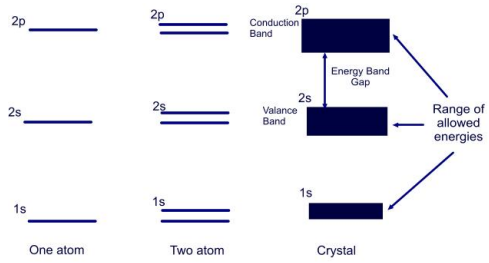

Figure C.1: Representation of energy levels

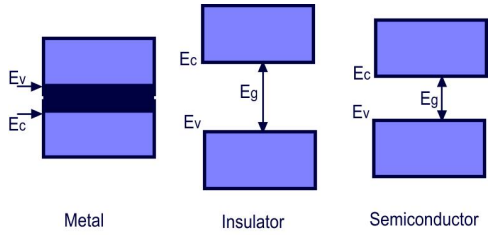

Figure C.2: Band Satructure in different materials

of the conduction band is below the maximum energy of the valence band. This means that the electrons in the conduction band are abundant and can move easily from the valence to the conduction band. The energy band structure of an insulator have a a large band gap between the valence and the conduction band so the energy need to move an electron from the valence to the conduction band is so high that only few electrons can reach this state. Semiconductors materials have a small energy band gap among the conduction and valence bands so the energy needed for electron to jump across the gap comes from the ambient temperature or photon energy. Since the energy used by the electron to jump the gap is thermal, the population of electrons in the conduction band depends on the temperature.

For some insulators the band gap is for SiO_2 $E_g = 9eV$ and for Diamond $E_g = 5.47eV$. But for some of the most popular semiconductors materials the energies of the band gap are: $GaAs$ $Eg = 1.41eV$, Si $Eg = 1.12eV$ and Ge $Eg = 0.66eV$

In metal, the electrons are the only contribution from electrons in the conducting band. On the contrary, semiconductor current has two contributions: one from electrons in the conduction band and the other from the electron vacancies in the valence band caused by electrons that jumped into the conduction band. The vacancy of

an electron in the valence band leaves an empty local charge of a value equal to the electron charge but the opposite sign. [Segura and Hawkins, 2004]

Silicon is most widely used in electronics devices instead of Germanium because when looking the structure of Si and Ge atoms, it can be seen that valence shell of Si is 3^{rd} shell while valence shell of Ge is 4^{th} shell. Hence valence electron of Ge are at large distance from the nucleus that valence electrons of silicon, thus the Ge electrons are more loosely bound to the nucleus than those of Si. Therefore valence electron of Ge can easily escape from the atom, due to very small additional energy imparted to them. So at thigh temperatures, germanium becomes unstable than silicon.

In order to change the properties of intrinsic semiconductors a small amount of some other material is added to it. This process is called doping and it helps to improve the conductivity of the semiconductors. The impurity added is called dopant. Depending upon the type of impurities added, the two type od semiconductors are : n-type and p-type.

When the impurity material used have five valence electrons (pentavalent atom) it is called donor doping as each impurity atom donated one free electron to an intrinsic material. This creates a semiconductor with large number of free electrons, called n-type semiconductor. Another type of impurity used is trivalent atom, which has only three valence electrons, this impurity is called acceptor impurity. When this is added to a intrinsic semiconductor, it creates more holes and ready to accept an electron, hence the doping generate a p-type semiconductor.[Bakshi and Godse, 2008]

The two types of materials (p-type and n-type) are chemically combined with a special fabrication technique to form a p-n junction. Consists of two semiconductor regions with opposite doping type as shown in Figure C.3. The junction is biased with a voltage Va. The junction forward-biased if a positive voltage is applied to the p-doped region and reversed-biased if a negative voltage is applied to the p-doped region. The contact to the p-type region is also called the anode, while the contact to the n-type region is called the cathode, in reference to the anions or positive carriers and cations or negative carriers in each of these regions

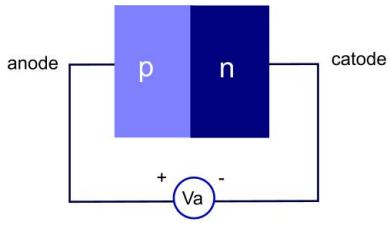

Figure C.3: Diagram of a P - N Junction

Transistor and Integrated Circuits

The Bipolar Junction Transistors have three sections of semiconductor materials with two P-N junction, may be used in amplifying or switching applications. There are two distributions PNP Transistors or NPN transistor. The simplified drawings for the Bipolar Junction transistors are shown in the Figure C.4 where B refers to the base, E to the emitter, and C for the collector

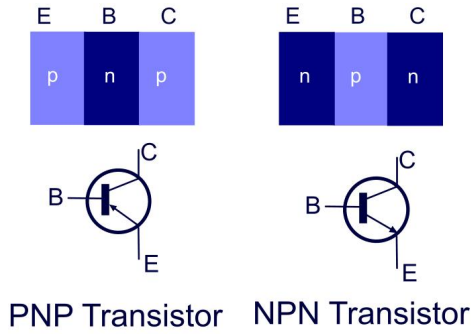

Figure C.4: Diagrams for PNP anad NPN Transistors

The normal method of applying DC to the emitter and collector of an NPN transistor is to have the emitter negative and the collector positive. The operation of the PNP is the same as for the NPN except that the roles of the electron and holes, the bias voltage polarities and the current directions are all reversed. The figure C.5 shoes the proper bias arrangement for both NPN and PNP transistors. In both cases the B-E junction is forward-biased and the B-C junction is reverse-biased.

What happens inside the transistor when is forward-reverse biased is that the forward bias in the BE narrows the depletion layer and the reverse bias in the BC widens the depletion layer. The N-type emitter region is teeming with conduction

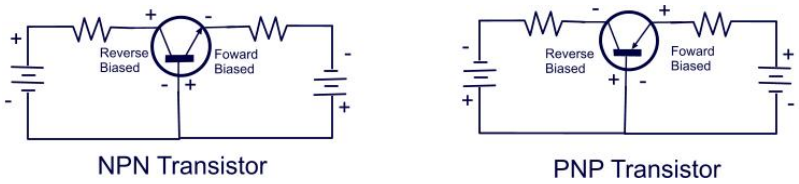

Figure C.5: Foward-Reverse Bias of a Bipolar Transistor

band (free) electrons which easily diffuse across the BE junction into the P-type base region , see the figure C.6. The base region is lightly doped and very thin so that it has a very limited number of holes. Thus only a small percentage of all the electrons flowing across the BE junction combine with the available holes. There relatively few recombined electron flow out of the base lead as valence electrons, forming the small base current (Step 2).

Most of the electrons flowing from the emitter into the base region diffuse into the BC depletion layer. Once in this layer, they are pulled across the BC junction by depletion layer field set up by the force of attraction between the positive and negative ions. In other words, the electrons are pulled across the reverse biased BC junction by the attraction of the positive ions on the other side (Step 3). The electrons now move through the collector and into the positive terminal of the external DC source, forming the collector current. The collector current depends directly in the amount of base current and is essentially independent of the DC collector voltage.

MOSFET

The acronym MOSFET stands for *metal-oxide-semiconductor field-effect transistor*. This type of component can be constructed with a channel of N-type material (*N-channel* MOSFET), or with a channel of P-type material (*P-channel* Material). A simplified cross-sectional drawing of an N-channel MOSFET and P-channel m=MOSFET along with the schematic symbol are shown in Figure C.7. MOSFET is a transistor used for amplifying or switching electronic signals. When the MOSFET was first developed, it was called an insulated-gate FET of IGFET. The gate electrode is actually insulated, by a thin layer of dielectric materials, communly SiO_2.

MOSFET technology can be operate in either of two modes: the depletion mode or

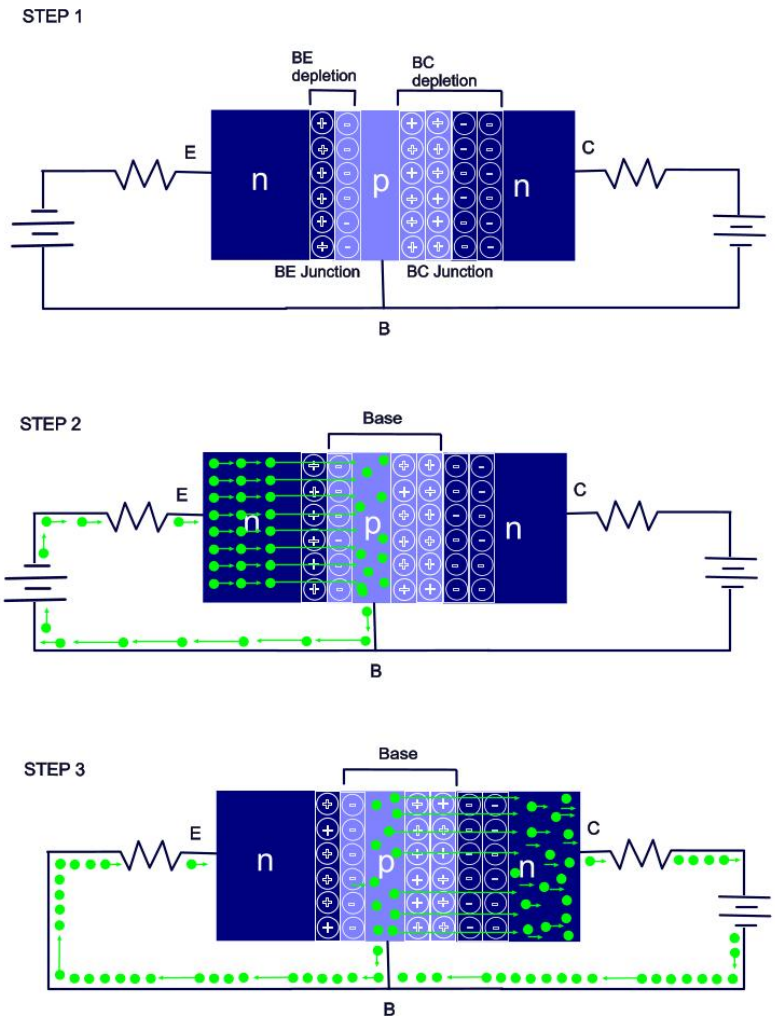

Figure C.6: Transistor Operation

the enhancement mode. Since the gate is insulated from the channel, either positive or a negative gate voltage can be applied. The MOSFET operates in the depletion mode when a negative gat-source voltage is applied and in the enhancement mode when a positive gate to source voltage is applied . [Floyd, 2006]

CMOS Technology

Complementary Metal Oxide Semiconductor is Integrated Circuit (IC) design process. CMOS is used in very large scale integrated (VLSI) or ultra large scale integrated

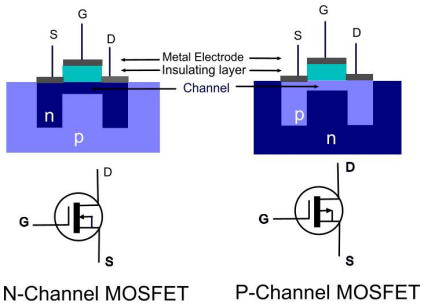

Figure C.7: Diagragram for a N-channel and P-channel MOSFET

(ULSI) circuit chips. The term VSLI is associated with chips containing thousands or millions of metal oxide semiconductor field effect transistors (MOSFETs). The term ULSI is associated with chips containing billion or more MOSFETs. [Baker, 2010]

Bibliography

J. Adolphsen, J.L. Barth, E.G. Stassinopoulos, T. Gruner, M. Wennersten, K.A. LaBel, and C.M. Seidleck. Single event upset rates on 1 mbit and 256 kbit memories: Crux experiment on apex. *Nuclear Science, IEEE Transactions on*, 42(6):1964 – 1974, dec 1995. ISSN 0018-9499. doi: 10.1109/23.489241.

J.W. Adolphsen, J.L. Barth, and G.B. Gee. First observation of proton induced power mosfet burnout in space: the crux experiment on apex. *Nuclear Science, IEEE Transactions on*, 43(6):2921 –2926, dec 1996. ISSN 0018-9499. doi: 10.1109/23.556886.

Erik Anderson. Kankoh maru flight manual, 2011. URL `http://www.spacefuture.com/archive/kankoh_maru_flight_manual.shtml`.

R.J. Baker. *CMOS: Circuit Design, Layout, and Simulation.* Number v. 1 in IEEE Press Series on Microelectronic Systems. John Wiley & Sons, 2010. ISBN 9780470881323.

U.A. Bakshi and A.P. Godse. *Electronics Engineering.* Technical Publications, 2008. ISBN 9788184315035.

J.L. Barth, J.W. Adolphsen, and G.B. Gee. Single event effects on commercial srams and power mosfets: final results of the crux flight experiment on apex. In *Radiation Effects Data Workshop, 1998. IEEE*, pages 1–10. IEEE, 1998.

M.J. Beck, B.R. Tuttle, R.D. Schrimpf, D.M. Fleetwood, and S.T. Pantelides. Atomic

displacement effects in single-event gate rupture. *Nuclear Science, IEEE Transactions on*, 55(6):3025 –3031, dec. 2008. ISSN 0018-9499. doi: 10.1109/TNS.2008.2009215.

KL Bedingfield, R.D. Leach, and MB Alexander. Spacecraft system failures and anomalies attributed to the natural space environment. *NASA reference publication*, 1390:20, 1996.

J. Bernstein, P.M. Fishbane, and S. Gasiorowicz. *Modern physics*. Prentice Hill, 2000. ISBN 9780139553110.

HA Bethe and LC Maximon. Theory of bremsstrahlung and pair production. i. differential cross section. *Physical Review*, 93(4):768, 1954.

Bigelow. Genesis i & ii, 2011. URL `http://www.bigelowaerospace.com/`.

R. A. Braeunig. Spacecraft systems. *Rocket and Space Technology, website*, 1999.

S. Buchner, A.B. Campbell, T. Meehan, K.A. Clark, D. McMorrow, C. Dyer, C. Sanderson, C. Comber, and S. Kuboyama. Investigation of single-ion multiple-bit upsets in memories on board a space experiment. *Nuclear Science, IEEE Transactions on*, 47(3):705 –711, jun 2000. ISSN 0018-9499. doi: 10.1109/23.856502.

C.L. Claeys and E. Simoen. *Radiation effects in advanced semiconductor materials and devices*. Springer series in materials science. Springer, 2002. ISBN 9783540433934. URL `http://books.google.com/books?id=Kjp2rb7LgEcC`.

Scaled Composites. Spaceship one & spaceship two, 2011. URL `http://www.scaled.com/`.

H. Davies, HA Bethe, and LC Maximon. Theory of bremsstrahlung and pair production. ii. integral cross section for pair production. *Physical Review*, 93(4):788, 1954.

J.R. Davis, R. Johnson, and J. Stepanek. *Fundamentals of aerospace medicine*. Lippincott Williams & Wilkins, 2008.

R. Destefanis, E. Amerio, M. Briccarello, M. Belluco, M. Faraud, E. Tracino, and C. Lobascio. Space environment characterisation of kevlar®: Good for bullets, debris and radiation too.

T.L. Floyd. *Electronics fundamentals: circuits, devices, and applications*. Floyd Electronics Fundamentals Series. Pearson/Prentice Hall, 2006. ISBN 9780132197090.

Vigin Galactic. Virgin galactic's vehicles., 2011. URL `http://www.virgingalactic.com/overview/spaceships/`.

M.S. Gussenhoven, G. Mullen, D.A. Hardy, D. Madden, E. Holeman, D. Delorey, and F. Hanser. Low altitude edge of the inner radiation belt: dose models from the apex satellite. *Nuclear Science, IEEE Transactions on*, 42(6):2035 –2042, dec 1995. ISSN 0018-9499. doi: 10.1109/23.489250.

D. Hastings and H. Garrett. *Spacecraft-Environment Interactions*. Cambridge Atmospheric and Space Science Series. Cambridge University Press, 2004. ISBN 9780521607568.

D. Heynderickx. Review on modelling of the radiation belts. In *Matter, antimatter and dark matter: proceedings of the second International Workshop, Trento, Italy, 29-30 October 2001*, page 87. World Scientific Pub Co Inc, 2002.

K. Holbert. Charged particle ionization and range, 2007.

D. Hull and TW Clyne. *An introduction to composite materials*. Cambridge Univ Pr, 1996.

J.D. Jackson. *Classical electrodynamics*. Wiley, 1999. ISBN 9780471309321.

C.E. Jordan. Nasa radiation belt models ap-8 and ae-8. Technical report, DTIC Document, 1989.

K. LaBel, A. Moran, D. Hawkins, A. Sanders, C. Seidleck, H. Kim, J. Fomey, EG Stassinopoulos, P. Marshall, C. Dale, et al. Single event effect proton and heavy ion test results in support of candidate nasa programs. In *Radiation Effects*

Data Workshop, 1995, NSREC'95 Workshop Record., 1995 IEEE, pages 16–32. IEEE, 1995.

Kenneth A. LaBel. Single event effect criticality analysis. *Sponsored by NASA Headquarters/ Code QW*, February 1996.

C. Lobascio, M. Briccarello, R. Destefanis, M. Faraud, G. Gialanella, G. Grossi, V. Guarnieri, L. Manti, M. Pugliese, A. Rusek, et al. Accelerator-based tests of radiation shielding properties of materials used in human space infrastructures. *Health physics*, 94(3):242, 2008.

V.L. Pisacane. *The space environment and its effects on space systems.* AIAA education series. American Institute of Aeronautics and Astronautics, 2008. ISBN 9781563479267.

B.E. Pritchard, G.M. Swift, and A.H. Johnston. Radiation effects predicted, observed, and compared for spacecraft systems. In *Radiation Effects Data Workshop, 2002 IEEE*, pages 7–13. IEEE, 2002.

Ansari X Prize. Ansari x prize, 2003. URL `http://space.xprize.org/ansari-x-prize`.

S.G. Prussin. *Nuclear physics for applications: a model approach.* Physics textbook. Wiley-VCH, 2007. ISBN 9783527407002.

M. Pugliese, V. Bengin, M. Casolino, V. Roca, A. Zanini, and M. Durante. Tests of shielding effectiveness of kevlar and nextel onboard the international space station and the foton-m3 capsule. *Radiation and environmental biophysics*, 49(3):359–363, 2010.

JE Reifert. Selling space: Accepting the risk. *AIAA Proceedings.[np]. 14-17 Sep*, 2009.

D. Sawyer and J. Vette. Ap-8 trapped proton environment for solar maximum and solar minimum, report 76-06. Technical report, National Space Science Data Center, Greenbelt, Maryland, 1976.

J. Segura and C.F. Hawkins. *CMOS electronics: how it works, how it fails.* IEEE Press, 2004. ISBN 9780471476696.

Bristol Spaceplanes. Acender spaceplanes, 2011. URL `http://www.bristolspaceplanes.com/projects/ascender.shtml`.

E.G. Stassinopoulos and J.H. King. Empirical solar proton model for orbiting spacecraft applications. *Aerospace and Electronic Systems, IEEE Transactions on*, AES-10(4):442 –450, july 1974. ISSN 0018-9251. doi: 10.1109/TAES.1974.307797.

C.P. Stephens. Proton irradiation of ultra high molecular weight polyethylene for space applications. *e-Polymers*, 042, 2008.

Advance Fiber Systems. Technical guide, KEVLAR ®aramid fiber. Technical report, DuPont, 2005.

HHK Tang. Nuclear physics of cosmic ray interaction with semiconductor materials: particle-induced soft errors from a physicist's perspective. *IBM journal of research and development*, 40(1):91–108, 1996.

R. Velazco, P. Fouillat, and R.A. da Luz Reis. *Radiation effects on embedded systems.* Springer Verlag, 2007.

J. Wall and A. Macdonald. The nasa asic guide: Assuring asics for space. *Jet Propulsion Laboratory*, 1993.

XCOR. The lynx spacecraft, 2003. URL `http://www.xcor.com/products/vehicles/lynx_suborbital.html`.